JOURNÉES NATIONALES SUR LES TECHNOLOGIES EMERGENTES EN MICRONANOFABRICATION

JNTE 2019 GRENOBLE

NOVEMBER 25-27, 2019

MAISON MINATEC
3 PARVIS LOUIS NÉEL

JNTE2019.SCIENCESCONF.ORG

LTM — LABORATOIRE DES TECHNOLOGIES DE LA MICROÉLECTRONIQUE · leti cea tech · &C cnrs — Depuis 80 ans, nos connaissances bâtissent de nouveaux mondes · RENATECH — French national nanofabrication network · UNIVERSITÉ Grenoble Alpes · LabEx MINOS-LAB · nanoSCIENCES · GRENOBLE ALPES MÉTROPOLE · SENTECH ThermoFisher SCIENTIFIC

Table of contents

FORMATION MECHANISMS OF ZNO NANOWIRES ON POLYCRYSTALLINE AU SEED LAYERS FOR PIEZOELECTRIC DEVICES

Clément Lausecker,[1,2,3] Bassem Salem,[2] Xavier Baillin,[3] Hervé Roussel,[1] Eirini Sarigiannidou,[1] Franck Bassani,[2] Estelle Appert,[1] Sébastien Labau,[2] and Vincent Consonni[1]

[1] Univ. Grenoble Alpes, CNRS, Grenoble INP, LMGP, 38000 Grenoble, France
[2] Univ. Grenoble Alpes, CNRS, LTM, F-38054 Grenoble Cedex, France
[3] Univ. Grenoble Alpes, CEA, LETI, F-38000 Grenoble, France
clement.lausecker@grenoble-inp.fr

Topic : ZnO nanowires, formation mechanisms

Abstract— **The formation mechanisms of ZnO nanowires by chemical bath deposition on Au seed layers were investigated. We show the presence of two different populations of ZnO nanowires with a given morphology and formation mechanism. These findings should be taken into account for their more efficient integration into piezoelectric devices. [1]**

FULL ABSTRACT

ZnO nanowires (NWs) are considered as attractive building blocks for piezoelectric devices, as they combine strong piezoelectric properties and the possibility to be grown at low temperature by chemical bath deposition (CBD) [2-4]. However, their integration requires the use of metallic Au seed layers, on top of which the formation mechanisms of ZnO NWs by CBD are still largely open. In this context, the nucleation and growth mechanisms of ZnO NWs on top of Au seed layers are thoroughly investigated by preparing several samples with varying Au thicknesses - ranging from 5 to 100 nm, on which ZnO NWs are grown by CBD under identical standard conditions using zinc nitrate and hexamethylenetetramine in aqueous solution [5]. We reveal the presence of two populations of ZnO NWs with a given morphology. The majority primary population is composed of vertically aligned ZnO NWs, which are heteroepitaxially formed on top of the Au (111) grains. The

resulting epitaxial strain is found to be completely relieved at the Au / ZnO interface. In contrast, the minority secondary population is made of ZnO NWs with a significant mean tilt angle around 20 ° with respect to the normal to the substrate surface, which are presumably formed on the (211) facets of the Au (111) grains. By further implementing the selective area growth using electron beam lithography, we achieve a good control over the position of ZnO NWs, although the two populations still co-exist in the ensemble. These findings provide an in-depth understanding of the formation mechanisms of ZnO NWs on metallic Au seed layers, which should be taken into account for their more efficient integration into piezoelectric devices.

REFERENCES

[1] C. Lausecker, B. Salem, X. Baillin, H. Roussel, E. Sarigiannidou, F. Bassani, E. Appert, S. Labau, and V. Consonni, "Formation mechanisms of ZnO nanowires on polycrystalline Au seed layers for piezoelectric applications," Nanotechnology, vol. 30, 2019, p. 345601.

[2] Z. L. Wang, "Towards self-powered nanosystems: from nanogenerators to nanopiezotronics," Adv. Funct. Mat., vol. 18, 2008, pp. 3553-3567.

[3] J. Briscoe, and S. Dunn; "Piezoelectric nanogenerators – a review of nanostructured piezoelectric energy havesters," Nano Energy, vol. 14, 2015, pp. 15-29.

[4] D. Lincot, "Solution growth of functional zinc oxide films and nanostructures," MRS Bulletin, vol. 35, 2010, pp. 778-789.

[5] R. Parize, J. Garnier, O. Chaix-Pluchery, C. Verrier, E. Appert, and V. Consonni, " Effects of Hexamethylenetetramine on the Nucleation and Radial Growth of ZnO Nanowires by Chemical Bath Deposition," J. Phys. Chem. C, vol. 120, 2016, pp. 5242-5250.
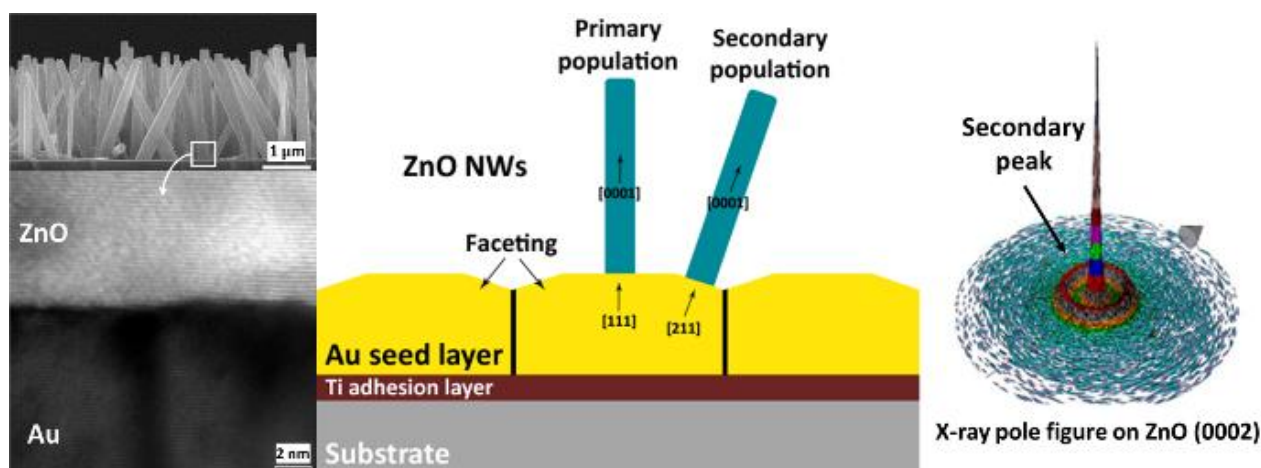
ITO OPTICAL ACCESS FOR MAGNETIC TUNNEL JUNCTION

A. Olivier[1], L. Avilés-Félix[1], A. Chavent[1], M. Rubio-Roy[1], S. Auffret[1], G. Gay[2], C. Gomez[3], T. Chevolleau[2], T. Charvolin[4], L. Vila[1], B. Dieny[1], R. Sousa[1], I. L. Prejbeanu[1]

[1]Univ. Grenoble Alpes, CEA, CNRS, Spintec, 38000 Grenoble, France
[2]Univ. Grenoble Alpes, CNRS, CEA/LETI Minatec, LTM, 38000 Grenoble, France
[3] INP Grenoble, CIME/Nanotech, 38000 Grenoble, France
[4]Univ. Grenoble Alpes, CEA, DRF/IRIG/DEPHY/PHELIQS/SINAPS, 38000 Grenoble, France

(*e-mail of contact author*): aurelien.olivier@cea.fr

Topic : *Spintronics, MRAMs*

Abstract— **In this paper, we present an integration flow of Indium Tin Oxide (ITO) as transparent conductive electrode for the realization of magnetic tunnel junctions (MTJ) with optical access. Electrical measurements validate that the developed process steps lead to properties equivalent to the reference process flow.**

I. INTRODUCTION

Magnetic random access memories (MRAM) are based on magnetic tunnel junction (MTJ) devices, corresponding to two ferromagnetic layers, a free layer and a reference layer, separated by a tunnel barrier thin enough for the quantum tunneling of the electrons to occur [1]. MRAM is known for its non-volatility, low energy dissipation, high endurance, compatibility and scalability to advanced Si complementary metal-oxide-semiconductor (CMOS) processing and technology nodes. Conventional cells are based on spin transfer torque (STT) switching. Recent advances have shown the possibility of manipulating the magnetization in magnetic systems having two magnetic sub-lattices coupled antiferromagnetically [2,3]. Based on these systems, laser pulses in the ps and fs range allow for the reversal of the magnetization even in the absence of applied magnetic field. To test these magnetic systems in a magnetic tunnel junction requires the realization of junction pillars having an optical access, using a transparent conductive electrode (TCE). It should be easy to process and robust to be used as a hard mask during a critical step of defining the tunnel junction pillar by ion beam etching (IBE). Possible transparent conductive oxides (TCO) (e.g. SnO_2, In_2O_3 and ZnO) have been heavily studied [4]. Indium Tin Oxide (ITO) (In_2O_3-SnO_2) is the most used TCO material, having the lowest electrical resistivity, is highly transparent [5], easy to process using by dry etching [6] and more robust compared to ZnO [7]. In this paper, we will introduce the process of integration of TCE based on ITO in a MTJ device in order to realize all optical switching magnetic tunnel junction (AOS-MTJ) devices and compare the electrical performances with MTJ devices based on our standard process.

II. FABRICATION

A. Standard MTJ process – Process A

The objective of this study is to compare the standard process, named Process A with the new process based on ITO named process B using the same conventional magnetic stack [8]. Both process flows are schematically described in Fig. 1. For the process A, the magnetic stack is deposited by physical vapor deposition (PVD) Fig.1 (top left). It is followed by annealing at 350°C during 15 min. A Ta layer used as a hard mask is deposited by PVD afterwards. The MTJ diameter is defined by e-beam lithography followed by Cr deposition and lift-off. The Cr layer is used as a mask to etch the Ta layer by inductively coupled plasma (ICP) to define a hard mask to etch the stack by multiple angle ion beam etching (IBE). Photolithography and Pt dry etch by reactive ion etching (RIE) are then performed to realize the bottom electrode and the top electrode accesses. In order to get electrical access to the MTJ top contact, a spacer based on Accuflo™ resist is spincoated, patterned by photolithography, dry etched and thinned down by RIE. The top electrode itself is based on Cr/Al, patterned by photolithography, e-beam evaporation and lift-off.
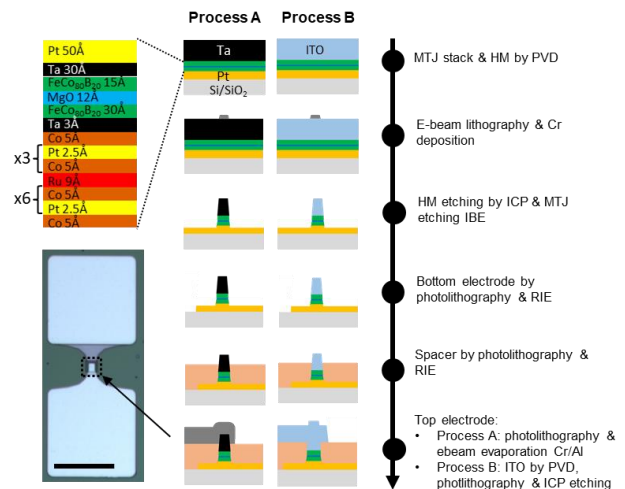
Figure 1. Process flows of Ta hard mask (HM) based MTJ with Cr/Al metallic electrode (Process A) and a proposed ITO based HM and top electrode (Process B). The magnetic stack is detailed on the top left. In bottom left, optical microscopy image of an MTJ (scale bar: 100μm)

B. ITO based MTJ process –Process B

The process B flow is similar to process A flow except for the top electrode where after the spacer realization an ITO layer is deposited by PVD and patterned as the top electrode by photolithography and ICP etching. The ITO properties and its possible used as hard mask were investigated.

To evaluate the morphology after deposition, we deposited a 150 nm ITO layer on quartz substrates by PVD at different power, O_2 flow and chamber pressure. Fig.2 shows that power influences surface morphology. Fig. 2(a-c) exhibit crystal growth at the surfaces, while higher power results in smoother surfaces, with some pyramid-like features still visible. The sample at $300W/O_2=1$ $sccm/p=8.10^{-3}mbar$ (Fig. 2(c)) shows the best compromise between crystallinity and smoothness. Changing the O_2 flow and chamber pressure degrades the surface and results in a more granular surface not suitable for process (Fig. 2(d-e)). ITO was successfully deposited on magnetic stack (Fig. 2(f)) without impact to its magnetic properties.

We measured the sheet resistance of the samples by four-point method for different deposition power conditions. The deposition at $300W/O_2=1sccm/p=8.10^{-3}mbar$ gives the lowest sheet resistance, 32 $\Omega/\square$ i.e. a resistivity of 2.3×10^{-4} $\Omega.cm$, higher than reference values [5] but suitable for our MTJ device. We have also investigated the transmittance of the ITO achieving 75% for 150 nm of ITO at 1.55 µm wavelength.
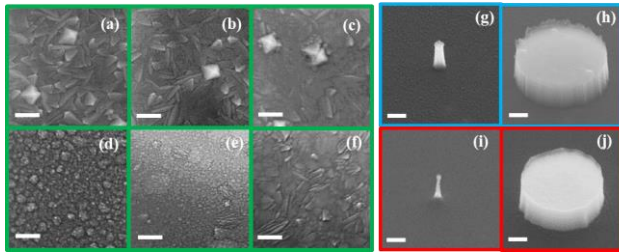
Figure 2. Top view SEM images of the deposition of 150 nm of ITO by PVD on Quartz substrates with different PVD deposition conditions (green color): (a) $100W/O_2=1$ $sccm/p=8.10^{-3}mbar$, (b) $200W/O_2=1$ $sccm/p=8.10^{-3}mbar$, (c) $300W/O_2=1$ $sccm/p=8.10^{-3}mbar$, (d) $300W/O_2=0sccm/p=8.10^{-3}mbar$, (e) $300W/O_2=1$ $sccm/p=2.10^{-3}mbar$; (f) The ITO is deposited on magnetic stack described in Fig. 1. (g-j) Tilted (45°) view SEM images of the etching by ICP of the ITO (blue) and their ITO pillars robustness through IBE process (red) for small and large diameter. Scale bar: 100nm.

In terms of process, we also investigated the patterning of ITO by using a Cr mask and ICP etching with H_2/CH_4 gases [6]. 150 nm ITO is deposited by PVD on $Si/SiO_2/Ta(5nm)/Pt(5nm)$ substrates, Pt used as a etch stop layer. We obtained ITO pillars with steep vertical sidewalls from 50 up to 500 nm diameter (Fig. 2(g-h)). ITO pillars have been shown to be robust during the IBE etch step (Fig. 2(i-j)) to pattern the magnetic stack. The ITO top electrode was patterned using the same ICP conditions and a resist mask, while using the spacer material as an etch stop.

III. ELECTRICAL RESULTS

Both processes are compared electrically to show feasibility of ITO patterned MTJ devices. Electrical results are shown in Fig. 5. We obtained a high squareness hysteresis loop as is desirable for perpendicular anisotropy magnetic tunnel junctions, as shown in Fig. 5(a). Tunnel magnetoresistance (TMR) up to 67% is achieved for MTJ having 20nm diameter as shown for both processes A and B. The observed higher TMR values for smaller diameters

is due to the higher resistance of smaller pillars. A series contact resistance at the top electrode, results in a reduction of the measured TMR signal and improved etch cleaning prior to the ITO electrode deposition should eliminate this issue. The results show that the ITO process flow is equivalent to our reference MTJ process flow.
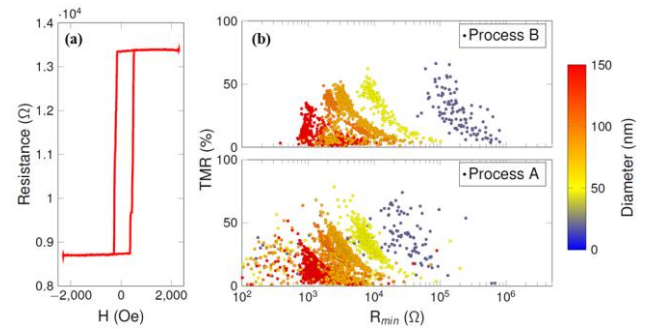
Figure 3. (a) R(H) hysteresis loop of a 80 nm diameter MTJ device. (b) TMR plot with R_{min} for different MTJ diameters comparison between standard MTJ devices process (Process A) and ITO based devices process (Process B).

CONCLUSION

Using incremental process developments, we successfully proposed, realized a fully processed magnetic tunnel junctions patterned with ITO hard mask and electrode. This developed process provides an optically accessible top electrode, without damage to the magnetic tunnel junction stack.

ACKNOWLEDGMENT

REFERENCES

[1] B. Dieny, R. B. Goldfarb, et K.-J. Lee, Introduction to Magnetic Random-Access Memory. John Wiley & Sons, 2016.

[2] M. S. El Hadri et al., « Electrical characterization of all-optical helicity-dependent switching in ferromagnetic Hall crosses », Applied Physics Letters, vol. 108, nº 9, p. 092405, feb. 2016.

[3] J.-Y. Chen, L. He, J.-P. Wang, et M. Li, « All-Optical Switching of Magnetic Tunnel Junctions with Single Subpicosecond Laser Pulses », Physical Review Applied, vol. 7, nº 2, feb. 2017.

[4] T. Minami, « Transparent conducting oxide semiconductors for transparent electrodes », Semiconductor Science and Technology, vol. 20, nº 4, p. S35-S44, apr. 2005.

[5] Z. Ghorannevis, E. Akbarnejad, et M. Ghoranneviss, « Structural and morphological properties of ITO thin films grown by magnetron sputtering », J Theor Appl Phys, vol. 9, nº 4, p. 285-290, dec. 2015.

[6] M. Mohri, H. Kakinuma, M. Sakamoto, et H. Sawai, « Plasma Etching of ITO Thin Films Using a CH4/H2 Gas Mixture », Japanese Journal of Applied Physics, vol. 29, nº Part 2, No. 10, p. L1932-L1935, oct. 1990.

[7] H. Agura, A. Suzuki, T. Matsushita, T. Aoki, et M. Okuda, « Low resistivity transparent conducting Al-doped ZnO films prepared by pulsed laser deposition », Thin Solid Films, vol. 445, nº 2, p. 263-267, dec 2003.

[8] S. Ikeda et al., « A perpendicular-anisotropy CoFeB–MgO magnetic tunnel junction », Nature Materials, vol. 9, nº 9, p. 721-724, sept. 2010

Controlling InGaAs/InAlAs interfaces in MOCVD at the level of the atomic monolayer

K. Pantzas[1,*], G. Beaudoin[1], L. Largeau[1], O. Mauguin[1], G. Patriarche[1], and I. Sagnes[1]

[1]Centre de Nanosciences et de Nanotechnologies, C2N UMR 9001 CNRS – Université Paris-Sud – Université Paris-Saclay, 91120, Palaiseau, FRANCE
*corresponding author: konstantinos.pantzas@c2n.upsaclay.fr

Topic: Synthèse, intégration et assemblage de nouveaux matériaux

Abstract — **Organo-metallic chemical vapor epitaxy is a well-established technique used for the growth of highly complex heterostructures combining a variety of semiconductor alloys with a multitude of applications in photonics. Research in MOVPE at the C2N focuses at pushing the limits of what is feasible with this technique, tackling the growth of advanced heterostructures, such as quantum cascade devices, challenging to the complexity of their structure that consists of hundreds of layers that are only a few monolayers thick.**

A particularly ripe market for such applications is the field of biological and chemical sensing in the mid-infrared. The 3 to 5 µm and 8 to 13µm bands contain the signatures of the roto-vibrational modes of a large number of molecules, allowing one to unambiguously identify and quantify trace amounts of these molecules in gas or liquid mixtures [1]. Detecting these signatures in on-chip spectroscopy systems that can be integrated on smart devices can, therefore, open these devices up to a slew of applications in biomedical and environmental sensing and ensure continued growth in the industry. Developing a platform for mid-infrared photonic integrated circuits that combine emitters, modulators, and detectors is, thus, highly desirable [2].

The key difficulty with emission and detection in the infrared spectrum is the small separation in energy of the involved transitions – typically a few hundreds to a few tens of meV. Semiconductors with the appropriate band gap are scarce and their gap can only be tuned over a narrow portion of the infrared spectrum. This limitation is lifted in devices that rely on intersubband transitions: quantum cascade lasers, quantum cascade detectors, and quantum-well infrared photodetectors. In these devices, the wavelength of optical transitions is determined by the energy separation of sub-band states in the conduction band of a coupled quantum-well structure. For a given material system, this separation in energy depends on the thickness of wells and barriers in the structure and can, through careful design, be tuned almost continuously over a wide range of the infrared spectrum.

Typical designs are comprised of several tens of stages, each stage containing around 20 wells and barriers, some of which are no thicker than a few angstrom. Therein lies the core challenge with intersubband devices: maintaining precise control over alloy composition, layer thickness, and heterointerface quality over several hundreds of ultra-thin epilayers to produce high-performance intersubband devices with predictable optical-transition wavelengths. To address this challenge, we recently used advanced scanning transmission electron microscopy techniques to precisely map the concentration of each individual layer in InAlAs/InGaAs on InP quantum cascade lasers with sub-nanometer resolution [3]. Using this information, we were not only able to precisely identify and remedy deviations from the ideal design in grown structures, but also to precisely model the effects these deviations have on the end-device by feeding the acquired information back into numerical simulations.
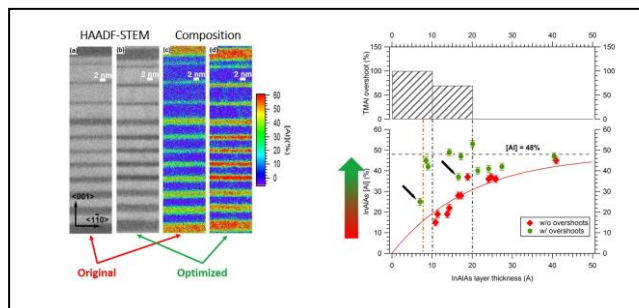
Figure: (a,b) HAADF-STEM images of two quantum-cascade laser active regions and (c,d) corresponding, sub-nanometrically resolved chemical mappings obtained using the algorithm desirved in Reference [3]. The graph on the right plots the composition versus the thickness of the InAlAs barriers for the orginal structure and the one that was optimized.

REFERENCES

[1] "More than Moore", ITRS White Pater – latest version available at www.itrs2.net

[2] ITRS Roadmap v2 – Executive summary – available at www.itrs2.net

[3] K. Pantzas et al., Semiconductor Science and Technology, 31, 055017 (2016) – http://dx.doi.org/10.1088/0268-1242/31/5/055017

A focus on the key advantages of using pARXPS versus conventional ARXPS for ultra thin films characterisation
The IMPACT project and platform: merging academic research and industrial applications in microelectronic

Bernard Pelissier[1], S. Labau[1], JH Tortai[1], J. Moeyaert[1], T Baron[1]

[1] UGA, CNRS, LTM, MINATEC Campus, Grenoble, France

Topic : Surface characterisation, XPS

Abstract

Among the few physico-chemical characterisations techniques allowing to access to a near surface chemical depht profile information, ARXPS (Angle Resolved XPS) rises the advantage of non destructive analyses.
The improvement brought by pARXPS (parallel ARXPS), with the collection of a large number of angle in only one acquisition and without any sample tilt, leads to several key advantages that will be highlighted in this contribution

The IMPACT Platform is a large multitechnique characterisation setup that we monted at lab in the scope of the EQUIPEX funding, in collaboration with LETI.

The overall idea of this innovative setup is to combine the benefits of the *quasi insitu* transfer concept (keeping the vacuum between tools) with advanced best in class characterization tool.

Thus, the purpose of such a platform is dual:

- For all processes dealing with materials sensitive to the atmosphere, the preservation of the vacuum chain between different process tools and characterization chambers allows a fine understanding and development of industrial processes [1,2,3,4,5].

- The advanced and upfront nature of the characterization techniques implemented on the platform allows extensive academic studies [6,7,8].

This second requirement, relating to upstream studies capabilities, lead us to choose "academic" tool makers for building our platform. This results in best in class characterisations modules with broad range of specifications (Fig. 1). Moreover, a specific sample loading capability allows to analyse a large variety of samples from small ones up to 300mm wafers.

Among those advanced characterisation techniques implemented on the platform, pARXPS (parallel Angle Resolved XPS) allows to access systematicaly to the angle information in only one acquisition, and without any sample tilt.
Thus, after a brief description of the IMPACT project's concept and platform structure, the presentation will highlight some key advantages brought by the systematic use of pARXPS instead of conventional ARXPS.

Two main axes will be developped :

- One about chemical depht profile reconstruction and thickness measurements, considering a metrological approach and using reference industrial samples (CIFRE ST Thesis). Comparisons / validations with MEIS analyses (INAC collaboration) will be detailed too.
  (Fig. 2, Fig. 3).

- Another one highlighting the benefit of a systematic access to the depht information for clear environment determination during fitting. Several examples will be given where pARXPS allowed a direct and unambiguous correct spectrum interpretation.

- **XPS (Thermo Fisher)**
  - ✓ pAR-XPS (parallel angle resolved XPS)
  - ✓ Angles from 20° to 80° without sample tilt
  - ✓ Spot size 20 to 400µm
  - ✓ Ion beam Ar etching for abrasion

- **Ellipsometry (Horiba Jobin Yvon)**
  - ✓ IR to V-UV : 12 µm (0,1 eV) to 145 nm (8,55 eV)
  - ✓ IR Polarimetry
  - ✓ Azimutal rotation
  - ✓ Sample heating (up to 450°C)

- **Photolum / Raman (Horiba Jobin Yvon)**
  - ✓ Based on Labram HR (best in class Raman system)
  - ✓ IR to UV (3 lasers : 355nm / 532nm / 1064 nm)
  - ✓ Confocal measurements (depth resolution)
  - ✓ Spatial resolution < 3µm

200mm / 300 mm / small sample loading capability

Fig. 1 : Advanced specifications of the IMPACT platform characterisations modules
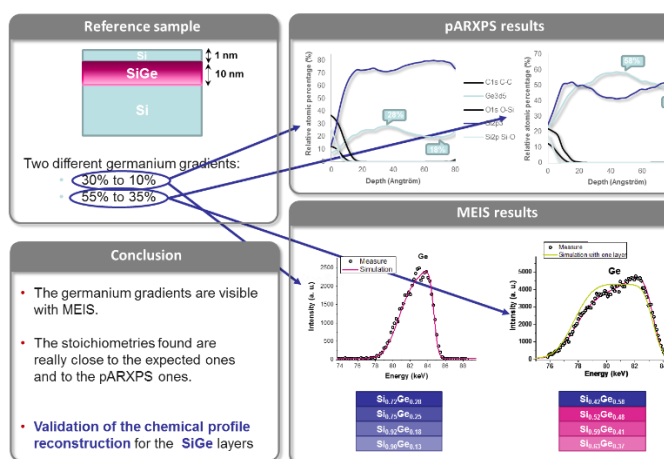
Fig. 2 : SiGe pARXPS profile reconstruction validation
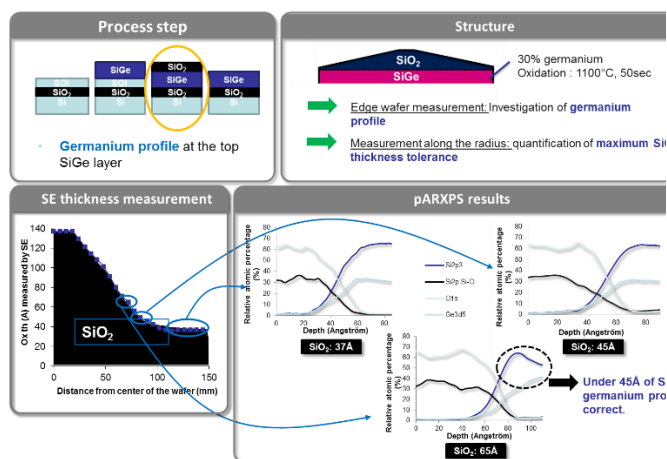
Fig. 3 : pARXPS profile reconstruction : range of use ?

Réferences

[1]. XPS analysis with an ultra clean vacuum substrate carrier for Oxydation and Airborne Molecular Contamination prevention
B.Pelissier, H. Kambara & al.
Microelectronic Engineering 85 (2008) 151-155

[2]. Impact of Oxidation on $Ge_2Sb_2Te_5$ and GeTe Phase-Change Properties
E. Gourvest, B. Pelissier & al.
Journal of the Electrochemical Society, 159 (4) H373-H377 (2012)

[3].   Interface and plasma damage analysis of PEALD TaCN deposited on HfO_2 by Angle Resolved XPS and C-V for advanced CMOS
F. Piallat, V. Beugin, & al.
Applied Surface Science, Volume 303, 1 June 2014, Pages 388-392

[4]. Area selective deposition of TiO2 by intercalation of plasma etchnig cycles in PEALD process : a bottom up approach for the simplification of the 3D integration scheme
R. Vallat, R. Gassilloud, & al.
J. Vac. Sci. technol. A 37 (2) (2019) art. no. 020918

[5]. Wet and Siconi® cleaning sequences for SiGe p-type MOS channels
P.E. Raynal, V. Loup & al.
Microelectronic Engineering, 187 (2018), p84-89

[6]. HF contamination of 200mm Al wafers: A Parallel ARXPS study
B. Pelissier, H. Fontaine & al.
Microelectronic Engineering 88 (2011), pp. 861-866

[7]. Use of optical spacers to enhance IR Mueller ellipsometry sensitivity
Gerald Ndong, Angel Lizana, Enric Garcia & al.
Applied Optics, 55 (12), pp. 3323-3332 (2016)

[8]. Depth profiling investigation by pARXPS and MEIS of advanced transistor technology gate stack
L. Fauquier, B. Pelissier & al.
Microelectronic Engineering, 169, pp. 24-28 (2017)

Core-Shell Percolative Nanodielectric for High Voltage Integrated Capacitors

M. Alfonso[1], B. Viala[2], J.-H. Tortai[1]

[1]*Univ. Grenoble Alpes, CNRS, CEA/LETI Minatec, LTM, 38000 Grenoble, France*
[2]*Univ. Grenoble Alpes, CEA, LETI, 38000 Grenoble, France*

(marco-salvatore.alfonso@cea.fr)

Topic: *core-shell nanoparticles, high-k composite, dielectric properties*

Abstract— **High-*k* dielectric nanocomposites are promising materials to miniaturize integrated capacitors. In this work, we investigate core-shell Metal Polymer Composites (MPC) having nanoparticles (carbon-coated nickel, Ni@C) dispersed in a polymer matrix (Polystyrene). A three-step formulation (desagglomeration, surface functionalization and dispersion in a polymeric matrix) was used with simple sonochemical methods. The original core-shell structure of the MPC results of the grafting of a thin second polymer layer on the carbon coating. Finally, films of MPC were deposited on silicon wafers by spincoating and Metal-Insulator-Metal (MIM) capacitors were fabricated. The dielectric response was investigated by using broadband dielectric spectroscopy.**
Preliminary results show that below the percolation threshold, MPC with a core-shell structure exhibits twice the dielectric constant of the polymer with similar losses that is encouraging for the future (higher dielectric constant, similar loss).

I. INTRODUCTION

High-*k* polymer nanocomposites, which includes metallic nanoparticles dispersed in a polymeric matrix, are key new dielectrics for ultra-small capacitors in a number of electrical and electronic applications [1-3]. Nowadays there is currently a fast growing interest in polymer based nanodielectrics because of their flexibility, low cost, easily tunable properties and versatile processing [4,5].

Dielectric polymers nanocomposites made of ceramic or metallic particles embedded into an insulating polymer matrix are among the most promising systems. This approach allows to obtain a new class of materials in which its possible to exploit the electrical features of the fillers materials in combination with the easy processing of polymers [6]. These materials exhibit a large increase of the dielectric permittivity in the proximity of the percolation threshold. The enhanced polarizability of the nanocomposite can be explained as the formation of locally large micro-capacitors effect, which contribute to increase the dielectric constant of material [7-9]. Currently, this technology suffers from a weakness due to the substantial increase of dissipation factors around percolation threshold. In practice, a lack of control on the dispersion order of the nanoparticles in the polymeric matrix generates resistive contacts between the metallic nanoparticles.

Most significant challenge in the field consists in obtaining a high permittivity value related to a low dissipation factor in the frequency ranges of interest. In this view, only a refined structural control of the nanoparticles within the polymeric matrix guarantees the achievement of the desired electrical properties.

The aim of this work is to establish a wafer-scale film fabrication process of metal polymer nanocomposites (MPC) based on commercial carbon coated nickel nanoparticles Ni@C. This work focuses the desagglomeration of the nanopowder, the surface functionalization of the nanoparticles with the aim to create a core-shell structure by grafting a thin polymer layer (few nm) on the carbon coating and the dispersion in a polymeric matrix. This three-step formulation is based on simple sonochemical methods. The core-shell structure of the MPC is intended to get greater control of interparticulate spacing distribution and to finely adjust the filling factor below the critical electrical percolation threshold where the dielectric constant be substantially enhanced with limited electrical dissipation.

II. EXPERIMENTAL PART

A. Materials

Commercial Carbon-coated nickel nanoparticles (Ni@C) are supplied by Nanostructured & Amorphous Materials, Inc. (20 nm). The polymer shell Pyr-PS$_1$ is a pyrene-terminated polystyrene (2.8 kg/mol) from Polymer Source, and the matrix PS$_2$ is a polystyrene (280k Mw) from Sigma-Adrich. The solvent used is Propylene glycol methyl ether acetate (PGMEA) from Microdeposit™ EC Solvent and used as received.

B. Preparation

The objective is to produce processable films of nanocomposite, from raw powder materials. Directly mixing the nanoparticles (NI@C) and the polystyrene matrix PS$_2$ fails, as inhomogeneous dispersion and large dewetting zones form. Hence, functionalization of the nanoparticles is required. A soft stacking of pyrene-terminated polystyrene Pyr-PS$_1$ was used to coat the nanoparticles surface.

The flow chart to obtain the casting solution of Ni@C/Pyr-PS$_1$/PS$_2$ blend is discussed. The high power ultra-sonication of the suspension of nanoparticles in PGMEA breaks the big agglomerates of the nanopowders. The dispersion is sonicated in 3 different steps of 10 minutes at 100 W (VCX500 ultrasonic processor Sonics). Afterwards the Ni@C nanoparticles are functionalized by the Pyr-PS$_1$. This step requires a further step of 10 min at the same power by adding 20 mg of polymer. Finally, PS$_2$, previously dissolved in PGMEA at a concentration of 0.3 g/ml, is added. The stabilized suspensions of Ni@C/Pyr-PS$_1$/PS$_2$ in PGMEA is used for spin-coating within the 5 minutes after the last sonication.

C. Ni@C film deposition

Nanocomposites films are spincoated on 4-inches wafers. The targeted thickness of the film is in the range of 10 μm. This was achieved by successive spincoting processes. The first coating is set at 1000 rpm with an acceleration of 5000 rpms^{-1} then the successive steps are set at 500 rpm with an acceleration of 500 rpms^{-1}. For each deposition step, 2 mL of the formulated nanocomposite resist is dropwise spread on the wafer surface After each spincoating, the films are annealed at 150 °C for 30 min on a hot plate for solvent evaporation. Films deposited onto silicon wafers with a 500 nm thick layer of thermal oxide were used for characterization purpose while films deposited on metallized wafers Si/SiO2 (500nm) /Cr (5-10nm)/Au (200nm) are dedicated for MIM capacitors measurements.
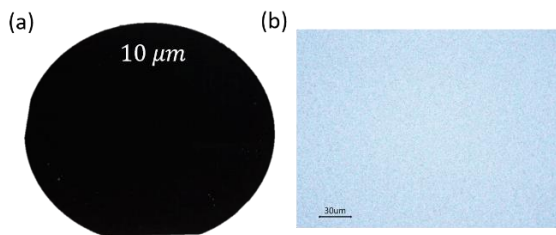

Figure 1 – (a) Pictures of Ni@C/Pyr-PS$_1$-PS$_2$ dielectric composite film, (b), Optical surface analysis (b).

For these last samples, the 30 nm top electrode is achieved by sputtering Gold through a shadow mask on the film surface. All deposited films are macroscopically uniform with a thickness in the 10 μm range. (Figure 1 (b)).

III. RESULTS AND DISCUSSION

A. Nanocomposites resist characterization

The stability of the Ni@C dispersions was investigated using the variation of the mean size distribution of the suspension measured using Dynamic Light Scattering (Zetasizer Ultra, Malvern Panalytical).
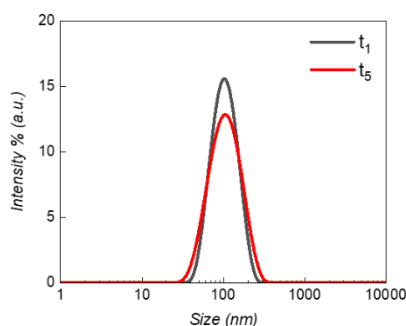

Figure- 2 DLS measurements of suspension of Ni@C nanoparticles in PGMEA at 0.0875 mg/ml after ultrasonication.

Dilution was set at 0.0875 mg/ml in order to ensure precise DLS measurements. A total of 5 successive measurements of the Scattered light was planned that covers a total sedimentation duration of 20 minutes in backscatter mode. No significant differences in the correlation curves was obtained for the first and the last scan are detected. It means that the nanoparticles dispersion is stable. In Figure 2, the measured size distribution (in intensity) of the dispersed nanoparticles is centered at 100 nm. No significant variation in the NP size is reported so negligible sedimentation occurs.

B. MIM capacitors performances

The dielectric properties of the nanocomposite at a 0.025 g/ml loading of Ni nanoparticles was determined by measuring the impedance of the MIM capacitor with an impedance analyzer (Novocontrol Alpha-A Analyzer). The AC voltage was set at 3 V and the scan recorded in a frequency range of 100 Hz–10^6 Hz. The diameter of the top electrodes is 2.5 mm and the thickness of the deposited film was measured at 13 μm by profilometry. Raw impedance measurements were conversely post processed in order to obtain the dielectric permittivity.
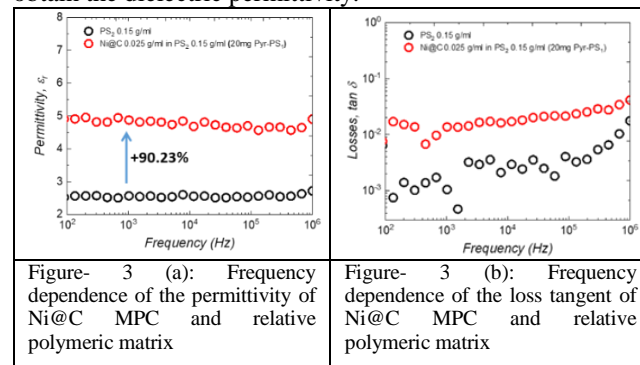

Figure- 3 (a): Frequency dependence of the permittivity of Ni@C MPC and relative polymeric matrix	Figure- 3 (b): Frequency dependence of the loss tangent of Ni@C MPC and relative polymeric matrix

Figure 3 (a) presents obtained dielectric constant for this film. One can see that the dielectric constant at 1 kHz increases from 2.5 to 4.7 when this low filler contents is added to the PS$_2$ film (90 times higher). Meanwhile the recorded values of the loss angle, in this frequency range, remain relatively low (0.02 at 1k Hz). The high-k material developed in this study exhibits low losses, making it suitable for realistic applications.

IV. CONCLUSION

We report a wafer-scale film fabrication process of core-shell MPC film for MIM capacitors based on functionalized carbon-coated nickel nanoparticles Ni@C using simple sonochemical methods and spincoating. MIM capacitors on silicon wafers were fabricated using this process.

Particles size, filling ratio and dielectric properties have been investigated. Below the electrical percolation threshold, MPC with the core-shell structure exhibits twice the dielectric constant of the polymer with similar losses that is encouraging for the future in order to rich high dielectric constant with controlled loss closer to this limit.

REFERENCES

[1] K. C. Kao *Elsevier Academic Press*, San Diego, (**2004**).

[2] A. V. Hippel, *Technology Press of MIT*, Cambridge, (**1954**).

[3] T. Osaka and M. Datta, *Gordon & Breach Amsterdam*, Netherlands, (**2001**).

[4] L. Zhang and Z.-Y. Cheng, J. *Adv. Dielectr. 1*, 389 (**2011**).

[5] Z. M. Dang, J. K. Yuan, J. W. Zha, T. Zhou, S. T. Li, and G. H. Hu, *Prog. Mater. Sci. 57*, 660 (**2012**).

[6] A. Pattanayak, S.C. Jana, *Polymer* 46, 3394–3406 (**2005**).

[7] C. W. Nan, *Prog. Mater. Sci. 37*, 1 (**1993**).

[8] M. D. Arbatti, X. B. Shan, and Z.-Y. Cheng, *Adv. Mater. 19*, 1369 (**2007**).

[9] I. Webman, J. Jortner, and M. H. Cohen, *Phys. Rev. B 15*, 5712 (**1977**)

Surface Modification and Activation with Atmospheric Plasma

Gilbert Lecarpentier, Eric Schulte.

SET North America, SETNA, Chester – NH, USA

glecarpentier@set-na.com, eschulte@set-na.com

Topic : Functionalization

Abstract— **Radicals generated within an Atmospheric Plasma Head are capable of reducing, nitridizing, or oxidizing surfaces without a vacuum chamber.**
Metastable Helium (~20eV) activates surface reactions without bombardment. Treatment leaves surfaces highly activated for subsequent processes such as functionalization, deposition or adhesives.
Environmentally friendly alternative to chemical treatments. Apparatus is described.

I. INTRODUCTION

Surfaces exposed to room air environment are typically contaminated with hydrocarbons, oxygen, nitrous compounds, OH, water, and much more. Atmospheric Plasma with reducing, oxidizing, or nitridizing gas chemistry provides controlled, pristine, highly activated surfaces for subsequent process steps in micro or nano fabrication, including complex surface functionalization. An uniquely-designed Atmospheric Plasma treatment system provides this capability *without the need for a vacuum system.* This enables continuous-feed surface preparation. We describe the Atmospheric Plasma apparatus and processes used in to prepare the surfaces for subsequent processing.

II. DESCRIPTION OF THE ATMOSPHERIC PLASMA

Figure 1 shows a schematic cross-section of the Ontos Atmospheric Plasma Head. Process gas enters at the top of the head, passes through a plasma zone created by an RF field between two electrodes, and exits the head immediately above the target substrate.
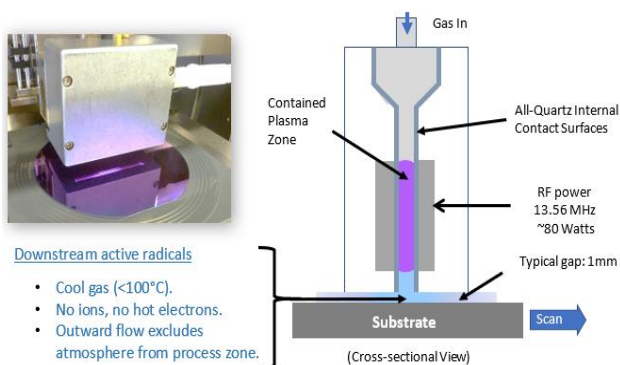

Figure 1. Atmospheric plasma head cross-section

Highly-energetic species of the plasma (ions, hot electrons) are confined within the plasma head due to their short lifetime (microseconds) at atmospheric pressure. This absence of high-energy species enables modification of delicate surfaces without bombardment such as one would encounter in a conventional vacuum plasma system. Chemical radicals created in the plasma zone, however,

have much longer lifetimes (milliseconds) and are still active when they contact the substrate below. These chemical radicals may include hydrogen atoms (H*), oxygen atoms (O*), nitrogen atoms (N*), or others. These are highly reactive species ready to chemically react with the substrate surface. Additionally, the downstream gas flow contains metastable helium atoms; which provide approximately 20eV of quantum energy directly to the substrate surface. This energy helps to activate chemical reactions, for example, two H* atoms reacting with an oxygen atom attached to the surface (i.e. a metal oxide) to remove the oxygen from the metal atom.

Similar reactions are used to remove carbon, OH, and other contaminants from the substrate surface. Additionally, N* from the upstream plasma can occupy the dangling bonds created by the loss of contaminants, and thereby protect the surface against re-accumulation of contaminants.

The flow of downstream gas from the atmospheric plasma head sweeps all room air from the reaction region at the substrate surface. This serves a similar purpose as a vacuum system without the need for vacuum chamber, pumping equipment and long pump down times. Therefore, Atmospheric Plasma is very fast and efficient, at a lower cost than vacuum plasma systems. In addition, the Atmospheric Plasma head can be positioned above moving conveyors to support continuous feed of substrates, thus eliminating "batch" processing required by vacuum plasma systems.

Figure 2. Three types of Activated Surfaces achieved with Ontos

Different types of Surface functionalization can be obtained with the standard Ontos processes, as shown in Figure 2. Such surfaces also provide an excellent interface for more complex functionalization with larger molecules.

III. SURFACE PREPARATION

A. Removal of oxidation on metallic surfaces

Copper has become a popular metallurgy for interconnect by solder joining or direct bonding [1-2].

When exposed to the atmosphere, copper oxidizes, growing a layer of oxides on the exposed surface [3] which inhibit either the bond quality of the initial joint or the long-term reliability of the bond. Atmospheric Plasma with

reducing chemistry (i.e. Hydrogen-based excited species) is capable to remove oxidation from the copper surface.

With the addition of Nitrogen Atoms (N*) in the downstream from the atmospheric plasma, the de-oxidized copper surface can be passivated to inhibit re-oxidation of the copper with exposure to air.

The surface preparation with atmospheric plasma has been successfully tested for direct bonding with the following configurations:
- Semiconductor-to-semiconductor (at RT)
- Oxide to Oxide, Nitride, semiconductor (at RT)
- Gold to Gold (as low as 100°C)
- In to In, Ag (at RT)
- SnAg – Cu (at 175°C)
- SAC to Cu, SAC (at 175°C)

B. Activation of the surface for good wetting

Atmospheric Plasma treatment activates the material surface leading to very low contact angle and excellent surface wetting for adhesion or aqueous processing.
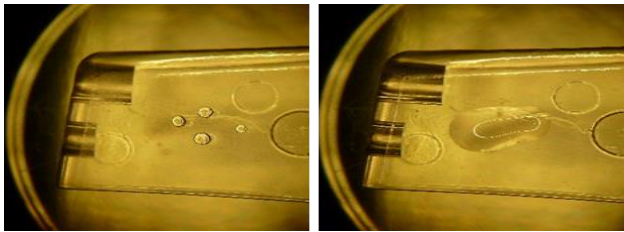

Figure 3. Medical device
(left, untreated - Right, with atmospheric plasma treatment

Biocompatible polymers (Figure 3), that are used in the manufacturing of medical devices (i.e. "Tecothane"), are naturally extremely low in surface energy, as evidenced by a very high contact angle with a water droplet. This low surface activity leads to poor adhesion of encapsulation material, and eventual assembly failure. After treatment with atmospheric plasma using oxidizing chemistry, the wettability of the module surface is significantly improved, providing long-term reliability to the module.
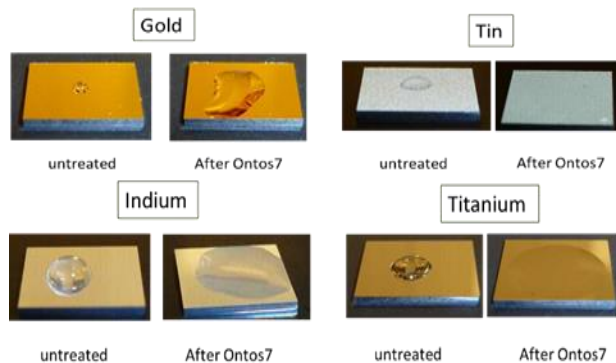

Figure 4. Surface activation on typical metals used in device fabrication.

Figure 4 shows another example of Atmospheric Plasma surface activation – this time on metal surfaces. Water contact angle on most metals is reduced from approximately 50-80 degrees down to 5-15 degrees.

These results have been achieved for Au, Sn, In, Ti, Ni, Al, and more. Insulators such as SiO_2 and Si_3N_4 also show a marked change in contact angle, typically decreasing from approximately 70 degrees to less than 10 degrees.

C. Organic contamination removal

Oxygen ashing in a vacuum system is typically used to remove organic contamination or photoresist residue. Ontos takes a different direction by using reducing chemistry (i.e. hydrogen-based excited species) to remove organics, while having the advantage that any existing oxide on the exposed metallic surface will be reduced, instead of growing more oxide as it would occur with Oxygen-based processes (figure 5).
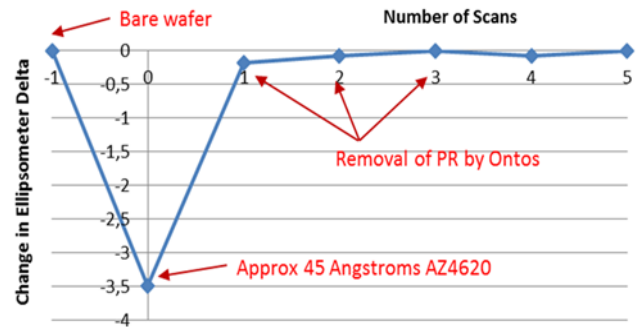

Figure 5. SiO_2-coated silicon wafer was over coated with a dilute solution of positive photoresist (AZ4620) in acetone, and then dried on a hotplate. Atmospheric Plasma with reducing chemistry removed all this heavy organic residue within three passes.

IV. ENVIRONMENTAL IMPACT

Atmospheric Plasma utilizes all-gas chemistry, typically Helium with a few percent of added Hydrogen, Nitrogen and/or Oxygen. Exhaust products are primarily Helium, water vapor, O_3, NH_3, CO, and CO_2. The quantity of these products is extremely low (typically milligrams per day), and are easily removed from the exhaust with a simple water scrubber system found in most labs and fabs. In many cases, Atmospheric Plasma can replace solvents, acids, or bases which are expensive to purchase, difficult to handle safely, and expensive and difficult to dispose of. In comparison to traditional low-pressure plasma systems, no vacuum system is required, resulting in significant savings in electricity consumption for continuous vacuum pumping.

IV. CONCLUSION

Atmospheric Plasma provides a rapid and effective surface treatment which enhances subsequent processes. Atmospheric Plasma treatment eliminates the need for solvents, acid etching, vacuum preparation chamber or adhesion promoters. The Atmospheric Plasma apparatus is relatively simple and is capable of rapid continuous throughput while employing non-hazardous chemistry.

V. REFERENCES

[1] Hummler, "TSV and Cu-Cu direct bond wafer-wafer and package reliability", ECTC 2013, pp. 41-48

[2] Lannon, "High Density Cu-Cu interconnect bonding for 3D Integration", ECTC 2009, pp. 355-369.

[3] Kyle, Investigation of RT Oxidation of Cu in Air by Yoneda - XAFS Faculty C - Department of Physics, Bergische Universität Wuppertal, Germany

sciencesconf.org:jnte2019:289929

Large scale arrays of living cells produced by automated microcontact printing

Lucas Malpartida, Emmanuelle Trevisiol, Charline Blatche, Christophe Vieu, Jean-Christophe Cau*

LAAS-CNRS, Université de Toulouse, CNRS, INSA, Toulouse, France

* INNOPSYS, Carbonne, France

contact author: lucas.malpartida@laas.fr

Topics: Surface Functionalization and Processing, Integration and Applications of Micro/Nano Technologies

Abstract— **We present a technological process for producing large arrays (1 cm^2) of human living cells (40 000 cells) immobilized on printed biomolecular micro-patterns. Statistical analysis of pattern quality and cell arrays is performed. The technique is implemented on microscope glass slides and also on thin films of soft hydrogels with adjustable mechanical stiffness (0,5 kPa-40 kPa). This methodology shows how clean room microfabrication processes can be transferred into the environment of biologists for practical use by themselves.**

I. INTRODUCTION

Creating specific devices to understand cell behavior has always been a challenge for bioengineers to provide new tools to biologists. In order to investigate key cellular mechanisms such as polarity, migration, differentiation or mechanosensing, it is required to control the adhesive pattern of the cell in a deterministic way, because the latter influences the organization of the cytoskeleton. Creating well-defined micrometric patterns that can control the position and spanning of the cell on a substrate thus appear as a technological solution of interest both for cell biology research but also for potential applications in drug or cell screening. We have developed a microfabrication process based on microcontact printing (µCP) [1], which is an elegant approach to transfer microfabrication clean room processes into the real world of biology. We have fabricated cell microarrays (CMAs) [2] over large areas. We demonstrate in this contribution that around 40 000 cells can be organized on a 1 cm² array with exceptional versatility and precision.

After the characterization and quality assessment of the patterning method, we describe how to fabricate these cell arrays on glass slides and we characterize the performances of our method for different human cell lines (PC3, HEK, HeLa). We also explain how we have transferred the process of fabrication from glass slide to polyacrylamide (PAA) hydrogels. The goal is to provide softer substrates of various mechanical properties allowing the investigation of mechanosensing properties over a large population of individual cells deterministically immobilized on registered patterns. We will describe the full processes during the conference and we will exemplify how this new technological capability opens new interesting routes in the investigation of fundamental mechanisms of cell biology.

II. AUTOMATED µCP PATTERNING METHOD

Microcontact printing (µCP) is a soft lithography technique used for generating micrometric and nanometric molecular patterns. When implemented for the final production of living cell arrays, these molecular patterns are composed of extracellular matrix (ECM) proteins and can be printed on glass slides, but also on thin hydrogel layers. In order to generate large scale arrays required for investigating large cell populations, we have used in our study an automated instead of manual µCP process (see Fig. 1.). For this purpose we actuate magnetic PDMS stamps and the Innostamp40 automate from Innopsys company [3].

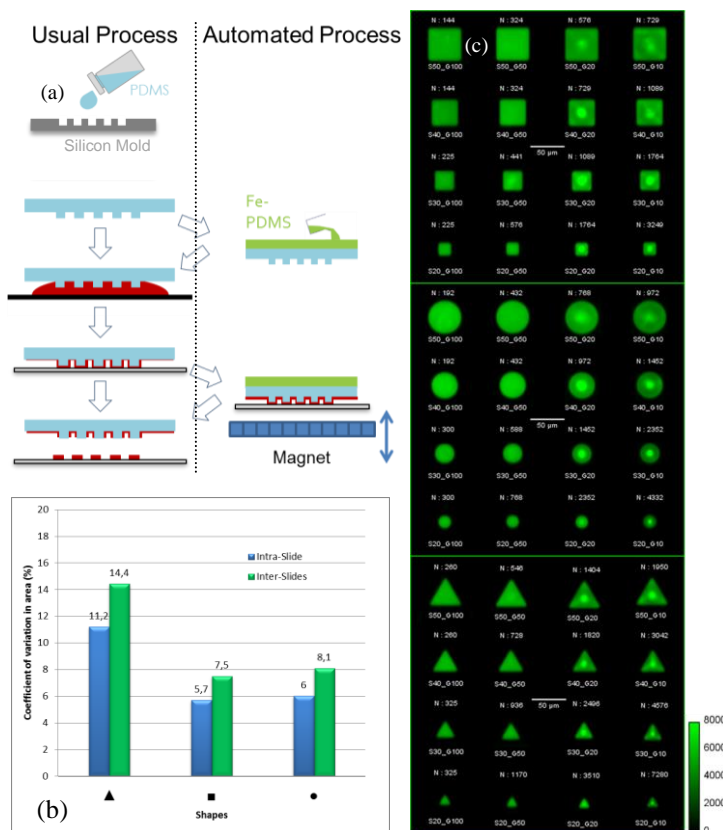Figure 1. (a) Scheme of principle of µCP and adaptation of the stamp for magnetic automatized µCP. (b)Variation coefficients of the area of the produced molecular features within one slide (intra-slide) and between 40 patterned slides (inter-slides) as a function of the shape of the printed features. (c) Average images of various types of patterns acquired over 40 printed glass slides and thousands of individual patterns.

To study the reproducibility of our patterning method, the PDMS stamps are inked with labelled Cy3-streptavidin, and automated µCP is performed on plasma-activated glass slides. We analyzed over 40 printed glass slides with thousands of features and reveal the variation coefficient of the printed area depending on the printed shapes, size and pitch within one slide (intra-slide, Fig. 1) and between all slides (inter-slide Fig. 1). We then compiled the average images of all the features (Fig. 1). This characterization at the cm^2 scale demonstrates that we can precisely define biomolecular patterns with less than 10% variations on large scale. These micro-patterns exhibit the appropriate dimensions for immobilizing individual cells with a highly controlled quality of the dimension and shape of the adhesive pattern. This kind of achievement is out of reach through manual µCP.

III. FABRICATION OF LIVING CELLS ARRAYS ON GLASS

For the production of CMA, we print fibronectin, a protein of the Extra Cellular Matrix, involved in cell adhesion. Directly after the print we incubate PLL-g-PEG which acts as an antifouling layer for the cells. The fibronectin-patterned glass slides are seeded with different cell lines (50 000 cells/cm²). Figure 2 shows a typical example with HeLa cells. The rate of occupancy of the micropatterns by some cells varies from sample to sample between 38% and 76%. Among the occupied sites, 90% are equipped with a single cell (as shown in the zoom of figure 2). Only 7% of the cells are found on the substrate outside the adhesive patterns. Compared to other techniques of CMA fabrication, these results are unique. This method of fabrication can be implemented easily by biologists outside any clean room facility, once the silicon moulds required to produce the PDMS stamp replica, have been produced.
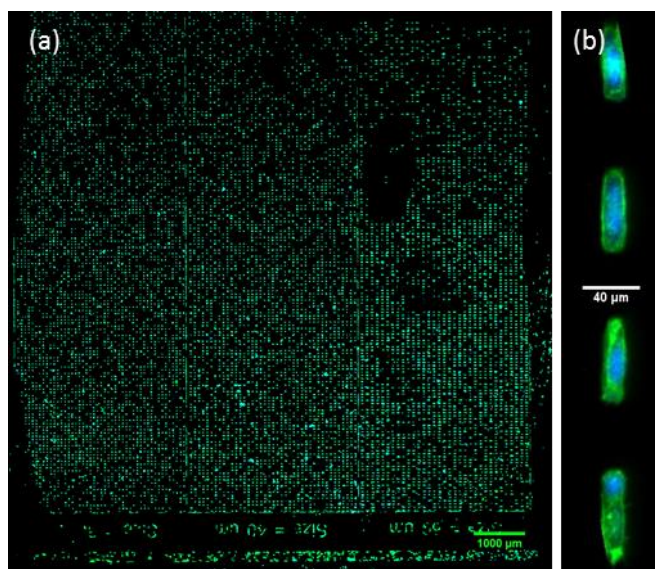
IV. FABRICATION OF LIVING CELL ARRAYS ON SOFT POLYACRYLAMIDE HYDROGELS.

We have adapted our process from reference [4] to produce the micropatterns of fibronectin at the surface of thin layers of polyacrylamide (PAA) hydrogels. We take the advantage of the stability of PAA with different compositions to obtain living cell arrays on PAA films of adjustable Young's Modulus from 0,5 to 40 kPa [5]. Figure 3 shows a typical example with HEK cells on a thin layer of PAA exhibiting a typical Young modulus of 10 kPa. The quality of the cell array is not affected by the print on a soft material and is even slightly improved compared to glass slides.
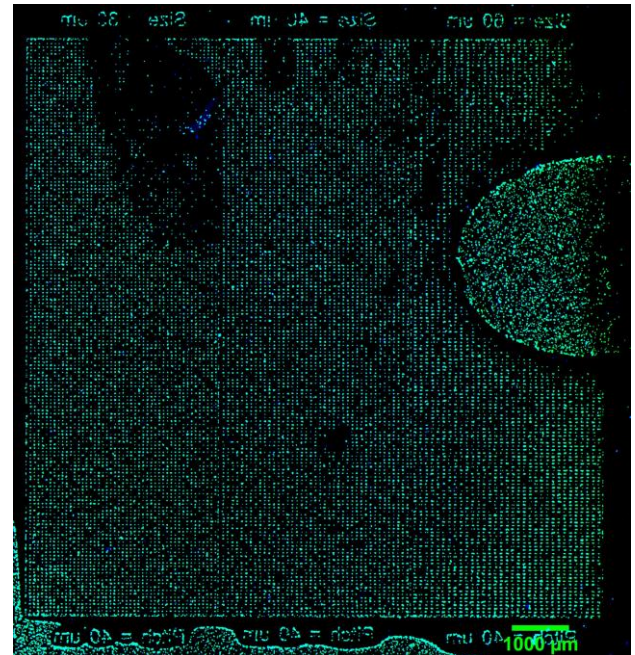

Figure 3. Typical array of HEK cells (Human Kidney) on a 10 kPa PAA hydrogel thin film (Actin labeled in green, nucleus in blue).

Figure 2. (a) Typical array of HeLa cells. (b) zoom on rectangle shapes. (Actin labeled in green, nucleus in blue).

REFERENCES

[1] S. Alom Ruiz and C. Chen, "Microcontact printing: A tool to pattern", Soft Matter, vol. 3, no. 2, pp. 168-177, 2007.

[2] R. Jonczyk, T. Kurth, A. Lavrentieva, J. Walter, T. Scheper and F. Stahl, "Living Cell Microarrays: An Overview of Concepts", Microarrays, vol. 5, no. 2, p. 11, 2016.

[3] J. Cau, L. Ludovic, N. Marie, L. Adriana and P. Vincent, "Magnetic field assisted microcontact printing: A new concept of fully automated and calibrated process", Microelectronic Engineering, vol. 110, pp. 207-214, 2013.

[4] B. Sarker, C. Walter and A. Pathak, "Direct Micropatterning of Extracellular Matrix Proteins on Functionalized Polyacrylamide Hydrogels Shows Geometric Regulation of Cell–Cell Junctions",

[5] J. Tse and A. Engler, "Preparation of Hydrogel Substrates with Tunable Mechanical Properties", Current Protocols in Cell Biology, vol. 47, no. 1, pp. 10.16.1-10.16.16, 2010.

In situ optical monitoring of the thickness of thin transparent layers with sub-nanometer resolution

A. Moreau, T. Begou, C. Koc, O. Hector, F. Lemarchand, F. Lemarquis, and J. Lumeau

Aix Marseille Univ, CNRS, Centrale Marseille, Institut Fresnel, Marseille, France

Topic: Surface functionalization and processing

Abstract—**The precise control of the thickness if thin layers is a key parameter for achieving high performance optical components. In this paper, we present how to implement direct in-situ optical monitoring for the control of the thickness of multilayer structures. Sub-nanometer resolution is demonstrated.**

I. INTRODUCTION

Optical interference filters offer a very broad range of optical functions for the control of the spectral properties of light. With the last 15-year improvement of both the design techniques and the manufacturing systems, it is now very common to fabricate very complex filters with very large number of layers and totally aperiodic structures [1]. In order to secure low errors on the thickness of each of the layers of the stack, it is not enough to implement stable deposition systems as provided by sputtering technique and a precise monitoring technique is required in order to stop the deposition when the desired layer thickness has been reached. In this paper, we review the best technique up-to-date, namely in-situ optical monitoring [2,3]. We first review the measurement techniques and then make a description of different algorithms based on optical criteria such as turning point monitoring (determination of the moment the derivative of the optical monitoring signals cancels) or trigger point monitoring (determination of pre-defined optical monitoring signal levels) to accurately stop the deposition of each of the layers [4]. We finally show how the choice of the optimal optical monitoring wavelength is a critical step that will directly affect the final performances of the filter. [4-7].

II. MEASUREMENT TECHNIQUES

There are various measurement techniques that can be implemented for optical monitoring of layers. The most common is monochromatic optical monitoring. It consists in measuring, at a single wavelength, the evolution of the transmission, or reflection, during the deposition. It generally relies on a simple measurement geometry based on a white light source (tungsten lamp), which is send directly or through a fiber, inside the vacuum chamber. The light propagates through the sample under deposition and is then collected by a fiber, spectrally filtered with a monochromator and the intensity at a single wavelength is then measured using a photodiode. An alternative solution is broadband optical monitoring. In this case the monochromator is replaced with a spectrometer and the broadband transmitted spectrum is then measured. A typical

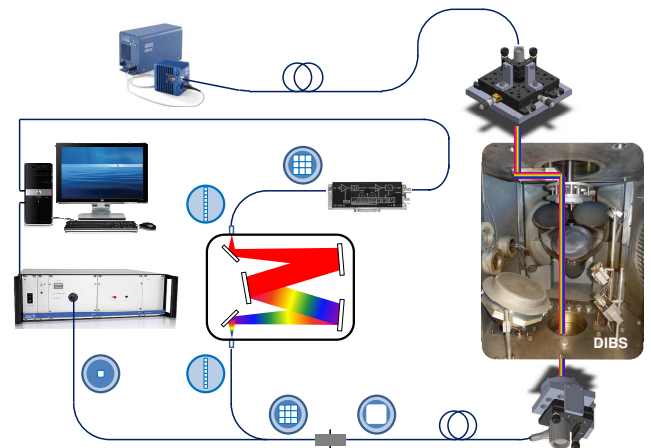geometry for both of the mentioned systems is illustrated in Figure 1.

Figure 1. Example of monochromatic and broadband optical monitoring systems installed on a sputtering deposition machine.

Other approaches based on the measurement of the reflected phase have also been recently proposed [8]. However, as of today, these solutions are only at the development level and do not represent a robust technique.

III. MONITORING ALGORITHMS

Due to the interference effects that occur within transparent layers, the transmitted intensity will be oscillate following a sine-type modulation function. The evolution can be easily modeled using a matrix-based analysis [5]. Thus, it is possible to use some of these features to define specific criteria to stop deposition when the expected optical thickness has been reached.

A. Turning point monitoring

During the growth of a thin layer, its optical thickness will gradually increase and periodically pass through a multiple of quarter-waves corresponding to a transmittance and a reflectance extremum. When this multiple number of quarter-wave is odd, the transmittance is minimum while when it is an even number (half-wave layer), the transmittance goes through a maximum. A classical method (turning point monitoring, TPM) for determining the moment to stop the deposition of a layer relies on these specific features of the transmittance signal. By properly adapting the monitoring wavelength, it is then possible to stop the deposition of a layer every time it reaches an extremum. To activate this detection, the simplest and most efficient way is to follow the evolution of its first derivative with respect to the optical thickness (or deposition time). As an example, we plotted in Figure 2 the evolution of the transmittance of a single layer with refractive index of 2.35 on a glass substrate with refractive index of 1.52 during

deposition and the associated derivative. One can see that every time a layer has a quarter-wave thickness, the derivative goes through a zero with a maximum slope and a close-to-linear dependence. This technique has been extensively used for a long time and is still actively used as it provides a simple method that can be implemented even on systems with pretty low signal stability.
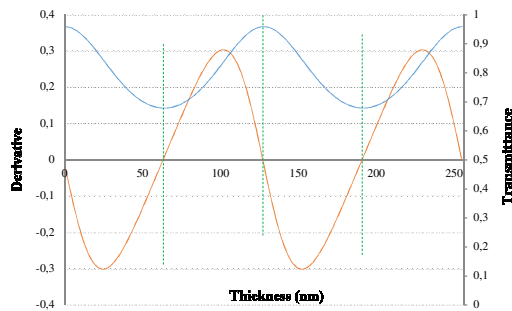

Figure 2.   Illustration of turning point monitoring technique.

B. Turning point monitoring

To overcome some of the limitations of TPM and especially the limited choice of monitoring wavelengths, Level Cut (or trigger point) monitoring (LC) provides an interesting alternative method. The principle is quite simple: the deposition of each layer i is stopped when the level of transmittance (or reflectance) measured at the control wavelength λ_i reaches the calculated theoretical level. Figure 3 illustrates the monitoring transmittance signal at 600 nm of a 255 nm thick layer with refractive index of 2.35. The measured signal follows the blue curve, crosses 5 extrema until reaching a transmittance of 0.73. Orange curve shows the remaining signal to the next extrema. The trigger point is reached when the transmittance is equal to the theoretically calculated value (green).
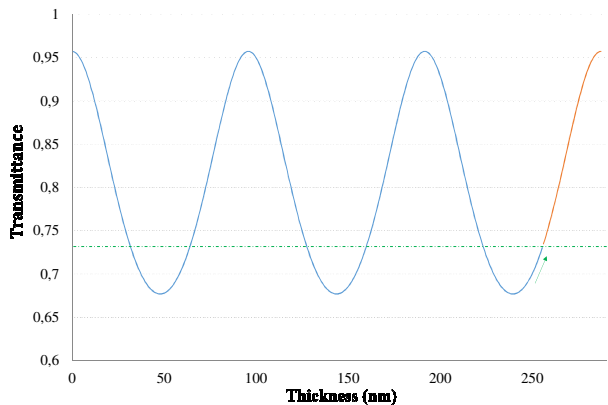

Figure 3.   Illustration of trigger point monitoring technique.

While this technique looks very attractive and easy to put into practice, the precision on the thickness of each layer is however conditioned by the control of several parameters. Indeed, it is important to precisely know the refractive index dispersion of the materials to be deposited. Any error on these values results in systematic errors before any layer deposition. It is also dependent one the distance from the previous and next extrema. Thus, it is mandatory to precisely select the proper monitoring wavelength.

IV.   ILLUSTRATION OF THE PROPOSED TECHNIQUES

To illustrate the potential of the proposed technique, we plotted in Figure 4 an overlay between theoretical (red) and experimental (green) transmission of a bandpass filter for 450 nm [9]. This filter is composed with more than 160 layers for a total stack exceeding 15 µm-thickness. It was optically monitored using different monitoring wavelengths and test glasses. One can see that the discrepancy between theory and experiment do not exceed 1 or 2%. One can show that such a result cannot be achieved if the error on the thickness of individual layers exceeds on 1% and are in average no larger than a few 0.1%.
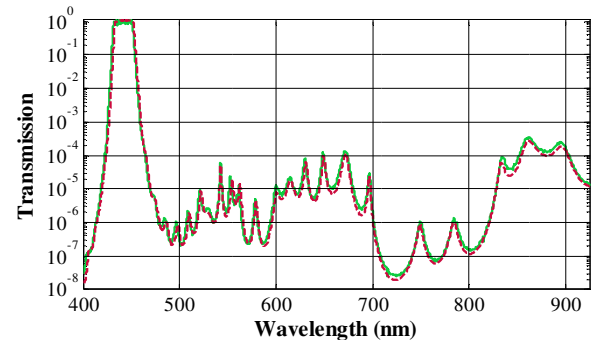

Figure 4.   Overlay between theoretical (red) and experimental (green) transmission of a bandpass filter for 450 nm.

REFERENCES

[1] K. D. Hendrix; C. A. Hulse; G. J. Ockenfuss; R. B. Sargent, "Demonstration of narrowband notch and multi-notch filters," Proc. SPIE 7067, Advances in Thin-Film Coatings for Optical Applications V, 706702 (29 August 2008).

[2] M. Scherer, J. Pistner, and W. Lehnert, "UV- and VIS filter coatings by plasma assisted reactive magnetron sputtering (PARMS)," in Optical Interference Coatings, OSA Technical Digest (Optical Society of America, 2010), paper MA7.

[3] T. Begou, H. Krol, D. Stojcevski, F. Lemarchand, M. Lequime, C. Grezes-Besset and J. Lumeau, "Complex optical interference filters with stress compensation for space applications", CEAS Space J 9(4), 441–449 (2017).

[4] R. R. Willey, "Simulation comparisons of monitoring strategies in narrow bandpass filters and antireflection coatings," Appl. Opt. 53, A27-A34 (2014).

[5] H. A. Macleod, Thin-Film Optical Filters, 4th ed., (CRC Press/Taylor & Francis, 2010).

[6] M. Vignaux, F. Lemarchand, T. Begou, C. Grezes-Besset and J. Lumeau, "In-situ optical monitoring of Fabry-Perot multilayer structures: analysis of current techniques and optimized procedures", Optics Express 25, 18040-18055 (2017).

[7] T. Begou, F. Lemarchand and J. Lumeau, "Advanced optical interference filters based on metal and dielectric layers", Optics Express 24(18), 20925–20937 (2016).

[8] S. L. Nadji, M. Lequime, T. Begou, C. Koc, C. Grèzes-Besset, and J. Lumeau, "New method of in situ monitoring of thin-film deposition using real time phase measurement", SPIE Advances in Optical Thin Films VI (Frankfurt, Germany), paper 10691-17, May 2018.

[9] T. Begou, H. Krol, D. Stojcevski, F. Lemarchand, M. Lequime, C. Grezes-Besset and J. Lumeau, "Complex optical interference filters with stress compensation for space applications", CEAS Space J 9(4), 441–449 (2017).

ULTRASHORT LASER BEAM IRRADIATION OF MESOPOROUS C-SI: LARGE SCALE TEXTURING FOR ENERGY HARVESTING

A. Talbi[1], A. Stolz[1], C. Boulmer-Leborgne[1], H. Rabat[1], M. Mikikian[1], M. Tabbal[2], G. O'Connors[3], D. de Sousa-Meneses[4], N.Semmar[1]*

1- GREMI-UMR 7344, CNRS-Université d'Orléans, 14 rue d'Issoudun, BP 6744, 45067 Orléans Cedex 2, France
2- Department of Physics, American University of Beirut, Bliss St. P.O. Box 11-0236, Riad el Solh, Beirut 1107 2020, Lebanon
3- NCLA/Inspire Laboratories, School of Physics, National University of Ireland Galway, University Road, Galway, Ireland
4- CEMHTI-UPR 3079, CNRS-Orléans, Avenue de la Recherche Scientifique, 45100, Orléans, France

Nadjib.semmar@univ-orleans.fr

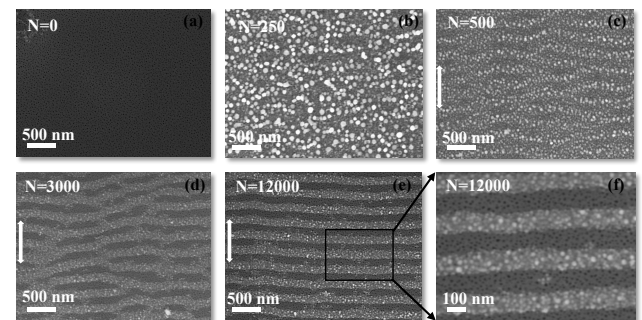*Topic : Surface functionalization and processing*

Abstract—**This work focuses on the surface modification of mesoporous c-Si by the direct laser beam irradiation. Picosecond and femtosecond beams are used to create nano and micro-scale structures leading to a huge change in the physical properties such as thermoelectric (low energy) and optic (high energy) properties.**

Silicon based materials still play a major role in microelectronics and microsystems, namely for energy conversion modules and harvesting that are more and more needed nowadays [1]. In this presentation the focus is done on the employment of laser beams for nano and micro structuring of mesoporous crystalline silicon. Our aim was to evaluate the mesoporous c-Si (MeP-Si) as a potential candidate material for thermoelectric applications.

In the GREMI-Lab this material (MeP-Si) was investigated in the frame of a regional project 'PoreuxTherm' and a national one 'PIA Tours-2015' during the period 2012 to 2018. The nano-architecture of the porous phase of c-Si was correlated to the macroscopic properties like optical, electrical and thermal ones that are important for energy harvesting microsystems and setups as reported in reference [2].

During the period 2014 to 2017 that corresponds to A. Talbi PhD-Thesis, we also started a parallel investigation of laser beam interaction with MeP-Si complex surface in order to understand the mechanisms of LIPSS formation in the pico and femtosecond regimes. The main results related to Nps based LIPSS (mainly LSFL, see Figure 1 were published in [3], and those related to their effect on thermoelectric properties are still in progress.

Thus, we will also focus on the influence of the large-scale surface nanostructures achieved with femtosecond beam source (@ 266 nm, 100 fs, 10 Hz) on the enhancement of the Seebeck coefficient and the electric resistivity/conductivity. As increasing the laser energy/dose, ablation mechanism takes place and induces the formation of large-scale micro-spikes structures as shown in Figure 2. These micro-spikes are likely similar to those obtained in several previous works to achieve black silicon surface namely for photovoltaic (PV) (See for

Figure 1: MeP-Si surface structures - NPs based LIPSS (LSFL) by ps and fs beams @266 nm.

example work from E. Mazur *et al.* on spie.org [4]). The laser processing setup and parameters that allow those structures fabrication will be illustrated. High resolution FTIR-spectroscopy applied on the spiked surface in the visible to IR range confirms the enhancement of absorption coefficient versus the size of micro-spikes.
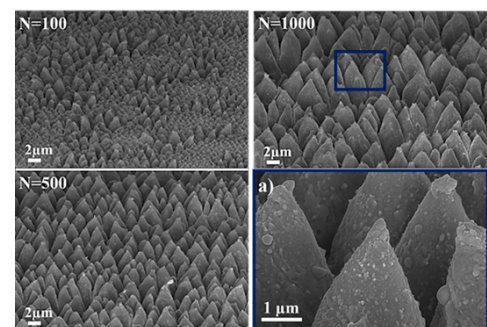

Figure 2: MeP-Si surface structures - Large-scale micro-spikes on MeP-Si by ps laser beam @266 nm.

ACKNOWLEDGMENT

REFERENCES

[1] Steven Chu & Arun Majumdar, "Opportunities and challenges for a sustainable energy future", Nature volume 488, pages 294–303 (16 August 2012).

[2] A. Melhem, D. de Sousa Meneses et al., "Structural, Optical, and Thermophysical Properties of Mesoporous Silicon Layers: Influence of Substrate Characteristics", The Journal of Physical Chemistry C 121 (14), 7821-7828 (2017).

[3] A Talbi, S Kaya-Boussougou, A Sauldubois et al., "Laser-induced periodic surface structures formation on mesoporous silicon from nanoparticles produced by picosecond and femtosecond laser shots", Applied Physics A 123 (7), 463 (2017).

[4] Black Silicon: 23 Years Later, http://spie.org/news/spie-professional-magazine/2019-april/black-silicon?SSO=1.

INKJET PRINTING AND LASER SINTERING OF Al:ZnO LAYERS FOR THE FABRICATION OF PLASMONIC SENSORS

O. Shavdina[1], C. Grillot[2], L. Hamraoui[1], F. Delorme[3], V. Bertagna[2], J. Nicolle[2], F. Giovannelli[3], C. Vautrin-Ul[2], N. Semmar[1], C. Leborgne[1], A. Stolz[1]

1. Université d'Orléans/CNRS 7344 UMR, Groupe de Recherches sur l'Energétique des Milieux Ionisés, Orléans, France
2. Université d'Orléans/CNRS UMR 7374, Interfaces, Confinement, Matériaux et Nanostructures, Orléans, France
3. Université de Tours/CNRS UMR 7347, Groupe de Recherche en Matériaux, Microélectronique, Acoustique et Nanotechnologies, Blois, France

e-mail of contact author: arnaud.stolz@univ-orleans.fr

Topic : Surface functionalization and processing

Our studies are focused on the inkjet-printing and laser sintering of aluminum-doped zinc oxide (AZO) layers. These layers turn out to be promising candidates for sensor applications due to their good transparency at visible range, high sensitivity and stability.

I. INTRODUCTION

Transparent conductive oxides films based on aluminum-doped zinc oxide nanoparticles are very promising candidates for a variety of applications such as gas sensors [1] or in optoelectronic applications [2]. This material possesses a wide band gap and exhibits good optical characteristics in the visible and near-infrared regions of the solar spectrum that could be interesting in the field of optical sensors. Undoped ZnO nanoparticles are highly sensitive toward the detection of flammable or toxic gases [3]. It was also demonstrated that the response of sensitivity for detection of acetaldehyde is 16 times higher for AZO nanoparticles than that in undoped ZnO NPs [4].

Our studies are focused on an additive method of the printing of AZO nanoparticles by the inkjet technology that include some advantages like single-step deposit of the functional material on flexible and rigid substrates, low-cost and contactless method [5]. Here, piezoelectric drop-on-demand nozzles are used to deposit a functional material in a state of suspension on a silicon or glass substrate. To prepare the ink, the AZO isotropic spherical nanoparticles were firstly synthesized by aqueous coprecipitation [6]. Then, the preparation of the solvent-based ink with AZO nanoparticles was performed with the control of the viscosity, ink stability and nanoparticles dispersion. Post-printing sintering of AZO films are conducted using a nanosecond pulsed laser.

Finally, the morphological and optical properties of the AZO films are characterized. The latter will act as active layers in future optical sensor to detect micro-pollutants in liquid water such as glyphosate and AMPA.

II. MATERIALS AND METHODS

A. Synthesis of Al doped ZnO spherical nanoparticles [7]

To prepare the Al doped (0,3%) ZnO nanoparticles, the method of aqueous coprecipitation was applied. AZO nanoparticles were obtained by a soda addition in aqueous cationic solution. The cationic solution was obtained by dissolving $Zn(NO_3)2,6-H_2O$ and $AlCl_3$ in demineralized water. The concentration of Zn is 1 M and Al concentration corresponds to 5 at % of Zn one. With this concentration of Al, the powder morphology was essentially formed by small isotropic particles close to 30 nm. Precipitation was made by the dropwise addition of NaOH solution. The precipitate obtained was centrifuged and washed with demineralized water. This step was repeated five times. The solid was finally dried at 80 °C.

B. Ink formulation and pattern generation

To prepare 7 mL of the ink, the previous synthetized AZO powder (0,125 g) was mixed with 1.875 mL of ethanol and 5 mL of ethylene glycol. Before printing, the dispersion was centrifuged during 1h and the glass and silicon substrates were cleaned in an ultrasonic bath, ethanol and acetone.

In order to generate the pattern from AZO dispersions, we used a commercial DMP – 2831 FUJIFILM Dimatix inkjet printer, with 10 pL cartridges. Droplet spacing was changed from 25 µm to 90 µm in order to find the best covering (Fig. 1 (b)). We also analyzed the influence of the holder temperature on the spreading effect of droplets, and the generation of drops by a stroboscopic method.
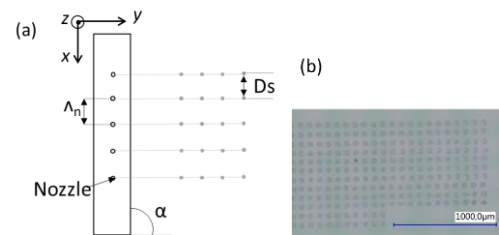

Figure 1. (a) Schematic of the printhead with inter-nozzle spacing Λ_n, drop space Ds, tilt angle α ; (b) Pattern with drop space fixed to 90 µm.

C. Laser sintering

In order to enhance the flatness and the density of the AZO layer, we proceed to a laser sintering with two nanosecond laser: a Nd:YAG laser at 355 nm and a KrF laser at 248 nm. Energy between 1.86 and 3.38 mJ were used. To focus the laser beam on the film layer, we used an opto-mechanical system able to move the sample. By this way, it was possible to adapt the dose of energy received by the film.

III. RESULTS

A. Properties of the inks and printing process

The viscosity and the particle size are the most significant parameters affecting the ink jettability. The values of viscosity required by the supplier should be between 10-12 cPs at operating temperature. In our case, the measured value of the viscosity at 20 °C for the AZO nanoparticle's dispersion is about 9 cPs. This value was optimal to prevent free flow of the ink on the substrate during the printing. In order to create the spherical drops on the substrate without any defect, it is important that the drop velocity is between 6 and 8 m/s. For this, the driving voltage was changed ranging from 20 to 40 V.

To form continuous uniform AZO layers without the drops overlapping and the particles accumulation at the edges of the droplets, we optimized the values of holder temperature as well as the spacing between them. We found that the optimal plateau temperature is 41°C and the drop spacing corresponding to 35 µm allows to create a continuous AZO layer.

B. Laser sintering : morphological properties

In order to produce particle fusion phenomenon, thin films have to absorb the laser irradiation. Fig. 2 shows the morphological state of two layers printed on a silicon substrate before (a) and after Nd:YAG ns-laser sintering (b), (c).
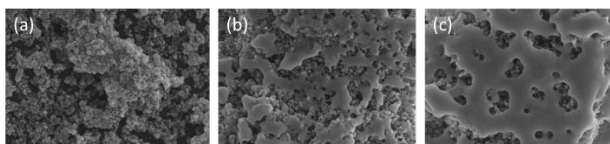

Figure 2. SEM micrograph of 2 AZO layers: (a) without laser sintering. After laser sintering with (b) E = 1.86 mJ; (c) E = 3.38.

We can observe that the spherical nanoparticles before laser treatment are densified on the substrate. This laser sintering phenomenon started at 355 nm under an energy of 1.86 mJ. At this energy surface morphology results on the neck formation. We also observe that the microstructure of the films is denser and more homogeneous in the case of 3.38 mJ. It can be explained by the starting of the coalescence process induced from laser sintering. In the case of KrF laser sintering with a tophat energy distribution, the surface morphology is obviously more uniform, and the sintering phenomenon is observed with an energy value about 45 mJ (Fig. 3).
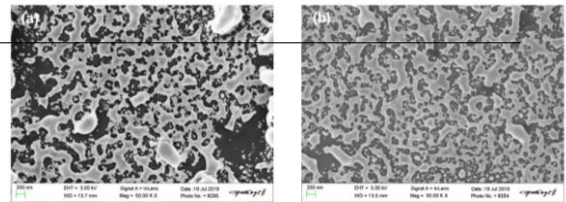

Figure 3. SEM micrograph of 3 AZO layers sintered at 45 mJ with : (a) 20 shots ; (b) 30 shots.

C. Optical properties

Optical transmittance spectra of the AZO thin films before and after the post-treatment in the wavelength from 350 to 1000 nm are compared in Fig. 4. These deposits remain mostly transparent above 70% except in the case of 4 layers. As the incident wavelength decreases down to ultraviolet region, the transmittance of the AZO films decreases with a sharp absorption edge at 350 nm. We can also observe that the transmittance increases slightly after the post-annealing laser.
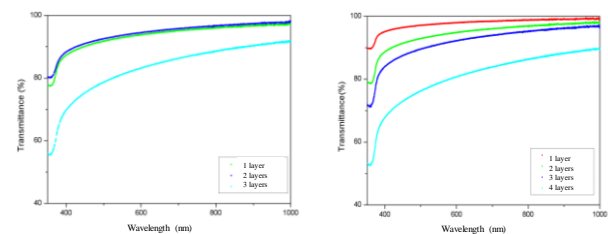

Figure 4. Optical transmittance spectra of the AZO films (a) before and (b) after laser sintering.

REFERENCES

[1] P. Lin, X. Chen, K. Zhang, H. Baumgart, " Improved Gas Sensing Performance of ALD AZO 3-D Coated ZnO Nanorods", ECS Journal of Solid State Science and Technology, vol. 7, 2018, pp. 246 –252.

[2] M. Maache, T. Devers, and A. Chala, " Al-doped and pure ZnO thin films elaborated by sol-gel spin coating process for optoelectronic applications" , Semiconductors, Vol. 51, 2017, pp. 1604–1610.

[3] R. Yoo, S. Cho, M.-J. Song, W. Lee, "Highly sensitive gas sensor based on Al-doped ZnO nanoparticles for detection of dimethyl methylphosphonate as a chemical warfare agent simulant", Sensors and Actuators B: Chemical, Vol. 221, 2015, pp. 217–223.

[4] Ran Yoo, Dongmei Li, Hyun Jun Rim, Sungmee Cho, Hyun Sook Lee, "High sensitivity in Al- doped ZnO nanoparticles for detection of acetetaldhyde", Sensors and Actuators, B: Chemical, Vol. 266, 2018, pp. 883–888.

[5] B. Andò, S. Baglio, A. R. Bulsara, T. Emery, V. Marletta and A. Pistorio, "Low-Cost Inkjet Printing Technology for the Rapid Prototyping of Transducers," Sensors, Vol. 17, 2017, pp. 1-11.

[6] P. Díaz -Chao, F.Giovannelli, O. Lebedeva, D. Chateigner, L. Lutterotti, F. Delorme, E. Guilmeau "Textured Al-doped ZnO ceramics with isotropic grains", Journal of the European Ceramic Society, Vol. 34, 2014, pp. 4247–4256.

[7] F. Giovannelli, A. N. Ndimba, P. Diaz-Chao, M. Motelica-Heino, P. I. Raynal, C. Autret, F. Delorme, "Synthesis of Al doped ZnO nanoparticles by aqueous coprecipitation", Powder Technology, Vol. 262, 2014, pp. 203–208.

Gratings with adiabatically varying depth for visible band optical applications

Andrei A. USHKOV[1*], Isabelle VERRIER[1], Thomas KAMPFE[1], Yves JOURLIN[1]

[1]Univ Lyon, UJM-Saint-Etienne, Laboratoire Hubert Curien, Saint-Etienne, France

*andrei.ushkov@univ-st-etienne.fr

Abstract A novel fabrication method for apodized diffractive structures is proposed and examined experimentally and theoretically. It combines the principles of laser interference lithography and a moiré effect in order to create high-quality subwavelength gratings with 2D adiabatic variation of depth. Synthesized structures can be used in optical security systems, plasmonic research and high-effective light couplers.

I. INTRODUCTION

Laser Interference Lithography (LIL) is a simple and quick surface patterning method [1]. As a one-shot procedure it allows the creation of macroscopic coherent periodic structures for nanotechnology. In particular applications avariable depth design can lead to attractive solutions. It is usually realized by variable dose ion- or electron-beam writing, which, however, have certain drawbacks like big time consumption, limited sample size (~mm) and a non perfect structure coherence at macroscopic scale. In order to adopt the LIL principle a number of approaches were proposed [2-3]. In this work we present a novel LIL-compatible fabrication method which utilizes the same interference moiré effect as in [2-3] but in a much simpler and more flexible way. We have synthesized and characterized apodized structures and performed theoretical calculations of grating profiles, which correspond perfectly to the AFM measurements. Our method can be used for optical security elements, plasmonic research and highly effective light couplers.

II. METHOD PRINCIPLES

In a LIL process with double exposure the intensity distribution on the resist surface is given by the sum of two sinusoidal patterns: $I_0(x) = A\left\{\sin\left(\frac{2\pi}{\Lambda_1}x\right) + \sin\left(\frac{2\pi}{\Lambda_2}x\right) + 2\right\}$, where A is the averaged intensity of a single exposure, modulation periods Λ_{1-2} depend on the LIL angle θ and laser wavelength λ [1], and x is the surface coordinate perpendicular to the modulation. Let us assume that $\Lambda_2 = \Lambda_1 + \Delta\Lambda, |\Delta\Lambda| \ll \Lambda_1$. In this case the intensity distribution over the resist surface can be represented as $I_0(x) \approx 2A\left\{\sin\left(\frac{2\pi}{\Lambda_1}x\right)\cos\left(\frac{2\pi}{\Lambda_{env}}x\right) + 1\right\}$ with the envelope function period $\Lambda_{env} \approx 2\Lambda_1^2/\Delta\Lambda \gg \Lambda_1$. The intensity formula clearly shows that the fine undulation with period Λ_1 is modulated by a large moiré pattern with characteristic size Λ_{env}. The conventional way to adjust the periods Λ_{1-2} is the control of LIL angle θ [2-3], i.e. $\Delta\Lambda \equiv \Delta\Lambda(\theta)$. However, this

approach is not precise at very small $\Delta\Lambda$ in order to get large Λ_{env}. In this work we present a novel fabrication method with a minor modification of a standard LIL setup (see Fig. 1a-b) for gratings with adiabatically varying depth. We propose utilizing the curved (spherical) wavefront of coherent point light sources that creates a set of slightly curved interference fringes in a photoresist layer after single LIL exposure. These fringes representing a family of hyperbolas are shown as colored lines in Fig. 1c, where the grating period being equal to the distance between lines slightly depends on coordinates (x,y). Consequently, small sample shifts of D < 1 mm between two LIL exposures can create a very small perturbation $\Delta\Lambda \equiv \Delta\Lambda(D) \ll \Lambda_1$ at any point of the resist surface, leading to a large macroscopic moiré pattern (see Fig. 1c).
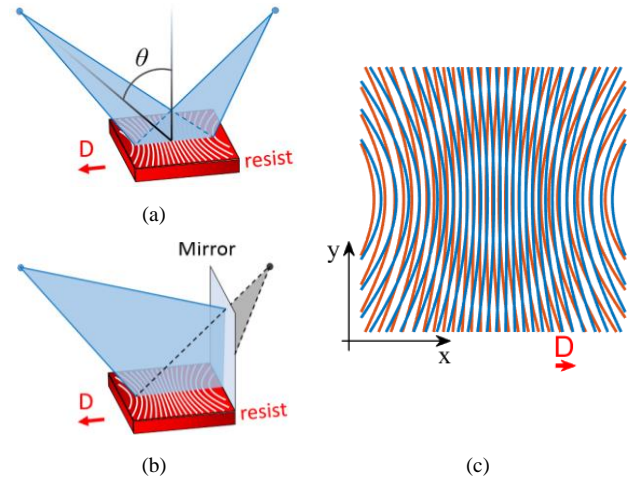

Fig. 1. LIL setups: (a) Dual Beam Interferometer and (b) Lloyd's Mirror Interferometer; (c) schematic representation of large moiré pattern (white ellipses) generated by double exposure LIL with a small sample shift D between the exposures. The vector **D** in (a-c) shows the direction and distance of sample shift.

These period perturbations are very small compared to the average period, but are sufficient to create a grating with a continuous variation of depths from zero to the maximum value. Let us notice that the proposed method is inherently 2D, i.e. the final structure is apodized in two dimensions, whereas grating grooves are still parallel to y direction everywhere.

III. MATERIALS AND FABRICATION

We used BK7 microscope glass slides as transparent substrates. They were cleaned in a wet bench in ultrasonic tanks of acetone and ethanol to remove chemical and mechanical pollutants. After drying in a nitrogen stream a thin film (~300 nm) of positive photoresist Shipley S1805 was spin-coated on the glass substrates and pre-baked in an

oven at 60°C for 1 min to evaporate the solvent and improve the adhesion. In order to create subwavelength diffraction gratings in the visible range we take Λ_1=300 nm. A dual-beam interferometer with a He-Cd laser at λ=442 nm was upgraded by a manual linear translation stage on the sample support to precisely control the sample shift D precisely. The samples were pre-exposed uniformly for 20 s with the beam intensity $I = 250$ µW/cm² in order to set the resist in a linear regime and get a smooth sinusoidal grating profile. Between two equal LIL exposures for t_{exp}=15 s each with intensity $A \equiv 2I = 500$ µW/cm² the samples were shifted by different distances D to create structures with various sizes of the moiré pattern. Finally, samples were developed in Microposit MF-319 developer for 4 s at the temperature 8°C in order to dissolve the exposed resist parts resulting in the desired surface structuration. Fig. 2 shows the prepared diffraction gratings with different shifts D. Black lines crossing the structures are moiré arcs (see Fig. 1c) of zero grating depth.
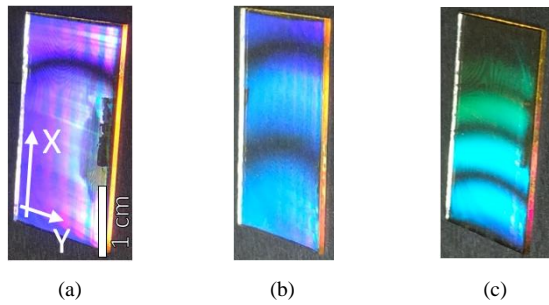

(a)   (b)   (c)

Fig. 2. Images of variable depth gratings of period Λ=300 nm in white lighting with different size of moiré pattern. The sample shift D=180, 400, 600 µm for (a)-(c) respectively is parallel to X-axis.

IV. CHARACTERIZATION

Fig. 3a demonstrates AFM measurements of the grating depth along the central line parallel to the x direction. The characterized grating of period 300 nm and shift D = 240 µm continuously and adiabatically covers all depth values from zero to 105 nm at a macroscopic distance ~3 cm. For every depth value we can consider at least 100 grating periods of almost equal depth, their profile can be simulated locally as for a standard uniform 1D grating with some effective exposition time $0 \ll T_{eff} \ll 2t_{exp}$. Fig. 3b reveals the form of structure regions with depths of 105 and 48 nm, with a good correspondence between experimental AFM data and numerical simulations of the resist development.
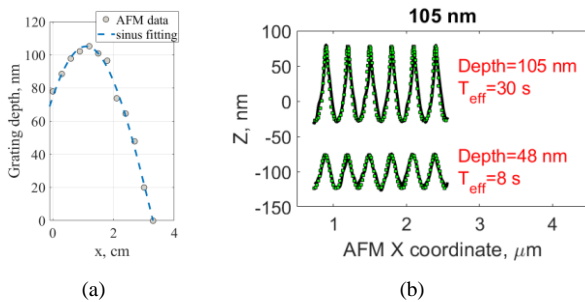

(a)   (b)

Fig. 3. (a) AFM-measured depths along the surface of variable depth grating (white dots) and sinusoidal fitting (blue dashed line). (b) AFM-measured grating profiles (black lines) and their numerical simulation (green squares) for depths 105 and 48 nm.

Numerical simulations are based on the experimentally measured resist sensitivity curve (Fig. 4a), the optical properties of glass and resist at $\lambda = 442$ nm and the exact field distribution in the resist layer (Fig. 4b). Furthermore, we implemented an iterative process to take into account the isotropic nature of the dissolution process [4].
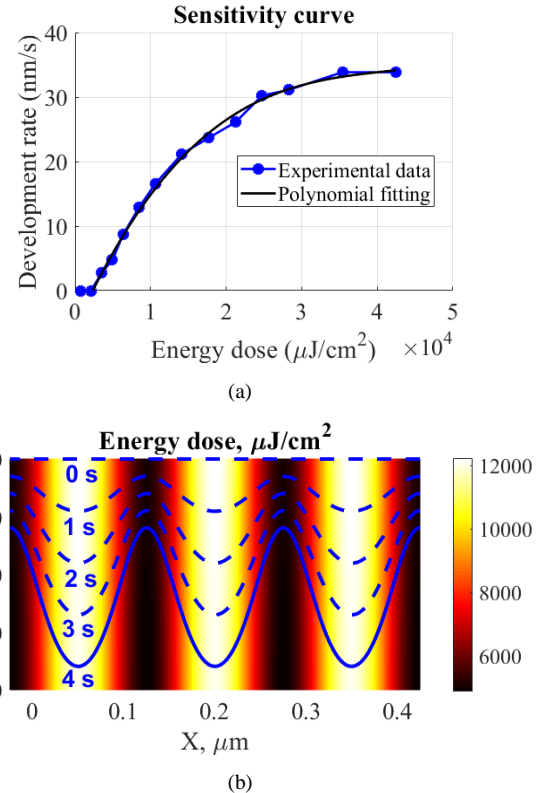

(a)

(b)

Fig. 4. (a) Experimentally measured resist development rate; (b) Iterative numerical simulation of resist development process for a region of depth 48 nm of a variable grating (blue solid and dashed lines for development times 0-4 s). The background color represents the exposition energy dose.

CONCLUSION

To conclude, we have presented a novel simple and flexible fabrication method for apodized nanostructures. It was demonstrated that it allows creating subwavelength gratings with macroscopic size and adiabatically varying depth, which are ready for further technological steps depending on the research area. The numerical simulation of resist development is in a very good correspondence with AFM measurements. The size of moiré patterns depends on the sample shift D and can be predicted theoretically. Our method is developed for optical security elements, plasmonic research and highly effective light couplers.

REFERENCES

[1] J.H. Seo et al., "Nanopatterning by laser interference lithography," J. Nanosci. Nanotechnol., vol. 14, pp. 1521—1532, 2014.

[2] H.-G. Fröhlich and R. Kashyap, "Two methods of apodisation of fibre-Bragg-gratings," Optics Communications, vol. 157, pp. 273—281, 1998.

[3] W.R. Tompkin, R. Staub, A. Schilling and H.P. Herzig, "Diffraction from metallic gratings with locally varying profile forms," Opt. Lett., vol. 24, pp. 71—73, 1999.

[4] B. Mello, C.R. Lima and L. Cescato, "Developed profile of holographically exposed photoresist gratings," Appl. Opt., vol. 34, pp. 597—603, 1995.

ACTIN DYNAMICS AND CELLULAR FORCES IN VIVO AND IN VITRO

Sara Bouizakarne[1,2] Alice Nicolas[1] Jocelyn Etienne[2] Gregoire Michaux[3]

Abstract— The interplay between genetic and mechanical regulation in morphogenesis is crucial in determining the properties of a model system. While genetics contribute in releasing biochemical signals that regulate cell activity and physical features, mechanics provide another layer for understanding the embryonic development. Using *C.elegans* embryos as in vivo model and A431 epithelial cells as an vitro model, we examine the role of actin organization during the morphogenetic step of elongation of the worm. We look at the mechanical anisotropy and investigate the link with the embryo actin organization.

I. INTRODUCTION

Morphogenesis is a developmental process by which shape is acquired. During morphogenesis, tissues change their shape, a process often mediated by myosin-driven cell contractility. The C.elegans embryo has been established as a model to investigate the relationship between cell contractility and shape changes.

One important morphogenetic step in C.elegans is elongation, that converts the embryo from a bean-shaped embryo to the characteristic elongated worm shape. Elongation occurs via changes in cells' shapes that depend on the forces created by the embryonic cells and the resistance of the biological tissue.

Actin organization was shown to play an essential role during this elongation [1]. Its transition from disordered, thin filaments to parallel thick bundles is suspected to be at the origin of an anisotropic tension that correlates with a planar polarization of the cortex and the elongation of the embryo [2].

Here we address the role of actin organization on embryonic tensions. First, we use laser ablations in the actin cortex to probe actin tension during the elongation of the embryos. The ablation is performed in a rectangular-shaped torus, to mechanically separate a small patch of actin from the rest of the cortex and allow the analysis of the tissue relaxation with well-defined boundary conditions.

Second, we develop an in vitro model that mimics actin organization during elongation in order to correlate it with cellular forces. Using A431 as an epithelial cellular model, we correlate actin organization with cellular forces. Actin organization will further be tuned either via chemical or mechanical patterning on soft hydrogels, so to explore the mechanical effects of the actin patterns that are observed in vivo.

[1]Laboratoire des Technologies de la Microelectronique, 38000 Grenoble
[2]Laboratoire Interdisciplinaire de Physique, 38402 Saint-Martin-d'Hres
[3]Institut de Genetique et de Developpement de Rennes, 35000 Rennes

Exploitation of both techniques is expected to provide a better characterization of actin dynamics during the course of C.elegans embryonic elongation.

REFERENCES

[1] *The interplay of stiffness and force anisotropies drives embryo elongation*, Thanh Thi Kim Vuong-Brender, Martine Ben Amar, Julien Pontabry, Michel Labouesse, eLIFE (2017).

[2] *Force Transmission between Three Tissues Controls Bipolar Planar Polarity Establishment and Morphogenesis*, Ghislain Gillard, Ophelie Nicolle, Thibault Brugiere, Sylvain Prigent, Mathieu Pinot, Gregoire Michaux, Current Biology 29, 19 (2019).

Micro-fabrication using synchrotron radiation at SOLEIL

P. Da Silva[1], P. Mercère[1], D. Bourrier[2], F. Bouamrane[1,3]

[1]Synchrotron SOLEIL, 91192 Saint-Aubin, France
[2]LAAS-CNRS, 31077 Toulouse, France
[3]Unité mixte de Physique CNRS-THALES, 91767 Palaiseau, France

Topic : lithography

Abstract—**LIGA, German acronym for Lithography, Electroplating, Moulding provides structures with heights up to a few hundred micrometers with high aspect ratio, complex shapes with micrometer lateral resolution in a wide range of materials: polymers, metals and ceramics. This technology relies on synchrotron radiation to obtain high X-ray flux, extreme precision and depth of field**.

Since 2009 a dedicated LIGA station is available at SOLEIL on the Metrology beamline allowing to perform deep X-ray lithography (DXRL). This beamline is open to both academic and industrial research projects. In 2014, the station was up-graded to work both with polychromatic (white) and monochromatic (Si (111) cristals nowadays and access to multi-layers diffraction grating in the future) beams in a strait forward and reversible manner. The top-up mode injection in the SOLEIL storage ring which was one main characteristic of synchrotron provides very stable current which is favorable for precise lithography (time and thermal stability). Two main injection modes with current values of 450-500mA and 80-100mA are possible within the year. Higher current values provide high photons flux for low sensitivity positive resists (PMMA…) for deep structures fabrication and for monochromatic exposures. Low current values in the other hand are well suited for sensitive (negative) resists and higher resolution structures as thermal impact during exposure is weak. This high versatility is a unique feature among LIGA beamlines in the world. It allows to perform standard micro-fabrication (micrometer resolution) but also basic and applicated research activities in order to better understand, improve the technology and move forward for higher resolution (sub-micron) and more demanding structures.

LIGA masks, resists preparation, chemical development, metal electroplating and all related metrology steps are made at the Unité Mixte de Physique CNRS-THALES using the clean room dedicated facilities.

To show the wide field of application of the LIGA technology some accomplishments in different scientific domains will be presented.

The interest for specific X-rays optical parts devoted to imaging, beam forming and diagnostic is ever rising and demanding on synchrotron facilities as more developments needing higher accuracy are requested both for samples, optical devices and beam line characterization.

For instance, beamlines at SOLEIL need specific (accurate micrometric to sub-micrometric dimensions with high aspect ratio, up to 30) optical devices working in the high energy X-rays (range from about 5 to 25 keV or more) which would need to be customized as no such devices are available. The high energy of the photon beams imposes the use of heavy material such as gold and features with high aspect ratios. Deep X-ray Lithography can fulfil all these requirements as for :

- knife-edge structures for beam characterization
- pinholes with sub to few microns diameter as defining apertures in X-ray Coherent Diffraction Imaging or X-ray Ptychography experiments
-Hartmann grids for accurate wavefront measurements in the hard X-ray region
-phase gratings for X-ray imaging [1] and Fig. 1.

Figure 1: Phase gratings for X-ray imaging
Electropalted gold over silicon
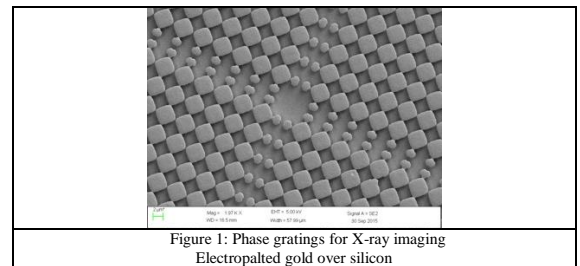
Not only related to the synchrotron facilities demand, LIGA micro-structures can respond to a wide range of specific micro-structures which need both micrometric resolution, high aspect ratio with perfectly vertical walls (due to the very low vertical divergence which is a specific properties of synchrotron radiation) of a few hundred micrometers, up to millimetric height. No other micro-fabrication technology can provide such properties. For example in the field of more conventional optics, development of a non-mechanical infrared laser deflection device or coherent combination of a high number of self-amplificated optical fibre laser for high energy laser [2] were conducted with THALES and THALES/ONERA respectively using micro-structured electro-optic ceramics as phase modulators. In the growing field of THz one challenge is the miniaturization of the sources. LIGA was a competitive technology to fabricate Slow Wave Structure (SWS) made of high purity copper, key part of the THz electronic source working under vaccum combined with up converters [3]. Examples of complex shaped optical components such as multiplexers for THz beam, combining 2, 3 and up to 5 different wavelengh [4] was also conducted.

Metamaterials (MM) due to their unique possibility of structural design are suitable materials to construct optical devices (lenses, switches, modulators...) operating in the THz range with unusual properties as negative refraction, sub-wavelength focusing… LIGA technology combined with ultrasonic manufacturing with micrometric structural dimensions within tens of micrometers depth which are necessary to expect resonances in the THz range using dielectric materials (low losses and isotropic properties compared to metals) [5].

These last years some developments in the fabrication of higher resolution LIGA masks and study of X-ray resists with higher sensitivity and aspect ratio capabilities were undertaken as they are key parameters to improve the technology. Some promising results for LIGA mask optimization on low absorbing substrate were obtain as in a collaboration within the RENATECH network. Some work will be presented using both classical UV masker (Fig. 2) and a UV stepper in order to reach sub-micronic dimension structures.
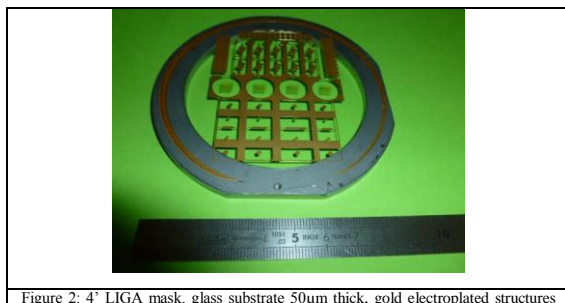

Figure 2: 4' LIGA mask, glass substrate 50µm thick, gold electroplated structures

20µm thick

REFERENCES

[1] Montaux-Lambert A., Mercère P., Primot J. "Interferogram conditioning for improved Fourier analysis and application to X-ray phase imaging by grating interferometry" Optics Express., 23(22): 28479-28490, 2015.

[2] C. Bellanger, A. Brignon, B. Toulon, J. Primot, F. Bouamrane, T. Bouvet, S. Megtert, L. Quetel, T. Allain, "Design of a fiber-collimated array for beam combining", Optical Engineering 50(2), 025005, 2011.

[3] C. Paoloni, A. Di Carlo, F. Bouamrane, T. Bouvet, A. J. Durand, M. Kotiranta, V. Krozer, S. Megtert, M. Mineo, V. Zhurbenko, "Design and realization aspects of 1-THz cascade backward wave amplifier based on double corrugated waveguide" Electron devices, IEEE trans. Vol. 60, iss. 3, 1236-1243, 2013.

[4] V. S. Jagtap, A. F. Dégardin, A. J. Kreisler "Reflection Phase Gratings: An Elegant Way of THz Beam Multiplexing" Fall OSA Optics & Photonics Congress, San Jose, USA, 2009.

[5] C. Dupas, S. Guillemet-Fritsch, P.-M. Geffroy, T. Chartier, M. Baillergeau, J. Man- geney, J.-F. Roux, J.-P. Ganne, S. Marcellin, A. Degiron, and É. Akmansoy, "High permittivity processed SrTiO3 for metamaterials applications at terahertz frequencies," Scientific Reports, vol. 8, no. 1, p. 15275, 2018.

Micro/nanotechnologies to improve concentrated photovoltaics systems

M. Darnon[1], M. Volatier[1], M. de Lafontaine[1,2], P. Albert[1,3], C. Laucher[1], G. Hamon[1], E. Pargon[2],
L. Bechou[3], S. Fafard[1], V. Aimez[1], A. Jaouad[1]

[1] *LN2,* CNRS, Université de Sherbrooke, 3IT, Sherbrooke, QC, Canada
[2]*LTM,* CNRS, Université de Grenoble Alpes, Grenoble, France
[3]*IMS,* CNRS, Université de Bordeaux, Bordeaux, France
(*e-mail of contact author*): maxime.darnon@usherbrooke.ca

Intégration et applications des micro/nanotechnologies ; Gravure, lithographie et nano-patterning

We present here how micro and nanotechnologies can be employed to enable the fabrication of high efficiency solar cells with innovative architectures, especially designed to facilitate the integration of the cells into system, and to improve the final system efficiency.

I. INTRODUCTION

With the current challenges of global warming, it is now urgent to convert fossil fuel-based electricity generation into renewable energy systems. Among all renewable energy systems, concentrated photovoltaics provides the highest photovoltaic conversion efficiency, and is considered as a competitive solution for utility scale photovoltaics implementation in high direct normal irradiance regions. Concentrated photovoltaics relies on optical concentration of sunlight onto a small-surface high-efficiency solar cell. For instance, commercial systems use multiple Fresnel lenses that concentrate ~500x the sunlight on few mm^2 solar cells, with system efficiency above 30% (see fig.1). The optical concentration makes expensive solar cells affordable while it also provides a premium on efficiency.

Commercial high efficiency solar cells are triple junction solar cells made of III-V heterostructures grown on germanium by MOCVD, that form three P-N junctions - each converting part of the sunlight with a high efficiency - series-connected by tunnel junctions. There has been huge efforts in the literature to optimize the materials quality as well as design the structure to maximize the efficiency [1]. However, the transformation of such materials into actual solar cells remains relatively basic with evaporation and metal lift-off for electrodes patterning. Solar cells are finally integrated into concentrated photovoltaics modules using rather expensive methods such as wire bonding.

Using micro-nanotechnologies for solar cells fabrication provides a good opportunity to fabricate innovative architectures of solar cells, that can be either cheaper or especially adapted for the integration of cells in modules to reduce the modules fabrication cost. We present here few processes specifically developed in this objective.

II. MATERIAL AND METHODS

All the experiments are performed using commercial materials provided by our industrial partners. They contain triple junction (InGaP / (In)GaAs / Ge) materials on 4" germanium wafers. The wafers are cut into ~1 to 2 cm^2 coupons and are processed individually in our cleanroom.

III. RESULTS

A. Plasma etching

Conventional solar cells are isolated using a diamond saw that creates damage at the mesa sidewalls and is hardly usable for small cells. Besides, only rectangular cells can be isolated with a diamond saw.

We developed a low damage III-V materials plasma etching process in replacement of the conventional diamond saw dicing. Using a $SiCl_4$ / Cl_2 / H_2 plasma, we managed to etch non-selectively the complex stack of materials (InGaP / (In)GaAs) with limited damage [2]. As a matter of fact, solar cells with multiple holes etched with such a process do not present any reduction of the cell efficiency under 500x illumination compared to cells without holes (see figure 2).

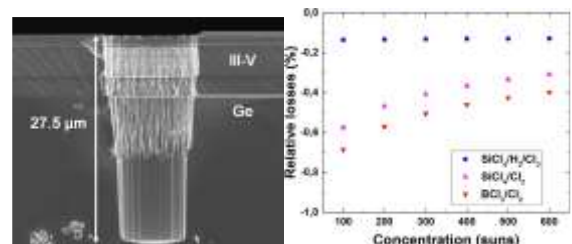Deep plasma etching of germanium has also been investigated and through-wafer etching processes were

Figure 1. Picture of a commercial 12 modules concentrated photovoltaic system installed at Université de Sherbrooke. It embeds 14,400 couples of Fresnel lens /solar cell with an optical concentration ~500x.

Figure 2. SEM picture of a 27.5μm deep hole etched in the stack of III-V materials and germanium, and relative electrical losses associated with plasma-induced damage [2].
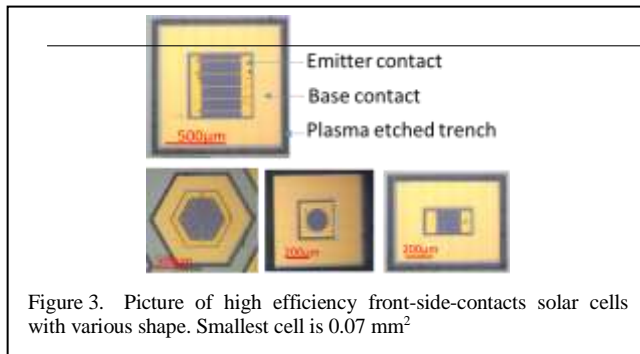
Figure 3. Picture of high efficiency front-side-contacts solar cells with various shape. Smallest cell is 0.07 mm²

Figure 5. Picture and electrical characteristics of high voltage / low current solar cells [6]

developed to replace saw-dicing by plasma dicing [3].

Using III-V and Germanium plasma etching processes, we enabled the fabrication of solar cells with any shape definable by lithography. We also reduce the dicing line width down to ~20 µm, compared to >50 µm for most advanced dicing tools, which reduces the waste of materials, especially for small cells surface. Finally, we enabled the fabrication of 0.07 mm² diced solar cells with good electrical performance [4], which cannot be fabricated otherwise. Example of solar cells fabricated with this method are presented figure 3.

B. Light-induced electrode plating

Vacuum-based processes such as evaporation or sputtering are quite expensive compared to wet-bench processes. In addition, lift-off processes are known to provide high defectivity. We developed a complete metallization process without vacuum-based processes and that avoids lift-off processes for the front electrode fabrication [5]. Using an external light source and the photovoltaic effect, we managed to deposit Ni, Au and Ag directly on our material without needing a seed layer nor external circuitry. The solar cell material under illumination provides the current needed for electroplating, as illustrated figure 4.

C. Innovative cells architectures

Using conventional micro/nano fabrication processes, innovative cells architectures can be envisioned.

Suppressing the wire bonding methods would be advantageous at the module level to improve the reliability and ease the fabrication. We developed several architectures of solar cells with either the two contacts on the front side or on the back side [4]. With such architectures, mass reflow processes can be used to solder both contacts on the cell receiver, avoiding the need for expensive wire bonding. As an example, solar cells with two contacts on the front side are presented figure 3.

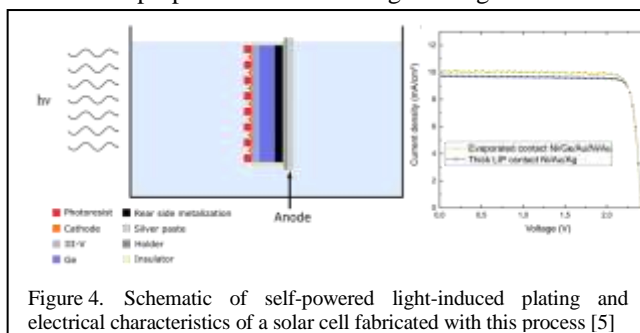We also proposed to fabricate high-voltage / low current
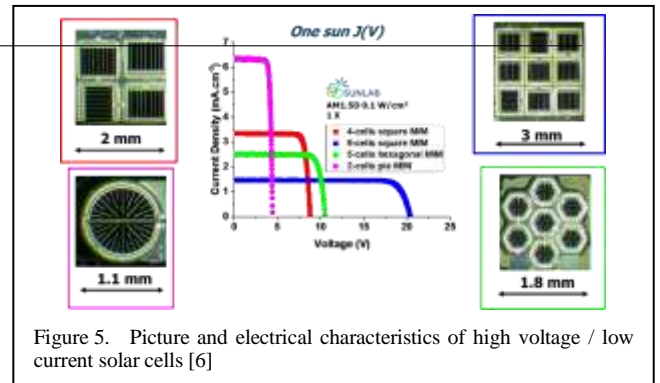
solar cells to reduce the Joule losses at the module level. For that, the cells are split into smaller cells that are monolithically interconnected at the wafer level using microfabrication methods. This structure is enabled by the plasma dicing methods presented above and by the architecture of front-side-contacted solar cells. Figure 5 shows few examples of high voltage / low current solar cells with various designs. The electrical characteristics under one sun illumination are also reported figure 5.[6]

IV. CONCLUSION

Micro and nano fabrication processes provide a high potential for improving the way concentrated photovoltaic systems are fabricated. Multiple processes have been proposed to reduce the fabrication cost and/or enable new architectures that improve the system performance/cost ratio.

REFERENCES

[1] C. Algora, I. Rey-Stolle, "Handbook of Concentrator Photovoltaic Technology", Wiley, 2016

[2] M. de Lafontaine, E. Pargon, C. Petit-Etienne, G. Gay, A. Jaouad, M-J. Gour, M. Volatier, S. Fafard, V. Aimez, M. Darnon, "Influence of plasma process on III-V/Ge multijunction solar cell via etching". Solar Energy Materials and Solar Cells, 195, 49-54, 2019

[3] M. Darnon, M. De Lafontaine, M. Volatier, S. Fafard, R. Ares, A. Jaouad, V. Aimez, « Deep germanium etching using time multiplexed plasma etching", J. Vac. Sci. & Technol. B, 33(6), 060605, 2015.

[4] P. Albert, A. Jaouad, M. Darnon, C. E. Valdivia, M. Volatier, Y. Deshayes, K. Hinzer, L. Bechou, V. Aimez, "Front-Contacted Multijunction Micro Solar Cells: Fabrication & Characterization", 14th Concentrated Photovoltaics Conference, Puertollano, 2018.

[5] C. Laucher, G. Hamon, A. Turala, M. Volatier, M. Darnon, V. Aimez, A. Jaouad, "Self-Powered Light-Induced Plating for III-V/Ge Triple-Junction Solar Cells Metallization", submitted to Progresses in Photovoltaics and Solar Cells.

[6] P. Albert, A. Jaouad, M. Darnon, G. Hamon, C. E. Valdivia, M. Volatier, Y. Deshayes, K. Hinzer, L. Béchou, V. Aimez, "High-Voltage Low-Current Multijunction Monolithic Interconnected Microcells", 15th Concentrated Photovoltaics Conference, Fès, 2019

Figure 4. Schematic of self-powered light-induced plating and electrical characteristics of a solar cell fabricated with this process [5]

Polymer-based photonic crystal VOC sensors fabricated by PMMA hot embossing

Lydie Ferrier, Dylan David, Jean-François Chateaux, Sébastien Cueff, Cécile Jamois, Taha Benyattou

Université de Lyon, Institut des Nanotechnologies de Lyon (INL), INSA Lyon, 69621 Villeurbanne, France

lydie.ferrier@insa-lyon.fr

Topic : Nano-patterning

Abstract—**A large-scale, high throughput and low cost photonic crystal fabrication process based on polymer hot embossing is presented. This simple patterning process, allowing to achieve lateral dimensions at the nanoscale, is used to realize polymer-based photonic crystal VOC (Volatile Organic Compounds) sensors.**

I. INTRODUCTION

This study presents the design and fabrication of an optical VOC (volatile organic compound) sensor based on a polymer photonic crystal. In order to achieve low cost and versatile sensing platforms, we aimed at developing new technological tools to produce low-cost, large scale, high precision and high throughput devices, yielding high resolution and compatibility with a large variety of polymer-based materials.

In particular, we focus our study on Poly(methyl methacrylate) (PMMA) which has the property to swell upon exposure to organic solvents [1,2] and presents a wide range of transparency (400nm-2µm). Combined with the extreme sensitivity of photonic crystal resonances to refractive index and geometry of the structure (period, filling factor) [3], devices with patterned polymer [4] or covered with it [5] should exhibit an increase of sensitivity to VOC.

II. DEVICE DESIGN

A photonic crystal (PhC) is a periodically patterned dielectric structure, with a periodicity that is often in the micron or submicron range. Thanks to its periodicity, such a structure can exhibit various exciting optical properties like optical resonances, light confinement, enhanced light-matter interaction, etc. In particular, PhCs support optical resonances at very specific wavelengths that are strongly depending on the PhC's geometrical parameters (period, filling factor). Any variation in these parameters (e.g. a swelling induced by the exposure to an organic compound) should lead to a shift of the resonance wavelength. The goal of the PhC design is to find the parameters leading to the largest wavelength shifts, i.e., yielding the largest sensitivity to any small change in the dimensions of the device. In this study, the PhC material is a low refractive index material ($n_{PMMA} \approx 1.5$ in the visible range), for which the best design requires a thick (≈ 800nm) patterned PMMA layer if it is placed on top of a Si substrate. As it would be easier to

pattern a thinner PMMA layer, an alternative structure consists in fabricating the polymer photonic crystal on top of a gold mirror in order to increase the light confinement. In the multilayer structure presented in Figure 1, with a period a=600nm, a filling factor of 50% and a thickness h_{PMMA}=400nm, a resonance located at 710nm is expected (RCWA numerical simulations). This resonance is very sensitive to the photonic crystal dimensions, as shown in Figure 2: a redshift of 9nm is obtained when the polymer gains 1.25% in volume upon exposure to VOC.

In order to demonstrate that this design is compatible with low-cost and large-scale fabrication processes, we developed PMMA hot embossing at the nanoscale: the goal is to achieve lateral dimensions smaller than the operation wavelength of the device, similarly to the structure shown in Figure 1
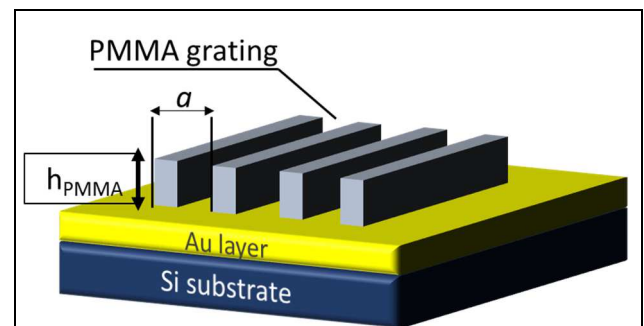

Figure 1. Schematic view of the structure design : a PMMA photonic crystal is patterned on a metallic (Au) mirror.
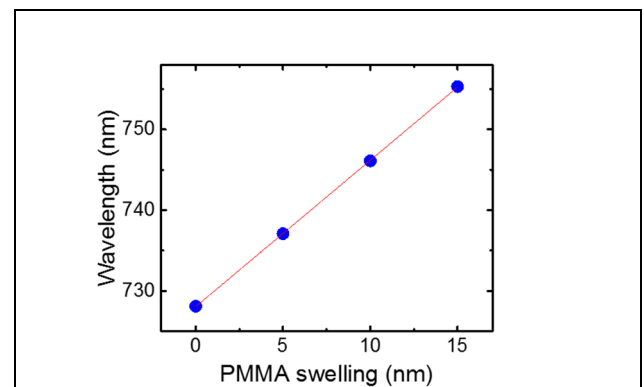

Figure 2. Peak resonance wavelength as a function of the PMMA swelling (thickness and filling factor).

III. EXPERIMENTAL METHODS

A. Stamp fabrication

We used a hard stamp fabricated on a SOI (220nm) platform as mold for the thermal imprint. The stamp patterns are defined using electron beam lithography on a HSQ layer (300 nm). The resulting photonic crystal patterns consist of 1D gratings (lattice period a= 250nm, width of stripes w= 175nm) as well as 2D gratings with square pillars (w=600nm) arranged in a square lattice (a=750nm). Then the patterns are transferred into a 220nm silicon layer by using ICP etching.

B. Sample preparation and thermal nanoimprint

The hot embossing process used to replicate the mold on PMMA layers follows conventional steps: first, the PMMA thermoplastic layer is spin-coated onto the substrate with a spin speed leading to a PMMA layer with 400nm thickness. Then the sample is baked on a hot plate at 150°C during 1min. In order to improve the nanoimprint process and prevent any sticking of the mold to the sample, the Si stamp is covered by an anti-adhesive layer [6,7] : the coating is carried out in a closed beaker by evaporating a drop of trichlorosilanes onto the Si stamp, at room temperature.

The thermal nanoimprint is performed on a thermal press at a fixed pressure (200bar) and different temperatures. In a first step the sample and the stamp are heated to the desired temperature. Then, the pressure is applied on both sample and stamp for 45min. After 45min, the heating is turned off while the force is being maintained. When a temperature $<$Tg is reached (70°C), the sample and the stamp are demolded. A range of temperatures have been tried, from 130°C to 200°C keeping the same pressure and duration of thermal imprint.

C. Results

Scanning electron micrograph of fabricated structures are shown in Figure 3. 1D photonic crystal with period of 270nm and stripes width as small as 75nm have been obtained for a temperature of 170°C. The 2D gratings have a period of 750nm with square holes of 600nm.

AFM measurements of the 1D and 2D gratings to determine the thickness of the imprinted structures are still under process, as well as optical characterizations.
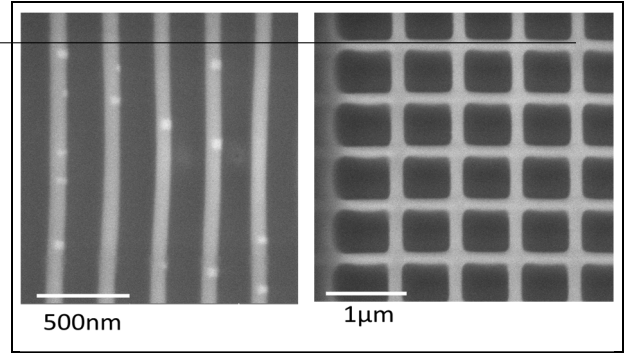

Figure 3. Scanning electron microscope images of 1D and 2D PMMA structures realized by thermal nanoimprint.

IV. CONCLUSION

In this work, we demonstrate a versatile approach to fabricate polymer-based photonic crystal sensors by hot embossing. We obtain 1D as well as 2D periodic PMMA grating with subwavelength resolution. The PMMA property of swelling upon exposure to VOC is exploited in this study to develop a new class of photonic crystal sensors by combining this property with the high sensitivity of photonic crystal resonances to the modification of the structure geometry.

REFERENCES

[1] Papanu, J. S., Hess, D. W., Soane, D. S., & Bell, A. T. (1990). Swelling of poly (methyl methacrylate) thin films in low molecular weight alcohols. *Journal of applied polymer science*, *39*(4), 803-823.

[2] Chen, J. K., Wang, J. H., Cheng, C. C., Chang, J. Y., & Chang, F. C. (2013). Polarity-indicative two-dimensional periodic relief gratings of tethered poly (methyl methacrylate) on silicon surfaces for visualization in volatile organic compound sensing. *Applied Physics Letters*, *102*(15), 151906.

[3] Fenzl, C., et al. (2014). Photonic crystals for chemical sensing and biosensing. Angewandte Chemie International Edition, 53(13), 3318-3335.

[4] Clevenson, H., Desjardins, P., Gan, X., & Englund, D. (2014). High sensitivity gas sensor based on high-Q suspended polymer photonic crystal nanocavity. Applied Physics Letters, 104(24), 241108.

[5] Smith, C. L., Lind, J. U., Nielsen, C. H., Christiansen, M. B., Buss, T., Larsen, N. B., & Kristensen, A. (2011). Enhanced transduction of photonic crystal dye lasers for gas sensing via swelling polymer film. Optics letters, 36(8), 1392-1394.

[6] Beck, M., Graczyk, M., Maximov, I., Sarwe, E. L., Ling, T. G. I., Keil, M., & Montelius, L. (2002). Improving stamps for 10 nm level wafer scale nanoimprint lithography. Microelectronic Engineering, 61, 441-448.

[7] Schift, H., Saxer, S., Park, S., Padeste, C., Pieles, U., & Gobrecht, J. (2005). Controlled co-evaporation of silanes for nanoimprint stamps. Nanotechnology, 16(5), S171.

Impact of plasma etching process exposure on the integrity of AlN and AlGaN layers integrated in GaN heterojunction transistors (HEMTs)

Fesiienko Oleh[a,b], Erwine Pargon[a] Hassan Maher [b], Camille Petit-Etienne[a], Ali Soltani [b], Maxime Darnon [b]

[a]Laboratoire des Technologies de la Microélectronique (LTM), CNRS, Université Grenoble Alpes, 17 avenue des Martyrs, 38000 Grenoble, France
[b]Laboratoire Nanotechnologie Nano systèmes (LN2) - CNRS UMI-3463, Université de Sherbrooke, 3000 Boulevard Université, Sherbrooke, Québec, Canada J1K OA5
Oleh.Fesiienko@cea.fr

Topic : Etching, lithography and nano-patterning

***Abstract* — One promising integration scheme for High electron mobility transistors (HEMTs) based on III-N material heterostructures such as AlGaN / GaN is to use a thin AlGaN barrier. However, in this integration, one technological challenge is the step dedicated to the plasma etching of the SiN layer that must be stopped on the very thin AlGaN layer without introducing damage. In this paper, we evaluate the impact of fluorocarbon plasma process typically used to etch SiN on AlGaN and AlN film integrated in HEMT device. We also propose to investigate alternative plasma technology such as pulsed plasma to limit the plasma induced damage.**

I. INTRODUCTION

High electron mobility transistors (HEMTs) based on III-N material heterostructures such as AlGaN / GaN are recognized as excellent candidates for future generation of components for power and high-frequency electronics thanks to their two-dimensional electron gas (2DEG) with high electron density ($\sim 10^{13}$ cm^{-2}) and high electron mobility ($\sim$ 1500 cm^2/V·s) [1, 2].

Typically, GaN HEMTs being in the on state, also called normally-on transistor. For reasons of safety, functioning and realizing logical functions, it is necessary to make HEMT normally-off (blocked when the gate voltage is zero).

Different approaches exist to make a normally-off HEMT such as: implantation of fluorides ions under the gate or recess, which involves locally etching the barrier at the gate or use thin barrier layer [3, 4, 5].

In this study we propose to develop the thin barrier layer strategy because it's more perspective and promising for GaN HEMTs technology.One technical challenge of this approach is the SiN plasma etching step that must be stopped on the thin AlGaN layer (cf. Fig.1).

This step must not only allow infinite selectivity over the AlGaN layer to preserve its thickness but must also preserve the integrity of the AlGaN material in terms of roughness, stoichiometry.

Fluorocarboned plasma is usually used to etch SiN. Other studies have shown that fluorine can diffuse through the

AlGaN layer down to the 2DEG channel leading to electrical channel properties degradation. [3, 6].
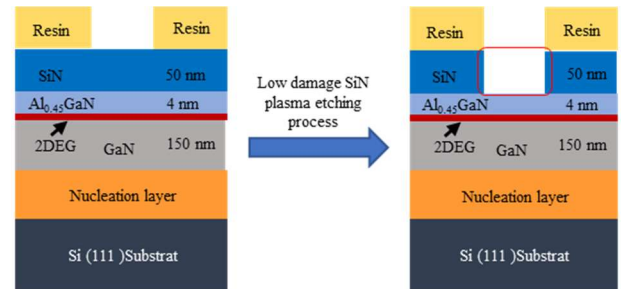

Figure 1. Scheme describing the critical step in GaN HEMTs fabrication process

The aim of this paper is to investigate the best plasma strategy to etch the SiN layer and stop on the AlGaN layer without causing damage. Preliminaries studies are dedicated to the impact of fluorocarboned plasmas on AlN and AlGaN layers and the evaluation of fluorine diffusion into those layers. Pulsed plasma technology using fluorocarboned plasma chemistries will also be investigated as it has already been proved that such technology can limit plasma induced damage. Alternative Fluorine free plasma chemistries will also be studied

II. EXPERIMENTS

The substrates used in this study are depicted in Figure 2. AlN and AlGaN layers are grown on 200 mm (111) silicon substrates using metalorganic vapor-phase epitaxy (MOVPE) while SiN is deposited by low-pressure chemical vapor deposition (LPCVD) E-beam lithography was used to print trenches with various width into a resist material.
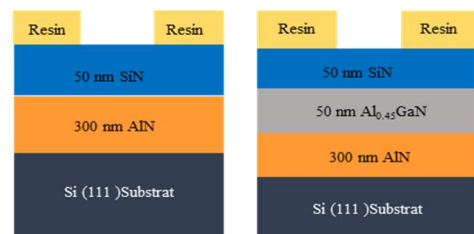

Figure 2. Description of the two substrates studied

All plasma etching processes have been performed in a 300 mm inductively coupled plasma (ICP) etching tool from Applied Materials. The inductive source power and the bias power are operated at 13.56 MHz. The samples are mounted with thermopaste on a 300 mm silicon carrier wafers. The

sciencesconf.org:jnte2019:291327

etch kinetics of the materials exposed to plasma are monitored by in situ kinetic ellipsometry.

The SiN is etched with two steps: a main etch using fluorocarboned plasma stopped dedicated to the anisotropic etching of the SiN followed by an overetch step dedicated to the etching of the last 10 nm of the SiN material with a soft landing on the AlN or AlGaN layer. This study focuses on the development of the overetch step.

The damage that the plasma exposure can cause on AlN and AlGaN layers are estimated by angle resolved X-ray photoelectron spectrometry (AR-XPS) and atomic force microscopy (AFM). The pattern profiles after SiN etching are characterized by After plasma exposure, the AlN and AlGaN surfaces are characterized by scanning electron microscopy (SEM).

III. RESULTS AND DISCUSSION

Fluorocarboned plasma processes impact on AlN layers have first been investigated. Two plasma chemistries have been compared CH_4/CF_4 or CHF_3/CF_4. For both processes, an infinite etch selectivity of SiN over AlN is obtained. However, XPS analyses reveal the formation of AlF_x salts on the AlN surface as revealed by the XPS Al2p spectrum. Moreover, thanks to the angular capability of the XPS analyses, the depth penetration of F into the AlN layer could be estimated as shown in Figure 3. It is observed that F penetrates up to 3-4 nm into the AlN and the penetration depth is slightly deeper if a CH_4/CF_4 plasma is used (4nm vs 3nm).
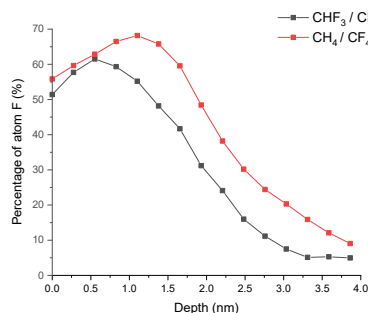

Figure 3. Fluorine distribution profiles obtained by ARXPS on the samples treated 20s by CHF_3 / CF_4 and CF_4 / CH_4 plasma

To limit this F penetration, we decrease the ion energy by decreasing the bias power in the CHF_3/CF_4 plasma process. Figure 4 shows the SEM profiles after patterning the SiN with the high and low bias power conditions. The SiN profiles are satisfying and both plasma conditions lead to smooth AlN surfaces.
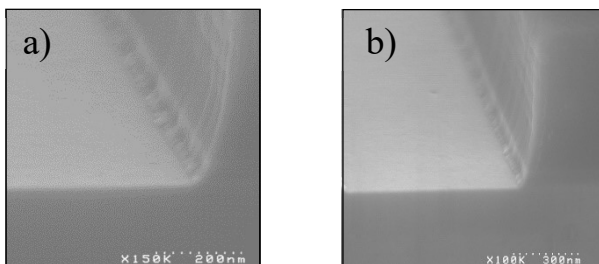

Figure 4. Cross-section SEM images of the samples profiles vias etched by CHF_3 OE plasma with a)20W power bias, b) 60 W power bias.

The ARXPS analyses highlight that the fluorine penetration into the AlN is shallower with reduced bias power, although if a 2.5 nm surface modification still remains unacceptable for the integration.
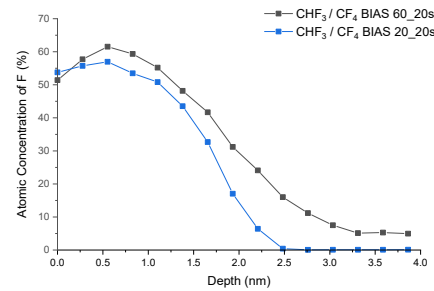

Figure 5. Fluorine distribution profiles obtained by ARXPS on the samples treated in different bias power conditions by CHF_3 plasma

Figure 5 shows the fluorine atom concentration profile for two different conditions plasma chemistry. As can be seen the penetration of the fluorine atoms into the surface depth of AlN depends on the time of exposure and the ion energy (bias power) that is bombarding the surface.

CONCLUSION

In this article, we have investigated using SEM and XPS characterization techniques the chemical modifications induced in AlN films exposed to fluorocarboned plasma process. Although an infinite SiN/AlN etch selectivity can be obtained with such plasma processes, an AlF_x layer is formed on the AlN surface. Tuning the plasma chemistry from CH_4/CF_4 to CHF_3/CF_4 slightly reduces the F penetration within the AlN layer. Lowering the bias power is also a parameter allowing a minimization of the surface fluorination. This suggests that pulsed plasma technology in which the mean ion energy is lowered compared to continuous wave plasma is a promising approach to limit the plasma damage. This approach is the next approach to be tested. Similar experiments are on going on the AlGaN material

REFERENCES

[1] Mishra, U. K., Parikh, P., & Wu, Y. F. (2002). AlGaN/GaN HEMTs-an overview of device operation and applications. Proceedings of the IEEE, 90(6), 1022-1031.

[2] Aubry, R., et al. "ICP-CVD SiN passivation for high-power RF InAlGaN/GaN/SiC HEMT." IEEE Electron Device Letters 37.5 (2016): 629-632.

[3] Cai, Yong, et al. "High-performance enhancement-mode AlGaN/GaN HEMTs using fluoride-based plasma treatment." IEEE Electron Device Letters 26.7 (2005): 435-437.

[4] Saito, Wataru, et al. "Recessed-gate structure approach toward normally off high-voltage AlGaN/GaN HEMT for power electronics applications." IEEE Transactions on electron devices 53.2 (2006): 356-362.

[5] Chang, C. Y., et al. "Development of enhancement mode AlN/GaN high electron mobility transistors." Applied Physics Letters 94.26 (2009): 263505.

[6] Dagher, Gulnar, et al. "Electrical behavior of GaN-HEMT after fluoride plasma treatment." physica status solidi c 8.7-8 (2011): 2416-2419.

Integrated chiral optics processing for sensing application

Alban GASSENQ[a], Hoshang SAHIB[a], Amina BENSALAH-LEDOUX[a], Leo COLLIARD[a], Gaetan CUSSAC[a], Bruno. BAGUENARD[a], Francois BESSUEILLE[b], Laure GUY[c] and Stéphan GUY[a]

(*a*) Institut Lumière Matière, UMR CNRS 5306, University of Lyon, France
(*b*) Institute of Analytical Sciences, UMR CNRS 5280, University of Lyon, France
(*c*) Laboratoire de Chimie, UMR CNRS 5182, Ecole Normale Supérieure de Lyon, France

Topic : Organic photonics, chiral integrated optics

Abstract—**In this work, we present our recent progress in micro-structuration and fabrication of new waveguides in organic modified silica (OrMoSil) layers. Such chiro-waveguides could propagate any kind of polarization which open a way to chiral integrated sensing which cannot be done with conventional waveguides.**

I. INTRODUCTION

Since the early observation of molecular chirality by Pasteur [1], its effect on living systems has attracted researcher's attention [2]. Indeed, detection of chiral molecules is highly important in the field of pharmacology and food industry [3]. The natural behaviour of chiral objects (including molecules) limits them to interact differently only with other chiral objects and that is the basis of materials optical activity. A detector (sensor) incorporated with a chiral tool is necessary to sense chiral molecules. Integrated optical sensors platform has shown their ability to detect low molecular levels [4]. However, because of their achiral materials they are linear birefringent devices (TE/TM eigenmodes) unable to sense chirality.

Waveguides made of chiral materials are called chiro-waveguides [5] and are elliptical birefringent devices [6] that allow chiral sensing [7]. Recently, we have shown that planar chiro-waveguides in a symmetric cladding structure can be used to tailor polarization of guided light from linear to nearly circular with OrMoSil layers [8,9]. OrMoSil layers are made of SiO_2 material associated to organic molecules. To realize an evanescent wave based chiral sensor, we need now to micro-structure our chiral layers, to combine the effect of the guiding layer structuration and its chirality on light polarization in order to fabricate integrated optical circuits with circularly polarized light propagation for chiral sensing applications.

II. PROCESSING

Figure 1 presents the different envisioned processing to fabricate micro-structured chiro-waveguides from OrMoSil layers. Three methods are studied: the direct layer etching (Figure 1-a), the photo-sensitive layer micro-structuration (Figure 1-b) and the micro-transfer method (Figure 2-c). Each method has different drawbacks and advantages; we thus have chosen to explore these different ways and to compare the obtained waveguides properties. Dry etching method (Figure 1-a) will be performed with a NGP80 reactive ion etching equipment after the UV contact mask lithography. Photosensitive method (Figure 1-b) will be performed with photosensitive OrMoSil layer [10,11] and µPG101 laser lithography machine to avoid sticking between UV mask and OrMoSil un-reticulated layer with conventional UV mask aligner. For the micro-transfert (Figure 1-c), PDMS mold will be fabricated with a Si master fabricated on Si with the same dry etching equipment. The stamping (or microtransfert) will be then done manually on Si substrate or on OrMoSil cladding layer on Si.
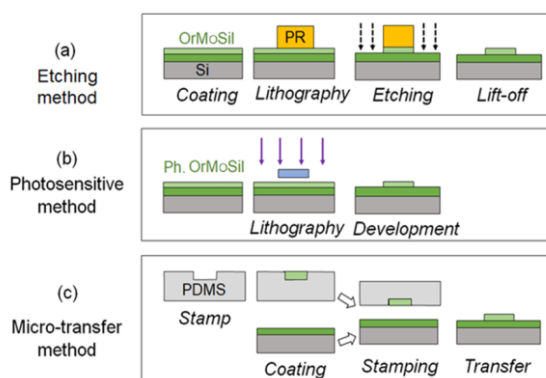

Figure 1. Stuided methods to fabricated chiro-optics waveguides by a) etching, b) photosentive and c) microtransfer methods

A. Etching method

Dry etching method for waveguide fabrication are mainly used in micro-electronics. Such method is not often use for organic photonics since organic layers can be sensitive to lift-off processing. In our case, we have studied the etching speed of OrMoSil layer and photosensitive photoresist to avoid lift-off step like presented in the Figure 2. If the layer speeds are well known, full etching of the AZ 5214 soft mask can be used to remove it.
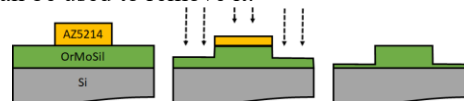

Figure 2. Used process flow for dry etching method without lift-off

For dry etching we have used SF_6 and O_2 gas at 100W power for different pressures. Figure 3 presents the etching speed as a function of the pressure and the used gas ratio. OrMoSil and AZ5214 photoresist layers were studied with Si and SiO_2 substrate as reference. We clearly see that the etching speed are in the same range between OrMoSil and photoresist layers except without SF_6 which is highly needed to etch the SiO_2 part of the OrMoSil layer. Therefore, the etching selectivity between OrMoSil and photoresist is close to one. Since we want to obtain around 1.5µm etched OrMoSil thickness we have use 1.5µm thick

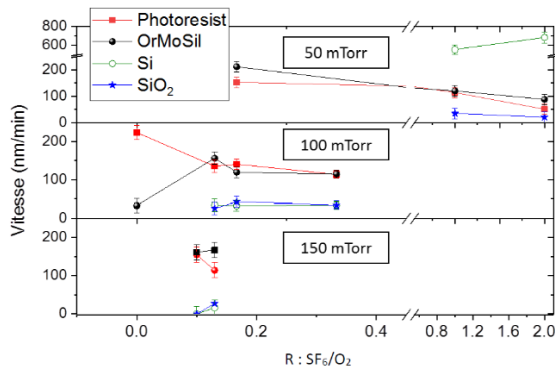photoresist to fully remove the photoresist layer during the OrMoSil etching.

Figure 3. Ecthing speed measurements for different materials as a function of the pressure and the gas ratio

For the pressure influence, the etching speed is not strongly affected. Figure 4 presents Scanning Electron Microcospy (SEM) tilted images at different pressure for 1/6 etching gas ratio. In that case, high pressure is needed to obtain smooth etching.
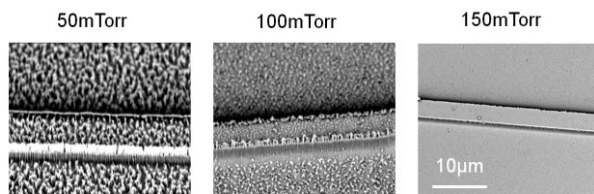

Figure 4. SEM imaging for diferent gas pressure at 1/6 ratio

B. Photosensitive method

Photosensitive OrMoSil have been already studied for making organic waveguide but without chiral molecules [10,11]. In this works we have studied the influence of the insolation dose on the fabricated waveguide. $2\mu m$ thickness layers with IR819/MAPTS/TEOS-7/1/2 proportion obtained by deep coating at 300mm/min speed and annealed 2h at 100°C were used. Layers were micro-insolated with laser lithography µPG101 equipment (with a $2\mu m^2$ 7mW spot) at a writing speed of ~10 mm²/min for n pass. The layers were developed 10s in THF solution. Figure 5 presents the profilo-meter measurements as a function of the number of pass which correspond to a maximum insolation dose of 1kJ/cm² for n=200. We clearly see that the thick waveguides are obtained only for the maximum insolation dose.
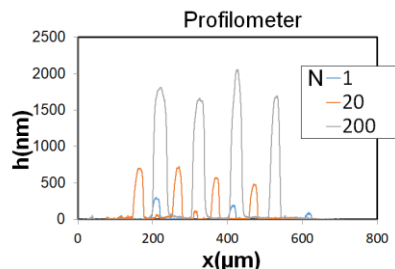

Figure 5. Profilometer measurement for photosensitive microstructuration as a function of the insolation dose N

C. Micro-transfert method

OrMoSil micro-structuration were also obtained on Si substrate by micro-transfer processing [12]. Si master was firstly fabricated by dry etching to make the PDMS mold. An OrMoSil liquid solution was then used to fill the PDMS mold and to realise the micro-transfer on Si after silanisation. OrMoSil layers were transferred on Si and on OrMoSil on Si. Microtranfert on Si was successfully demonstrated while layer peeling was observed for the transfer on OrMoSil cladding.

III. RESULT AND WORK IN PROGRESS

Figure 5 presents SEM images of fabricated waveguides by dry etching on SiO_2 (Figure 5-a), photosensitive insolation on Si (Figure 5-b) and Micro-transfer on Si (Figure 5-c). For dry etching such micro-structuration were obtained only on SiO_2 substrate since many layer cracks were observed on Si substrate probably due to the large difference of thermal expansion coefficient between Si and OrMoSil layer. Grating coupling is now envisioned at the beginning of the waveguide since SiO_2 substrate cannot be easily cleaved for direct coupling. For the photosensitive method, since the needed insolation is too high (~1kJ/cm²), layer composition influence and reticulation phenomena are now studied to improve photo-reticulation. Regarding micro-transfer, OrMoSil layer on Si can be obtained but not on OrMoSil cladding because OrMoSil cladding surface optimization is needed to avoid the layer peeling during the transfer.
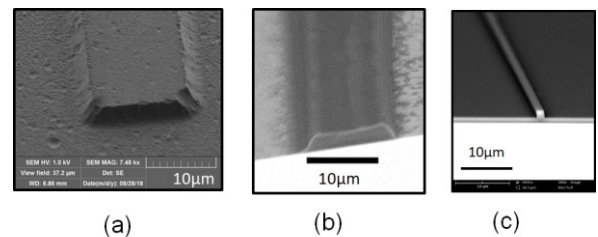

Figure 6. SEM image of microsturtured ,OrMoSil layers for a) dry etching, b) photosentitive and c) microtransfer methods.

REFERENCES

[1] Pasteur, L., Ann Chim 24, 442–458 (1848).
[2] Smith, S. W., Toxicol. Sci. Off. J. Soc. Toxicol. 110, 4–30 (2009).
[3] Ali, I. et al., Chirality 19, 453–463 (2007). Srkalova et al., Chem. Listy 102, 480–486 (2008).
[4] Mukundan, H. et al., Sensors 9, 5783–5809 (2009).
[5] Engheta, N. & Pelet, P., Opt. Lett. 14, 593–595 (1989).
[6] Herman, W. (NAVAL AIR WARFARE CENTER AIRCRAFT DIV PATUXENT RIVER MD, 1999).
[7] Guy, S. et al., Prog. Electromagn. Res. B 24, (2010).
[8] Hadiouche, D. et al., Opt. Mater. 36, 885–891 (2014).
[9] Guy, S. et al., ACS Photonics 4, 2916–2922 (2017).
[10] Amir Fardad et al. APPLIED OPTICS Vol. 37, No. 12 (1998)
[11] Sunho Jeong, et al. Thin Solid Films 466, 204 – 208 (2004)
[12] D. Li, et al., J. Opt. A Pure Appl. Opt. 11, (2009)

BURIED DEFECTS INVESTIGATION THROUGH BACKSCATTERED ELECTRON MICROSCOPY

Aurélie Le Pennec, Maxime Argoud, Guido Rademaker, Raluca Tiron

Univ. Grenoble Alpes, CEA, LETI, F-38000 Grenoble, France
e-mail of contact author : aurelie.lepennec@cea.fr

Topic: In-line metrology for microelectronic process control

Abstract — **Backscattered-electron microscopy (BSE) is used as a non-destructive and in-line characterization method to monitor processes and is based on material chemical contrast. Etching or deposition uniformity control can be achieved by using BSE. For example, it allowed us to detect a residual carbon layer after the mandrel etching in the SADP process.**

I. INTRODUCTION

As dimensions keep reducing in the microelectronic field, new characterization techniques need to be developed. Here, we introduce the implementation of backscattered electron microscopy (BSE) at CEA-LETI.

II. METHOD DESCRIPTION

A. Process description

The process implemented at CEA-LETI is the Self-Aligned Double Patterning (SADP) process [1]. It is used to reduce to 40 nm line / space patterns obtained via conventional lithography processes (immersion lithography for example). This process is described in figure 1.
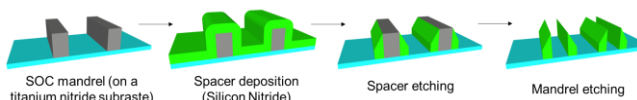

Figure 1 Schematic representation of the SADP process

After a lithography step in which pattern sizes are designed on a titanium nitride (TiN) substrate, these are transferred in an underlying carbon layer (SOC), known as the mandrel. Then, a silicon nitride layer (SiN) is deposited by plasma enhanced chemical vapor deposition at 320°C. This conformal layer is etched to form spacers and the mandrel is removed by etching as well.

B. Backscattered electron microscopy

When interacting with the sample surface, an incident electron can be subjected to elastic and inelastic scattering, which results in the escape of secondary and backscattered electrons. Whereas secondary electrons scan extreme surface and thus sample topography, backscattered electrons reflect the chemical composition of the sample in depth. The backscattered electron yield depends on specimen composition, density, and thickness [2]. The bigger the atomic number, the brighter the signal will be represented in the grey scale of the image resulting from the acquisition on the CD-SEM.

BSE is implemented on the VeritySEM (from Applied Materials) available at LETI. When applying a spectrometer offset, only backscattered electrons are gathered by electrons detector and a BSE image is obtained. Results obtained with this technique are correlated by Transmission Electron Microscopy (TEM) cross-sections.

III. OBJECTIVES AND RESULTS

The objective is to implement a fast, at wafer scale, and non-destructive method to characterize buried layers. Current available methods are mainly destructive like TEM cross-sections. Other characterization techniques could be considered (like Atomic Force Microscopes) but aspect ratios are too high and the tip doesn't reach the bottom of patterns. Moreover, no sample preparation is needed to implement this technique.

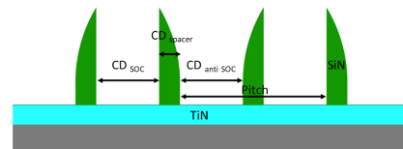Abbreviations used in the results section are described in figure 2.

Figure 2. Description of the abbreviation used in the results sections. (In green : spacers in SiN ; in blue : TiN substrate)

Figure 3 presents a SEM image compared to a BSE image. In the SEM image, only topography is observed whereas chemical contrast is present on the BSE image, on which two materials are present: the substrate made of titanium nitride (TiN) and spacers in silicon nitride (SiN).
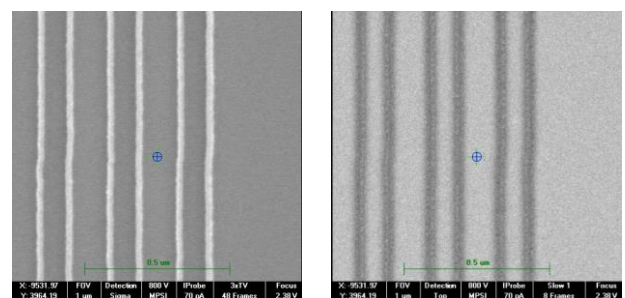

Figure 3. Juxtaposition of a classical SEM image (on the left) and a BSE image (on the right) with a tension filter of 700eV at the same position

We can assume that no other material is present since only two grey levels are represented on figure 4: TiN (points 1, 3 and 4) and SiN (2). The shape of the grey level signal is supposed to be equivalent whatever the pitch and CD $_{SOC}$ if there is no other material in presence.
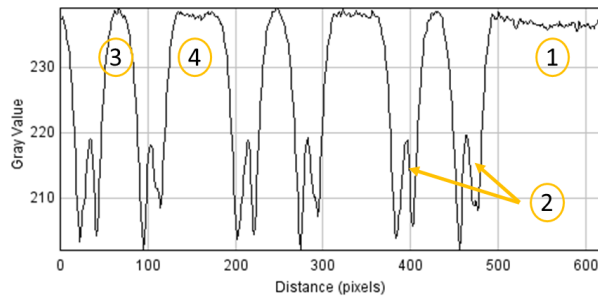

Figure 4. Grey level of the BSE image presented in Figure 3. (1: TiN signal taken as a reference; 2: SiN spacers signature, 3 and 4 : intra and extra spacer TiN signal)

When we characterize patterns with smaller pitches (as presented in figure 5), we can observed that a third grey level is represented. Depending on the configuration (small CD $_{SOC}$ or small CD $_{anti\ SOC}$), it means that a buried layer is in presence (carbon or SiN respectively). The suspected origin is microloading during the etching step. Indeed, the removal of the mandrel is done by detecting the end point detection on a wafer where different pitches are designed.
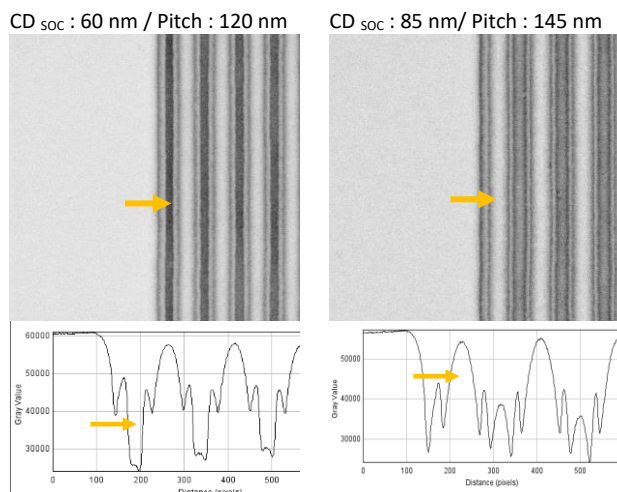
CD $_{SOC}$: 60 nm / Pitch : 120 nm   CD $_{SOC}$: 85 nm/ Pitch : 145 nm

Figure 5. BSE signal associated to their respectives grey level plots. Two different configurations are shown : small CD $_{SOC}$ with a residual carbon

layer (on the left) and small CD $_{anti\ SOC}$ with a residual SiN layer (on the right). The arrow points out where the carbon mandrel was before etching.

Carbon and silicon nitride residues where removed from the samples by using overetching, and the demonstration was done using BSE as well.

CONCLUSION

BSE has been demonstrated to be a powerful tool to control microelectronic processes, in a non-destructive, fast and in-line manner. This technique gives access to chemical information of nanostructures, and can be used to detect buried defects in the SADP process for example.

ACKNOWLEDGMENT

REFERENCES

[1] Paquet A., et al., "Spacer patterning lithography as a new process to induce block copolymer alignment by chemo-epitaxy", Proc. SPIE 10958-21, Advances in Patterning Materials and Processes (2019)

[2] Goldstein, J. I. et al. Scanning Electron Microscopy and X-Ray Microanalysis. (Springer, 2017).

FABRICATION OF HIGH ASPECT RATIO VERTICAL SIDEWALL TRENCHES USING 2 STEPS PARAMETER RAMPING BOSCH PROCESS

Eric Lebrasseur*, Taisei Kuriyama*, Kenji Hirakawa**, Masayuki Iwase**, Munehiro Ogasawara**, Takashi Yoda**, Yoshio Mita*

* Mita Laboratory, University of Tokyo, Tokyo, Japan

** Laboratory for Future Interdisciplinary Research of Science and Technology, Tokyo Institute of Technology, Tokyo, Japan

(*e-mail of contact author*): eric@if.t.u-tokyo.ac.jp

Topic: *Silicon, DRIE (Deep Reactive Ion Etching), High aspect ratio, Parameter ramping*

Abstract—**The Bosch process has been widely used to achieve Si micro-structures. However, when fabricating narrow high aspect ratio trenches, problems such as tapering and sidewall damage often occurs. In this paper, we present a two-steps parameter ramping method which is effective for solving such issues.**

I.   INTRODUCTION

DRIE (Deep Reactive Ion Etching) is a technique that enable the fabrication of deep trenches in silicon by alternating deposition and passivation steps. However, the higher the aspect ratio, the more difficult for the reactive ions to reach the bottom of the trench, which leads to issues such as tapered sidewalls. Technics to solve those issues and broaden the range of devices and applications, such as through silicon via (TSV), are still investigated nowadays [1]. In order to obtain high aspect ratio trenches with vertical walls, methods such as increasing the bias power or decreasing the pressure, which both enable more vertical trajectory of incident ions, can be used. However, the first one leads to lower mask selectivity and the second one leads to lower Si etching rate due to the reduction of reactive ions [2].

Parameter ramping method, which consist of changing the parameters continuously while the process is under progress, is another efficient way to solve those issues [3], [4]. This method allows to keep optimal parameters as the depth increases and the process conditions change. Thanks to this, side effects like decrease of mask selectivity and etching rate can be limited and high aspect ratio trenches with vertical sidewalls can be achieved.

In this paper, we present a method using a two-steps parameter ramping recipe, which enable to stay closer to the ideal etching conditions then the one-step parameter ramping recipe and leads to improved sidewalls quality during the deep etching of narrow trenches.

II.   EXPERIMENT

For the etching experiments, 525μm thick Si chips (about 1.5x1.5cm size) were used. Those chips were fixed on dummy 4-inch silicon wafers with silicone grease. The etching mask material was either a thick electron beam resist (OEBR-CAP112PM, thickness 1.5μm) or aluminum (thickness ~100nm). The deep reactive ion etching equipment was the MUC21-ASE Pegasus from SPTS. 2μm width and 80μm deep trenches were targeted.
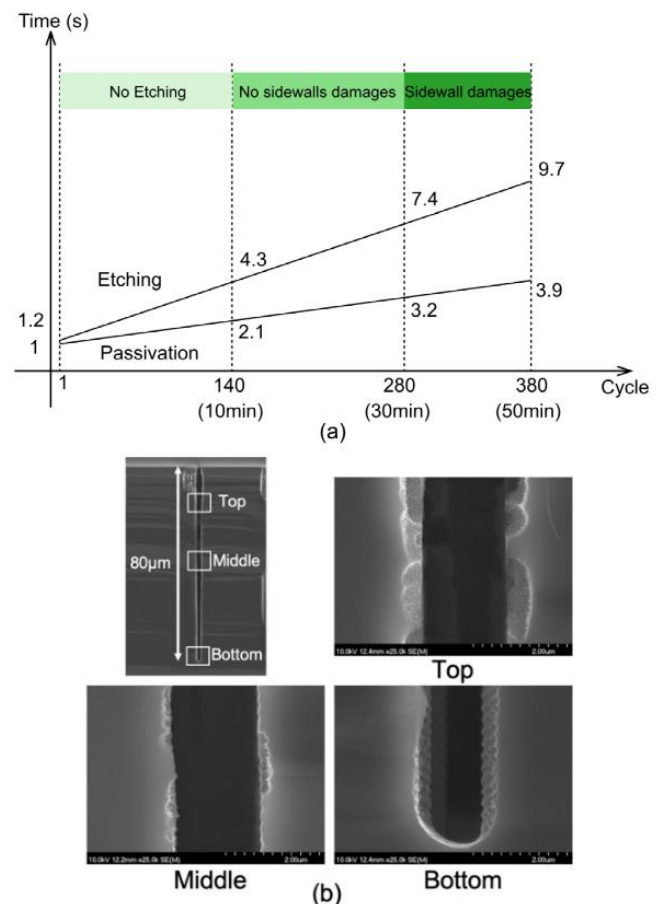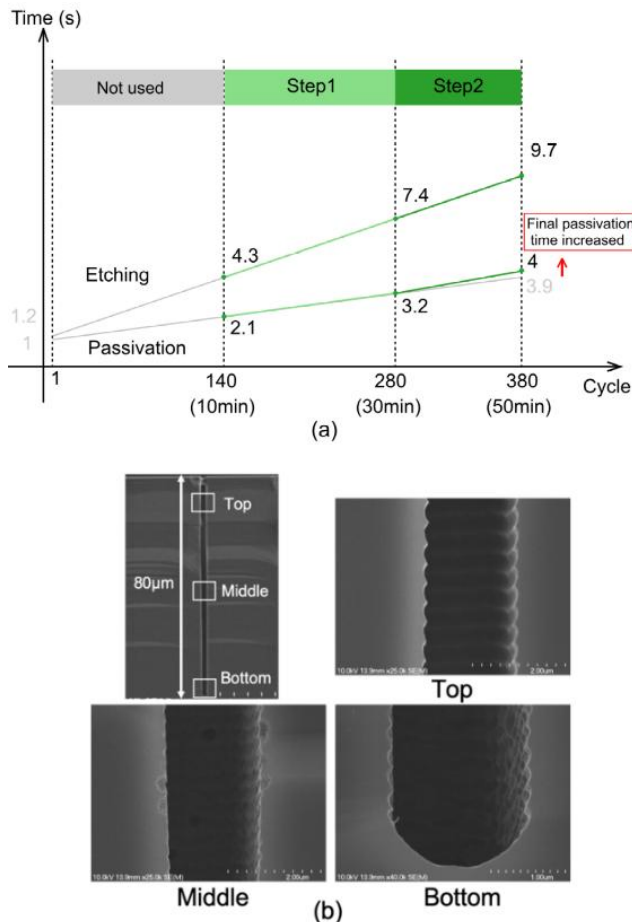

Figure 1.   (a) Parameter evolution during one-step ramping recipe. (b) SEM images of the fabricated trench with one-step ramping recipe. Damages were observed on some parts of the sidewalls.

At first, deep trenches were made using one-step parameter ramping recipe. In order to improve the access of the reactive ions to the bottom of the trench, the passivation step time and etching step time were both increased as the process time increased (Figure 1. a). As a result, 80μm deep trenches with a top width of 2μm and a bottom width of 1.98μm were obtained. However, some parts of the sidewalls were damaged in the process (Figure 1. b). Those damages may be due to the creation, by reflected reactive ions, of pin holes in the protection polymer layer, which leads to the Si etching of sidewalls during the isotropic etching phase [5], [5].

(a)

Figure 2. (a) Parameter evolution of two-step ramping recipe. (b) SEM images of the fabricated trench with two-step ramping recipe. The side-wall condition was drastically improved.

In order to determine when those damages start to occur, several samples were prepared and etched with different process time (10min, 20min, 30min). Then the samples were cleaved and observed with a scanning electron microscope (SEM). As a result, it was found that the etching was not progressing at all during the first 10min (140 cycles). The etching time was not long enough regarding the passivation time.

On the other hand, no sidewall damages were observed for a process time of 30min (280 cycles). Damages appeared for process time longer than 30min (Figure 1. a).

Based on those observations a new recipe was set up (Figure 2. using two ramping steps. As there were no sidewall damages during the first 30min of the first recipe, the same ramping conditions were used for the new recipe except that the first 140 cycles were removed as no etching occurred during this phase. Then the ramping conditions were changed so that the passivation time would increase faster relatively to the etching time. Actually, very small parameter changes can lead to dramatic changes in the process, so the final deposition time was increased only by 0.1s (from 3.9 to 4s).

With this new recipe, 80μm deep trenches with vertical sidewalls (top width of 2μm, bottom width of 1.95μm) and with much improved sidewalls quality were achieved (Figure 2. .

III. CONCLUSION

High aspect ratio trenches with vertical sidewalls were fabricated using parameter ramping Bosch process. The recipe was modified by adding a second parameter ramping step with faster passivation time increase, which enabled to drastically reduce the sidewalls damages while maintaining their verticality. We can expect to increase furthermore the aspect ratio and the sidewalls quality by increasing the number of ramping steps and/or adjusting the ramping parameters.

REFERENCES

[1] B. Chang, P. Leussink, F. Jensen, J. Hübner and H.Jansen: "DREM: Infinite etch selectivity and optimized scallopsize distribution with conventional photoresists in an adaptedmultiplexed Bosch DRIE process", Microelectronic Engineering,Vol. 191, pp. 77-83 (2018).

[2] H. Tanaka and H. Kanao, "Trend in etching of silicon for MEMS fabrication," Journal of The Surface Finishing Society of Japan, Vol. 68, No. 7, pp. 379–386 (2017).

[3] K. J. Owen, B. VanDerElzen, R. L. Peterson and K. Najafi, "High aspect ratio deep silicon etching," MEMS, pp. 251-254 (2012).

[4] Y. Tang, A. Sandoughsaz, K. J. Owen and K. Najafi, "Ultra Deep Reactive Ion Etching of High Aspect-Ratio and Thick Silicon Using a Ramped-Parameter Process," Journal of Microelectromechanical Systems, Vol. 27, No. 4, pp. 686-697 (2018).

[5] J.W. Choi, W.L. Loh, S.K. Praveen, R. Murphy, E.T.K. Swee: "A study of the mechanisms causing surface defects on sidewalls during Si etching for TSV (through Si via)", Journal of Micromechanics and Microengineering, Vol. 23, No. 6, pp. 065005 (2013).

[6] L. Meng and J. Yan: "Effect of process parameters on sidewall damage in deep silicon etch", Journal of Micromechanics and Microengineering, Vol. 25, No. 3, pp. 035024 (2015)

CYCLING OF IMPLANTATION STEP AND REMOTE PLASMA PROCESS STEP FOR NITRIDE SPACER ETCHING APPLICATIONS.

Nicolas Loubet[a,b], Camille Petit-Etienne[b], Cécile Jenny[a], and Erwine Pargon[b]

[a]STMicroelectronics, 850 rue Jean Monnet, 38926 Crolles Cedex, France
[b]CNRS-LTM, UMR 5129, Université Grenoble Alpes, CEA-Leti Minatec 17 rue des Martyrs, F-38054 Grenoble Cedex, France
nicolas.loubet@st.com

Topic: Etching, lithography, and nano-patterning.

Abstract—**The etching of silicon nitride spacers is a key step in the fabrication of transistor. The smart-etch concept brings a high selectivity while being anisotropic. A new route is proposed to implement this concept by cycling the process in the same plasma reactor.**

I. INTRODUCTION

Spacers are essential components of the transistor to control the source and drains and ensure good transistors performances. The etching can be very challenging as it requires both a high selectivity towards the underlying Si and a good anisotropy to obtain the spacer shape. Spacers are usually made of silicon nitride (SiN) deposited by low pressure chemical vapor deposition (LPCVD) and can thus be etched by conventional fluorocarbon based plasmas in inductively coupled plasma (ICP) reactors. However, current technologies show some limitations to etch stack of material without damaging underlayers. The smart-etch concept proposed in previous studies [1] brings interesting pathways to solve this issue. It relies on a two-step process: a light ion plasma implantation step (typically H_2 or He are used) to modify the material surface over a well-controlled thickness driven by the ion energy, followed by a removal step, using either HF exposure or a remote plasma discharge, that is dedicated to the removal of the modified layer with high selectivity over the non-modified layer. The energy of implantation is controlled by the bias power and the high directionality of the ions ensures anisotropy as only the horizontal surfaces are implanted. The removal step must be highly selective between the modified and non-modified material in order to keep the vertical surfaces (sidewalls) undamaged. So far, two different equipment were needed to perform the implantation and the removal steps which implied an air exposure between steps. The use of the same plasma reactor to conduct both steps is allowing new implementation of the smart-etch concept by cycling the two steps to get a fine control of the etched thickness.

II. EXPERIMENTAL

A. Substrates

A 75nm-thick SiN film deposited by plasma enhanced chemical vapor deposition (PECVD) on bare silicon is used. This silicon nitride is richer in hydrogen than the already extensively studied LPCVD deposited films.

B. Plasma reactor

The plasma reactor used for this study is a 300mm prototype chamber. It has both a remote plasma source (RPS) and a capacitively coupled plasma (CCP). The CCP unit is alimented by a RF power supply (13,56MHz) coupled to the bottom electrode which is equipped with an electrostatic chuck kept at 100°C. The walls are maintained at 80°C while the lid separating both units is at 130°C. The first step, the ion implantation, is realized by a CCP discharge, flowing H_2 at a pressure of 50mTorr for 60s. The ion energy obtained for such conditions is about 120eV. The RPS unit is alimented by a RF power supply (13,56MHz) separated from the CCP unit by the lid which is composed of several showerheads. Those showerheads block the ions so that only the radicals go through and reach the substrate. A gas mixture of He/NH_3/NF_3 at 2,5Torr is used during the remote plasma step to perform the selective removal of the modified layer. Previous studies have shown that when SiN or SiO_2 are exposed to a NH_3/NF_3 remote plasma the etching proceeds through the formation of ammonium hexafluorosilicate $(NH_4)_2SiF_6$ salts [2][3]. With a chuck temperature of 100°C, those salts are outgassed at the end of the process when the chamber pressure decreases down to the base chamber pressure of a few mT.

C. Charaterizations techniques

X-ray reflectometry is used to measure the thickness of the layer modified by the implantation: fitting the data to a model allows the extraction of the thickness, density and roughness of a stack of layers. Quasi in-situ Angle Resolved X-ray Photoelectron Spectroscopy (AR-XPS) is conducted to study the chemical bonds present in the first 10nm of the SiN film after implantation. The AR-XPS system is directly connected to the plasma chamber by a vacuum transfer chamber thus avoiding air exposure between the process and the measurement. It is equipped with a high-resolution monochromatic AlKa x-ray source. To construct the composition depth profile, the spectra are acquired at eight angles between 23,75° and 76,25°. The etch kinetics of implanted and pristine SiN are monitored with an ellipsometer directly connected to the chamber. The etch rate and the salt thickness during the process can be obtained from fitting the data to a model comprising the SiN film and a layer of salt on top of it.

A. Characterization of implanted SiN

The XPS analysis of pristine SiN reveals the presence the Si-N and Si-O bonds respectively at 101,6eV and 103,3eV [4]. The presence of an oxidized surface is confirmed by the XRR analysis as the results are fitted by a two-layer model as shown in figure 1a). On implanted SiN, two layers on top of the bulk are observed after the XRR analysis, and the AR-XPS shows an important concentration of fluorine and oxygen in the first 3nm of the implanted SiN, due to the presence of fluorine in the reactor. The profile can thus be constructed as a trilayer model shown in figure 1b): the implanted SiN is composed of an oxygen and fluor-rich top layer and a layer closer in density to the bulk, assumed to be the modified SiN rich in hydrogen. The implantation creates layers of lower density and richer in oxygen and fluorine than the bulk. Those layers are promoting the etching during the remote plasma step.
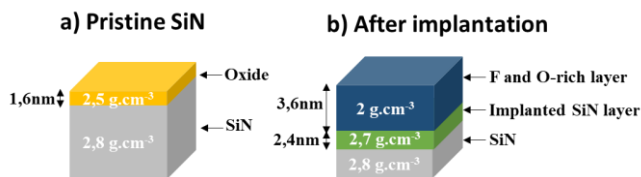
Figure 1. Schematic of the layers before a) and after b) implantation.

B. Kinetics of implanted vs non implanted SiN

For pristine SiN a 20s delay is observed before the etching starts when exposed to the $He/NH_3/NF_3$ remote plasma, as shown in figure 2. This incubation time most likely corresponds to the time needed for the reactive species to absorb on the surface and react with the SiN to form a salt. As shown previously the pristine SiN has an oxidized layer, if it's removed via a deoxidation with HF1% the remote plasma doesn't etch the surface. This suggests that the oxidized layer plays a key role in the absorption of species on the surface.
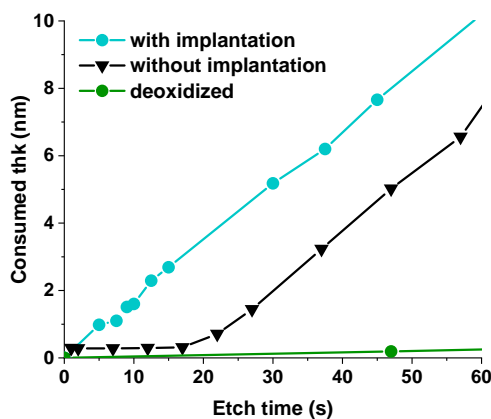

Figure 1. Etching Kinetics of SiN films after implantation (blue), without implantation (black) and after a deoxidation (green).

After implantation the etch starts without any incubation time implying that the change in the surface state catalyzes the formation of salts. The modifications induced by the implantation changes the incubation time offering a process window with infinite etch selectivity between horizontal (implanted) and vertical (non-implanted) surfaces.
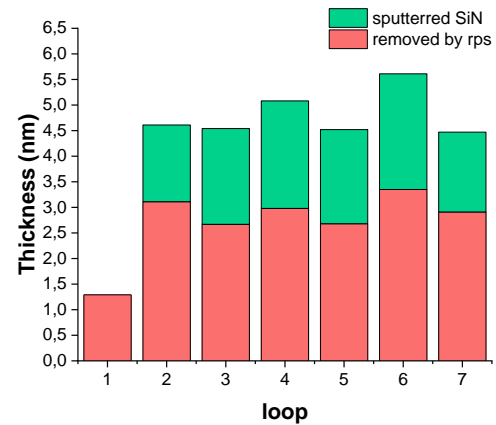

Figure 3. Etched thickness due to sputtering during the implantation (green) and during the RPS (red) for each loop.

When cycling the 60s implantation step with a 15s RPS, each cycle removes about 4,5nm except the first one as shown in figure 3. This implies that the native oxide reacts differently to the implantation than the bulk of the SiN film. Moreover, the first implantation leaves the film undamaged whereas the following implantations sputter around 1nm of material. AR-XPS analysis at different points during the process will be exploited to understand those differences.

The cycling will be applied on patterns to gauge the efficiency of this process compared to conventional etching processes. A particular attention will be given to the selectivity towards the underlying silicon and the shape of the spacer.

REFERENCES

[1] 1: N. Possemé, O.Pollet & S. Barnola, Applied Physics Letters 105, 051605 (2014).

[2] H. Ogawa, T. Arai, M. Yanagisawa, T. Ichiki, and Y. Horiike, Jpn. J. Appl. Phys., 41, p. 5349 (2002).

[3] A. Tavernier, L. Favennec, T. Chevolleau, V. Jousseaume, ECS Transactions, 45 (3) 225-232 (2012).

[4] B.S. Sahu, A.Kapoor, P.Srivastava, O.P. Agnihotri and S.M Shivaprasad, Semiconductor Science and Technology, Volume 18, Number 7, (2003)

NANOENGINEERING DNA NANOSTRUCTURES FOR LITHOGRAPHY

Marie Marmiesse[1], Raluca Tiron[1], Guillaume Thomas[1], Xavier Baillin[1]
[1]Univ. Grenoble Alpes, CEA, LETI, DPFT, Lithography Laboratory, F-38000 Grenoble
e-mail of contact author : marie.marmiesse@cea.fr

Topic : Nanopatterning

Abstract— **DNA origamis provide great potential to create nanostructures with sub-10 nm feature sizes. This ability makes them excellent candidates for a use as lithographic mask. Here, we show a method a method for nanopatterning a silicon substrate using DNA origamis as mask.**

I. INTRODUCTION

The semi-conductor industry is facing new challenges in lithographic technologies in order to reduce the size and to increase the density of components. In this context, DNA origamis have shown great potential to face these challenges.

II. DESCRIPTION

Patterning surface with structural DNA origami mask presents a major interest for nanolithography due to its modularity and high ability to achieve a high resolution with 3-5 nm (figure 1 a and b). In a previous work, we almost demonstrated a pattern transfer into a SiO_2 layer [1]. In this paper, we demonstrate a sub-ten-nanometer lithography process using anhydrous HF vapor into a SiO_2 substrate (figure 1C).

III. PROCESS

With strategically rinsing conditions on SiO_2 substrate and HF etching process, we reach a high density (>20 nm pitch) and high resolution (~10 nm CD) patterned surface with a fast etching rate of 0.2 nm.s^{-1}. Original structure, morphology and dimensions of DNA origami are fully conserved with high fidelity after HF etching. The resulting SiO_2 patterns are used as a hard mask and are transferred by using a HBr/O_2 plasma into a Si substrate (figure 1C). We conserve features of the hard mask: lateral dimensions, morphology and structure. In this paper, we developed a high resolution (~10 nm) and high contrast (~40 nm) transfer of patterns into Si substrate.

Moreover, templated substrates are generated by a nanoimprint lithography with gratings such as line and space patterns or contact holes. These are used in order to control DNA pattern precise placement on the substrate.

Thus, DNA origami appears like a promising approach for emerging and engineering of hard mask for patterning.
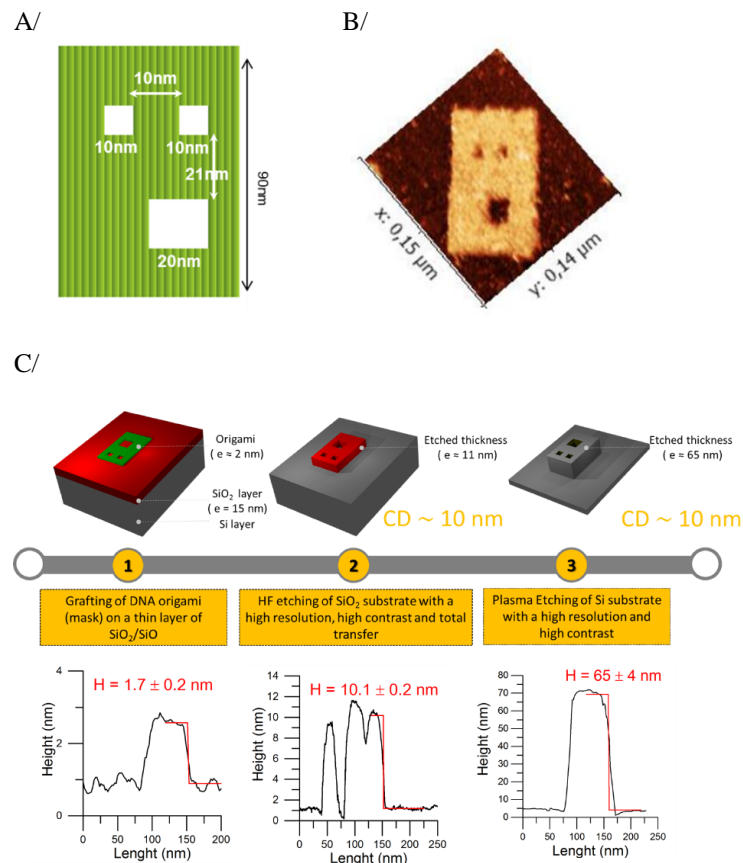

Figure 1/ A/DNA origami design, B/ AFM image after origami adsorption on Si substrate, C/ Patterning process flow and associated AFM profiles of the patterns after 1/ pattern adsorption on the substrate 2/ pattern transfer into SiO2 and 3/ pattern transfer into Si

REFERENCES

[1] Diagne, C. T.; Brun, C.; Gasparutto, D.; Baillin, X.; Tiron, R. DNA Origami Mask for Sub-Ten-Nanometer Lithography. ACS Nano 2016, 10, 6458–6463.

Localized oxide MBE growth on Si by selective etching lift-off for on-chip thermoelectricity

R. Moalla[1], D. Han[1], G. Saint-Girons[1], J.-L. Leclercq[1], and R. Bachelet[1]

[1] *Institut des Nanotechnologies de Lyon (INL) - CNRS UMR 5270, Ecole Centrale de Lyon, Bâtiment F7, 36 av. Guy de Collongue, 69134 Ecully Cedex, France*

Topic : Synthesis, integration on Si and assembly of new heterogeneous materials, Selective etching, lithography and nano-patterning, Integration and applications of micronanotechnologies

Abstract—We report here challenging technological issues of the fabrication of micro-thermoelectric module based on epitaxial perovskite oxides on Si. A process using sacrificial layer lift-off followed by its selective under-etching is developed for a localized growth of sequentially *n* and *p* thermoelectric oxides leg pairs.

I. INTRODUCTION

Due to waste heat in compact microelectronic devices, thermal management has become crucial for either efficiently cooling it or self-powering it through harvesting. Indeed, thermoelectric (TE) materials can be used either for cooling by Peltier effect or for electric generation by Seebeck effect. For such applications, they are generally integrated in a complex TE module structured in 3D: electrically connected *p* - *n* TE leg pairs in a series, and in parallel with respect to the thermal flux [1], [2]. The fabrication of such module is challenging, and even more when integrated at the microscale. In addition, the main TE materials working around the room temperature based on tellurides (*e.g.* Bi_2Te_3, Sb_2Te_3) are toxic, scarce and chemically unstable. Alternative TE materials overcoming these issues are thus targeted in the next future, and functional oxides are appealing in this view [3], [4].

II. EXPERIMENTS AND RESULTS

Here, we focus on the fabrication of micro-thermoelectric module based on thin epitaxial perovskite oxides on Si in a planar geometry as described on Figure 1. All the required challenging technological steps will be detailed in the first part of this communication. Firstly, *n* and *p* type TE oxides (La-doped $SrTiO_3$ and Sr-doped $LaCrO_3$, respectively) should be separately and sequentially integrated by molecular beam epitaxy (MBE) on a $SrTiO_3$ buffered silicon wafer [5]–[8].
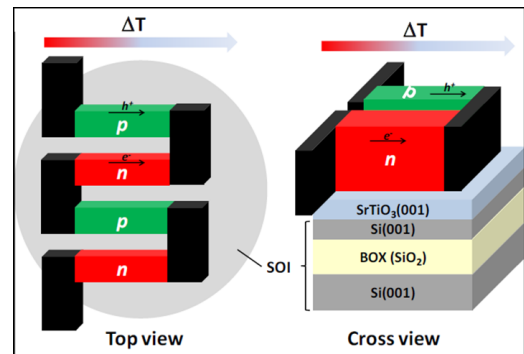

Figure 1. Sketch of a planar TE module architecture in top view and cross view.

For this, we are developing a specific lift-off technique combining sacrificial layer and hard mask patterning for localized MBE growth as shown on Figure 2. Then, this sacrificial layer have to be under-etched selectively regard to both TE oxides and $SrTiO_3$ buffered layer. Crucial issue is to properly remove it after MBE growth done at relatively high temperature (>500°C). For this, we have tested different classical bilayer combinations based on metal and/or dielectric materials such as Ni, Ta, SiO_2, Si_3N_4 and a-Si.
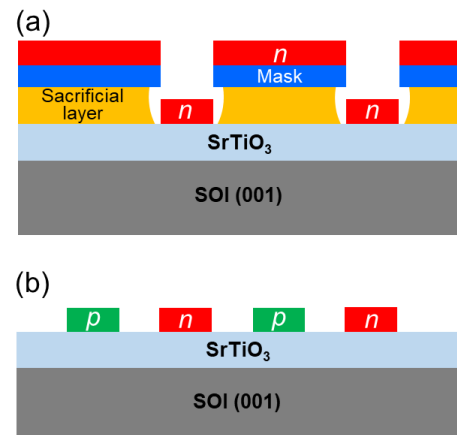

Figure 2. Sketch showing (a) the use of sacrificial layer lift-off for localised epitaxy growth of a *n* doped layer and (b) the final required structure

They present either good etching selectivity related to the grown oxides, or enough thermal stability, but not both at the same time.

Recently, we have obtained encouraging results by adapting a 'softly etched' epitaxial material, allowing the potential localized TE oxide growth. We are developing an experimental approach for the fabrication of a micro TE module on Si by controlling compatibilities between epitaxial material composition (oxides), mask design and etching process.

REFERENCES

[1] F. J. Disalvo, "Thermoelectric Cooling and Power Generation," Science, vol. 285, pp. 703–706, 1999.

[2] G. J. Snyder and E. S. Toberer, "Complex thermoelectric materials," Nat. Mater., vol. 7, pp. 105–114, 2008.

[3] J. He, Y. Liu, and R. Funahashi, "Oxide thermoelectrics : The challenges , progress , and outlook," J. Mater. Res., vol. 26, no. 15, 2011.

[4] T. Okuda, K. Nakanishi, S. Miyasaka, and Y. Tokura, "Large thermoelectric response of metallic perovskites : Sr 1-x La x TiO3 (0<x<0.1)," Phys. Rev. B, vol. 63, p. 113104, 2001.

[5] G. Saint-Girons et al., "Epitaxy of SrTiO3 on Silicon: The Knitting Machine Strategy," Chem. Mater., vol. 28, no. 15, pp. 5347–5355, 2016.

[6] M. Apreutesei et al., "Thermoelectric La-doped SrTiO3 epitaxial layers with single-crystal quality: from nano to micrometers," Sci. Technol. Adv. Mater., vol. 18, no. 1, pp. 430–435, 2017.

[7] K. H. L. Zhang et al., "Perovskite Sr-Doped LaCrO 3 as a New p-Type Transparent Conducting Oxide," Adv. Mater., vol. 27, pp. 5191–5195, 2015.

[8] D. Han et al., "Poisson ratio and bulk lattice constant of (Sr0.25La0.75)CrO3 from strained epitaxial thin films," J. Appl. Phys., vol. 126, p. 085304, 2019.

Realisation and characterization of large silicon cavities for interferometric applications

Marie Panabière[1], Camille Petit-Etienne[1], Silvère Gousset[2], Hélène Ehrhardt[2] and Jumana Boussey[1]

[1]. Univ. Grenoble Alpes, CNRS, CEA/Leti Minatec, LTM, 38000 Grenoble, France

[2]. Univ. Grenoble Alpes, IPAG, 38100 Grenoble, France

Abstract— **In this work, we describe the challenges related to the fabrication of large and ultra-deep silicon cavities as needed for the proof of concept of Nanocarb imaging spectrometer developed by the European Project SCARBO.**

INTRODUCTION AND CONTEX

The Horizon 2020 project Space CARBon Observatory (SCARBO) aims at the design and feasibility assessment of compact and low-cost satellites dedicated to the greenhouse gas (GHG) global survey. The concept adopted for the GHG concertation measurement is based on the use of a static Fourier-Transform imaging spectrometer proposed by IPAG and Onera teams [1]. Recent publications of those inventors have dealt in details with the design and performance modelling of this instrument for the detection of CO_2 and CH_4 gases [2, 3]. The predicted performances are very encouraging in terms of spatial resolution and sensitivity. One of the main objectives of the current SCARBO project is to elaborate a proof of concept of this instrument for on-board plane missions. This work is a contribution to this first prototype fabrication. This considered imaging spectrometer includes an interferometric core formed by the combination of a matrix of Fabry-Perrot (FP) interferometers with a micro-lens array (see Figure 1). Both have to be chosen and aligned in a way that each FP plate is associated with a micro-lens. An IR detector is placed on the focal plane of the micro-lens arrays, thus to obtain many images of a ground scene, each one being modulated by the corresponding FP interferometer.
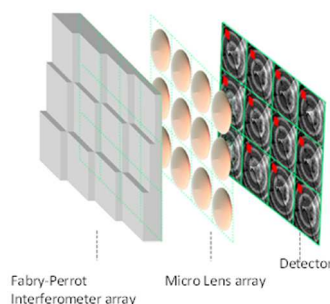

Figure 1. Scheme of the interferometric core of the Imaging spectrometer showing its three components.

It was decided to realize the FB array in silicon material to take advantage of its intrinsic good optical properties in the IR domain. In the present work, we describe the generic fabrication process we have developed and discuss its performance with respect to the required criteria.

GENERIC FABRICATION PROCESS

A. Starting material

The starting substrates are double side polished 100-mm diameter silicon wafers. The initial thickness of the substrate is chosen to be equal to 790 µm in order to optimize the sensitivity of CO_2 detection. None intentionally doped material was privileged to minimize IR light scattering with incorporated dopants. A specific lot of wafers satisfying the above mentioned characteristics was ordered from silicon vendor. The surface roughness of the received wafers was checked to be lower than 1nm (rms).

From the preliminary modelling work, it comes out that in order to precisely monitor CO_2, CH_4 gas in the atmosphere, a matrix of silicon plates has to be built on the silicon wafers by crossing two staircases. Lateral dimension (step width) of each staircase is dictated by the micro lens diameter and the detector pixel size while the height of each step is calculated as a function of the desired local OPD (optical path difference) for the investigated GHG spectral region. For this first prototyping attempt, step width was taken equal to or higher than 960µm while the step height has to match one of the following values: 46 nm, 230 nm, 3300 nm, 10 or 470 µm.

The generic fabrication process is rather simple. It consists in building the staircases by a series of optical lithography/ plasma dry etching sequences. Each sequence is characterized by its own lithography patterns and etching pattern transfer into silicon to the desired depth. Intermediate surface cleaning protocol was systematically applied in order to ensure a good surface quality of the final silicon plate.

B. Lithography step

Along this preliminary work, the staircase dimensions were frequently changed therefore a flexible and cost-effective mask-less lithography process was adopted. A table top Heidelberg µPG 101 tool based on a direct writing of patterns in photoresist films was used. Thin

(AZ1512HS) and thick (AZ4562) positive-tone photo resist films were used. The line edge roughness as well as the alignment accuracy between the two staircases were found to be conformal to the requirements.

C. Silicon etch step

Dry plasma etching processes were adopted to etch anisotropically shallow, deep and very deep cavities. For simplicity seek, all were developed with photoresist masking material. Shallow cavities were etched with a Cl_2-HBr-O_2/He inductively coupled plasma (ICP) etching process. The used reactor is equipped with in-situ optical characterization tools that allow a very accurate determination of the silicon etch rates. Moreover, the remaining photoresist films can be stripped with an oxygen plasma in the same reactor. The performance of this recipe in terms of uniformity, reproducibility and surface roughness were found to be within the required criteria (see Figure 2).
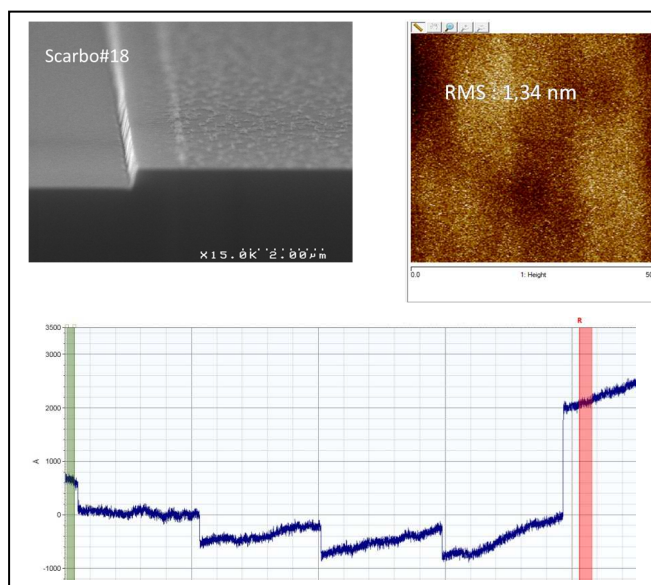
Figure2 : Typical results of shallow silicon steps obtaiend by chlorine based ICP plasma etching recipe. Top left, SEM image illustrating a 460nm hight edge ; top right, an AFM scan of the etched surface confirming a low rms surface roughness and, bottom : a profilometer scan of 4 consecutive steps of 46 nm height and 1920 µm width each

More issues are faced when deep (few tens of microns) or ultra-deep (~ 400 µm) cavities have to be etched. To achieve this depth range values, the silicon etching process was conducted in a Deep Reactive Ion Etching (DRIE) system using a Bosch process. In a Bosch process, the cavity is progressively obtained by applying many elementary cycles, each comprising two periods: the etching period with a SF_6 chemistry and the passivation period where a C_4F_8 gas is used to generate polymer materials on the sidewall and bottom. This polymeric passivation thin layer will prevent chemical reaction between SF_6 gas during the etching period. Consequently, the sidewalls may exhibit excessive wall roughness (usually called scalloping) which spatial periodicity is directly linked to the Bosch process parameters. On Figure3-a, typical SEM image of a cavity sidewall obtained during this study is illustrated. Another major issue of this deep reactive ion etching approach is the presence of "silicon grass" at the bottom of the cavities. These micro wires (see Figure3-b&c) are undesirable features etched into the silicon because of residual micro maskings which may be not fully removed during the etching cycles. These two issues can be detrimental for the interferometric concept being exploited for the Nanocarb sensor operation and have to be reduced.
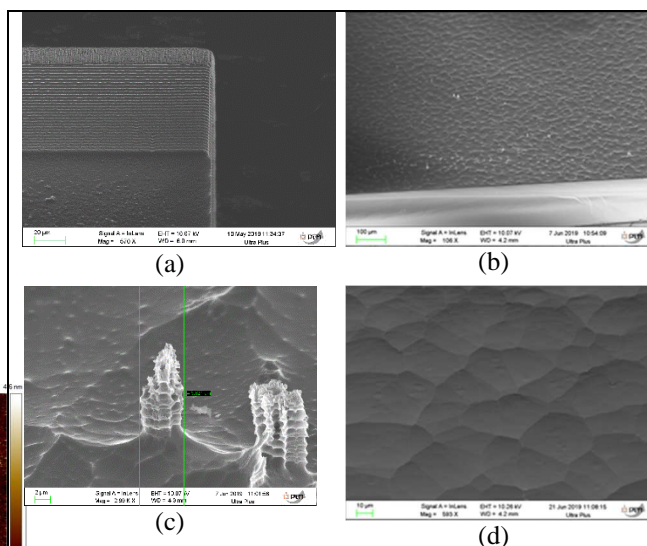

Figure3 : Typical results of ultra deep silicon cavities obtained by the Bosch process etching: a) SEM image showing the scalloping phenomenon, b &c) SEM images showing typical grass silicon at the bottom and d) the same cavity bottom after grass removal treatment

On-going work is dedicated to the optimization of a post-processing treatment based on the application of an isotropic etching of the silicon needles using a pure reactive SF_6 dry plasma etching. The first results obtained are promising as it can be seen on Fig.3-d where the bottom of a 400 µm deep silicon cavity was subjected to 126 s of a pure SF_6 reactive plasma treatment. Specific efforts are dedicated to the characterization of the cavity bottom surface quality as well as to its depth uniformity and reproducibility. Classical characterization tools as height profilometer or scanning electron & atomic force microscopies are not sufficiently powerful to access those parameters. That is why a thorough, nondestructive characterization of ultra-deep silicon cavities is being carried-on using an interferential metrology technique similarly to what has been performed for the characterization of the shallow cavity etching process [4].

At the conference venue, a detailed presentation of this fabrication procedure, including the silicon grass removal, will be available.

REFERENCES

[1] N. Guerineau et al. patent n° **WO2018/002558A1**

[2] S. Gousset et al., , SPIE **10562**, 105624U (2016)

[3] S . Gousset et al., CEAS Space Journal, **doi 10.1007** (2019)

[4] H. Erhhardt et al., ICSO 2018, Int. Soc. Opt. Photonics, **11180**, 1118066 (2018).

Dry etching challenges for high-χ block copolymers

G. Pound-Lana[a], P. Bézard[a], C. Gomes-Correia[c], X. Chevalier[b], C. Navarro[b], C. Nicolet[b], G. Fleury[c], M. Zelsmann[a]

[a] Univ. Grenoble Alpes, CNRS, LTM, Mintaec campus, 17 rue des martyrs, 38000 Grenoble, France
[b] ARKEMA, Groupement de recherches de Lacq, 64170 Lacq, France
[c] LCPO, CNRS–ENSCPB–Université de Bordeaux, 33607 Pessac, France
e-mail of contact author: marc.zelsmann@cea.fr

Topic : Directed Self-Assembly, plasma etching

Abstract— **In this work, we present our recent achievements on the integration and transfer etching of a novel silicon-containing high-χ block copolymer for lines/spaces applications. Dedicated neutral layers and top-coats allowing perpendicular orientations, it was possible to investigate specific plasma etching processes on full-sheets at 7 nm resolution, opening the way to the integration of these polymers in chemo-epitaxy stacks.**

I. INTRODUCTION

Block copolymer (BCP) of highly incompatible blocks (so-called high-χ BCPs) are attractive as a complementary next generation lithography technique since they can create self-assembled periodic patterns with features sizes below 10 nm. However, this high incompatibility is not without drawbacks such as long thermal annealing or preferential wetting at interfaces of one of the blocks. Then, forming perpendicular lamellar morphologies, which is the most promising approach for nano-patterning in terms of critical dimension control and resist budget, becomes a difficult task. At the substrate interface, such orientation is usually obtained with a grafted random copolymer with the same chemistry as the BCP but at the top interface complicated top-coat approaches have to be pursued since the solvent used for the top-coat should not modify the BCP layer. These developments are of particular interest for the so-called "chemo-epitaxy" directed self-assembly (DSA) approach, were high resolution chemical pre-patterns are used to ensure large scale registration of the formed micro-domains.

II. MATERIALS

In the present study, we report on the use of a new type of high-χ BCP: Poly(styrene)-*block*-Poly(1,1-dimethyl silacyclobutane) (PS-*b*-PDMSB, Fig. 1). This polymer showed lamellar periodicities down to at least 14 nm and its Flory-Huggins parameter χ was evaluated in the range of 0.08-0.1 at room temperature. A low glass transition temperature silicon-containing block is chosen here in order to improve the self-assembly kinetics. Also, this block copolymer can be synthesized in industrial conditions with an extremely low metal contamination and a high etch

resistance of the Si-block is anticipated without additional processing steps (infiltration).

However, the integration of a BCP into a chemo-epitaxy process-flow does require neutral materials for the top and bottom interfaces of the film in order to provide perpendicular BCP's features. In this view, Arkema developed various materials to satisfy neutrality conditions and other requirements inherent to microelectronic processes (Fig. 1). For instance, the underlayer and the top-coat materials are both silicon-free so as to maximize and optimize the available aspect-ratio of perpendicular silicon-containing features versus etch-plasma chemistry for transfer into the underlaying substrate. These materials are also designed so as to be processed under standard time and temperature conditions of regular microelectronic processes to ensure a high throughput of silicon wafers (i.e. the neutral underlayer can be grafted following a process at 200°C during 75 seconds). An example of cross-section STEM imaging of a 7 nm half-pitch polymer (thermally annealed at 160 °C for 5 min to initiate the self-assembly) sandwiched between a grafted neutral underlayer (4 nm thick) and a 20 nm thick top-coat is given in Fig. 2.
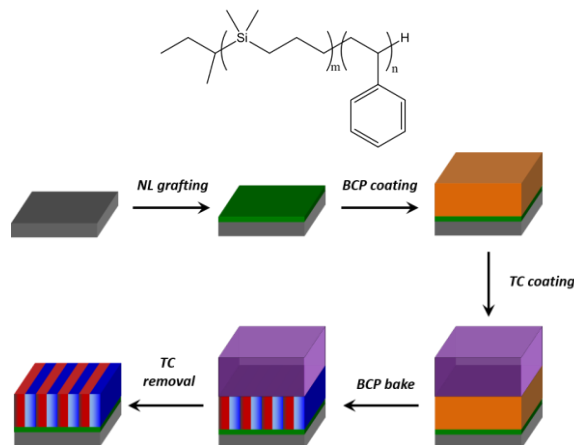

Figure 1. Chemical formulae of used lamellar PS-b-PDMSB and schematic of the process used to obtain perpendicular lamellas using a grafted neutral layer (NL) and a neutral top-coat (TC).
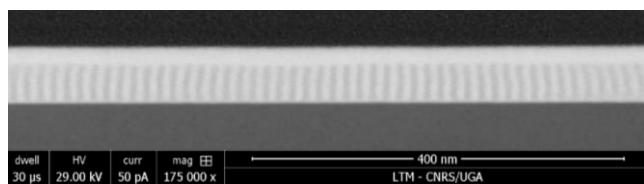

Figure 2. Cross-section STEM image of a 14 nm period, 40 nm thick PS-b-PDMSB layer thermally assembled between a neutral underlayer and a neutral top-coat onto a silicon wafer.

III. PLASMA ETCHING

Top-coat, PS and neutral underlayer are removed by dry-etching in a 300 mm industrial plasma reactor (Applied Materials). A pure Cl2 plasma chemistry is used for top-coat and BCP layer etching, providing a good control on both selectivity and etch rate. The etch rate of the BCP film can be independently adjusted from the selectivity between blocks. Examples of BCP surfaces at this step for two polymers are reported in Fig. 3. Then, an additional Ar/O2 step is performed to remove the PS block and oxidize the PDMSB block. By using Argon-rich gas mixtures, one can sufficiently modify the PDMSB block and no collapse of the lines is observed as illustrated in Fig. 4 (left). In order to limit the impact on well-known microloading effects, a Ar/HBr/N2 plasma chemistry is preferred to Ar/O2 to etch the grafted neutral underlayer. Though promising, early tests of silicon transfer with a standard process show greater roughness than after BCP reveal (Fig. 4 right). This roughness is due to the redepositing of etch products and optimizations are undergoing in other plasma chemistries designed for non-sticking etch products.
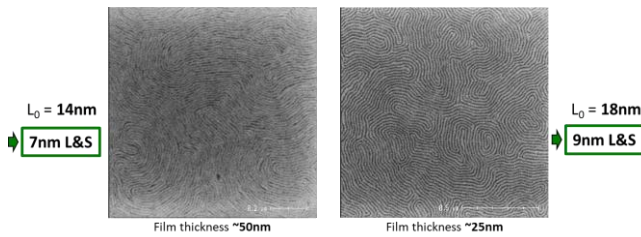
Figure 3. Top-view SEM observations of two different polymers (14 and 18 nm periods) after removing the top-coat and a 5s-long Ar/O2 plasma for PDMSB revelation.
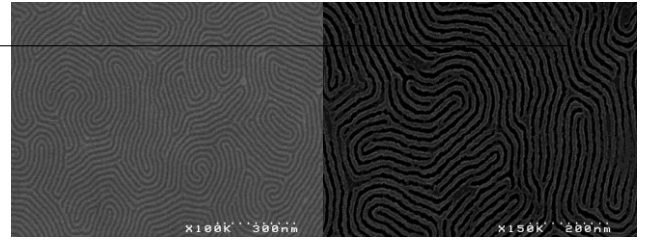
Figure 4. Top-view SEM images of the 18 nm period polymer after removing the top-coat in a Cl2 plasma chemistry and etching the PS block in a Ar/O2 chemistry (left), and after first attempts at transferring theses PDMSB features into the silicon wafer (right).

FABRICATION OF INDIUM TIN OXIDE PHOTONIC CRYSTAL USING HYDROGEN SILSESQUIOXANE RESIST

J. Solard, M. Chakaroun and A. Boudrioua

Laboratoire de Physique de Lasers CNRS UMR 7538, 99, avenue Jean-Baptiste Clément, 93430 Villetaneuse, France

jeanne.solard@univ-paris13.fr

Topic: nanopatterning

Abstract— **We report the fabrication of a photonic crystal of indium tin oxide and the investigation of the effect of the process key parameters. Triangular lattice of air holes (r=110 nm and a=290 nm) have been obtained using e-beam lithography combined with inductively coupled plasma etching through a 300 nm hydrogen silsesquioxane resist mask.**

I. INTRODUCTION

Indium tin oxide (ITO) thin films are key layers in many optoelectronic devices playing the role of transparent and conductive films. For instance, in the field of organic photonics, they are used as a anode on which is deposited the organic hetero-structure of the OLED. However, in the context of recent development of organic light sources, organic laser diode is still an important endeavor and a challenging issue, mainly due to the high lasing threshold under electrical pumping which is several orders higher than the allowed OLED current density [1]. To deal with this issue, one of the on-going studies of our group is to fabricate a photonic crystal (PhC) micro-cavity laser with a laser threshold current density at a level compatible with the OLED current density. In this context, we report the fabrication of PhC patterns directly on the ITO layer as a first step to prepare the investigation of OLED in PhC microcaviy. Hydrogen Silsesquioxane (HSQ) resist is used as mask because of its high resistance to etching process but a specific process needs to be developed. Indeed, the realization of dense high aspect ratio features (such as PhC) in thick HSQ resist remain challenging because of the chemical instability of this resist. The effect of different process parameters are investigated: HSQ resist patterning and mask transfer by ICP etching with the aim to obtain a low loss optical micro-cavity.

II. MATERIALS AND METHODS

HSQ type FOX 16 (Dow Corning) was spin-coated for a thickness of 300 nm on commercial substrates of glass with 150 nm ITO coating. The nanostructures were defined by e-beam lithography writing using a Raith Pioneer system operating at 30 keV with a beam current of 50 pA. The time and temperature of the resist baking and the type of developer were varied.

An ICP-RIE system (Corial 200 IL Dry etcher) was used to transfer the HSQ patterns into the ITO layer. ITO thin films were etched in BCl_3/Cl_2 plasma. The following parameters were varied: RF power (50-250 W), ICP power (600-1000 W) and chamber pressure (5-30 mTorr).

The processed features were characterized by atomic force microscope (AFM) and SEM (Raith Pioneer system) imaging.

III. RESULTS AND DISCUSSION

A. HSQ resist processing

HSQ is an attractive negative tone resist. Numerous efforts have been made to optimize the different process conditions such as electron beam dose [2], baking and developing temperature [3], type of developers and developing time [4, 5]. To achieve high aspect ratio dense pattern into the HSQ resist, we have to optimize the process.

The effect of baking was investigated with different time and temperature but also different post bake exposure process. No baking (Fig. 1a) shows the best contrast but makes the resist swell during development process. Too high temperature and too long baking time increase the sensibility of the resist. HSQ resist becomes sensitive to backscattering electrons during e-beam lithography and the inside of the holes is insolated, leaving HSQ inside the holes after development, reducing the average height of the holes.

We improved drastically the contrast of HSQ resist by adding salt to the TMAH solution for the development step. Best results were clearly obtained with the salty developer (Fig. 1b and 1c). We also optimized time development, varying the immersion time.
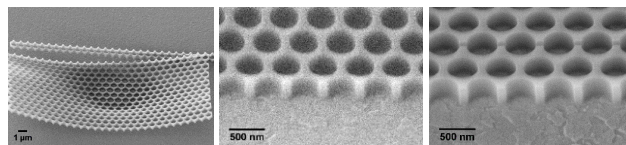

Figure 1. Comparison of SEM image of the developed HSQ resist with the design of PhC (a) no baking (b) development in TMAH solution (c) development in TMAH/NaCl solution. The average height of the holes measured by AFM is (b) 162 nm (c) 304 nm

B. Etching optimization

Patterned resist obtained with the optimization of HSQ processing was then used as a mask to transfer the PhC patterns into the 150 nm thick ITO layer. BCl_3/Cl_2 mixture with flow rate of 16:4 sccm was kept constant.

Pressure was varied from 5 mTorr to 30 mTorr. The increase of chamber pressure increases the density of

reactive Cl, changing the dominant etching mechanism from ion bombardement to a chemically assisted reaction.

The RF power was varied from 50 W to 250 W. The increase of RF power increases ion energy impinging on the surface which leads to a more efficient breaking of ITO bonds and improves sputter desorption of non volatil etch products from the surface.

The ICP power source was varied from 50 W to 250 W. As source power increases, the height of holes increases because of higher concentrations of reactive species and energetic ions, which enhance etch rate.
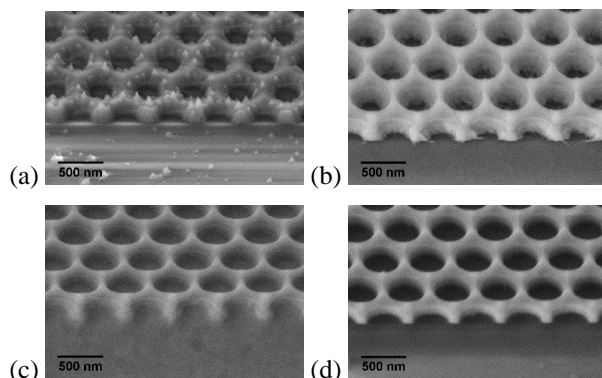
Figure 2. SEM tilted top view image of the ITO etch layer at (a) pressure of 5mTorr (b) RF power of 50 W (b) ICP power of 600 W (d) optimal etching parameters.

Eventually, as an example, we fabricated a PhC with a triangular lattice configuration consisting of air holes radius of 110 nm and lattice constant of 290 nm in a 150 nm thick ITO film. Typical result is displayed on figure 3 indicating a PhC micro-cavity of H2.
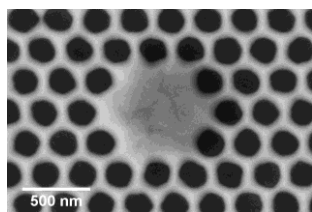
Figure 3. SEM top view image of the ITO PhC micro-cavity.

IV.   CONCLUSION

In summary, we developed a specific process in order to fabricate a photonic crystal in a 150 nm thick ITO layer. Best process parameters were found to obtained smooth and straight profile of the holes for the PhC. The ability to fabricate PhC patterns of ITO confirms the possibility of using this fabrication process to realize PhC micro-cavity in the visible range to be used in order to study low threshold laser application in the field of OLED compatible with electrical pumping.

REFERENCES

[1]   M. A. Baldo, D. F. O'Brien, M. E. Thompson, and S. R. Forrest, "Prospects for electrically pumped organic lasers," Phys. Rev. 66, 1–16 (2002).

[2]   M. J. Word, I. Adesida and P. R. Berger, "Nanometer-period gratings in hydrogen silsesquioxane fabricated by electron beam lithography", J. Vac. Sci. Technol. B 21, L12-15 (2003).

[3]   S. Choi, N. Jin, V. Kumar, I. Adesida and M. Shannon, "Effects of developer temperature on electron-beam hydrogen silsesquioxane resist for ultradense silicon nanowire fabrication", J. Vac. Sci. Technol. B 25, 2085-2088 (2007).

[4]   D. Lauvernier, J.-P. Vilcot, M. Francois, and D. Decoster, "Otimization of HSQ resist e-beam processing technique on GaAs material", Microelectron. Eng. 75, 177-182 (2004).

[5]   H.-S. Lee, J.-S. Wi, S.-W. Nam, H.-M. Kim, and K.-B. Kim, "Two-step resist-development process of hydrogen silsesquioxane for high-density electron-beam nanopatterning" J. Vac. Sci. Technol. B 27, 188 (2009)

ADVANTAGES OF NANOIMPRINT LITHOGRAPHY FOR PRODUCTION OF HIGH QUALITY DIFFRACTIVE OPTICAL ELEMENTS (DOES)

S. Drieschner, F. Pawlitzek, V. R. Kolli, M. Zoberbier, E. Storace, M. Hennemeyer

SUSS MicroTec Lithography GmbH
Schleißheimer Str. 90, 85748 Garching, Germany

E-mail: eleonora.storace@suss.com

Topic: Etching, lithography and nano-patterning, Integration and applications of micronanotechnologies

Abstract—**Nanoimprint lithography is proving itself as particularly suited technology for the production of Diffractive Optical Elements (DOEs), successfully addressing all the specific requirements that high-volume production poses.**

The possibility to enhance human perception of the surrounding environment by embedding information from sources other than our senses into what we see is boosting the commercial interest into optical devices which can be implemented into head-mounted AR equipment. Diffractive optical elements (DOEs) are considered as the most promising candidate to meet the market's requirements such as compactness, low-cost, and reliability [1] as they replace large display headsets for mixed reality (MR) by light-weight glasses. Their structures can vary from simple optical gratings for diffractive wave guides [2] to binary elements or pyramid-like multilevel structures [3]. When targeting a large volume production, current manufacturing techniques such as greyscale lithography, direct writing using laser or electron beams, and direct machining are starting to show their limitations: low process variability and surface precision, high equipment costs, and low volumes [3]. In contrast, soft lithography replication offers a pathway to the fabrication of large area DOEs with high aspect ratios, multilevel features, and critical dimensions below the diffractive optical limit down to 50 nm. In combination with UV-curable materials, the fabrication time can be significantly reduced in comparison to, e.g. hot embossing replication methods, making it very appealing to industrial applications [3].

Here, a very effective approach to fabricate high quality DOEs using nanoimprint lithography based on porous soft stamp materials is presented (see SEM image in Figure 1). Uniformly spin-coated substrates are brought in contact with a working stamp at atmospheric pressure, and a full-field imprint is demonstrated, free of air enclosures, answering to the high yield requirements of a high-volume low-cost manufacturing line.

Key parameters to qualify DOEs structures are the Total Thickness Variation (TTV) of both the feature height and the Residual Layer Thickness (RLT), here optimized to show the highest quality for the optical elements. Finally, in-machine separation of the substrate from the stamp enables high production rates and promotes the suitability of this technique for mass production.
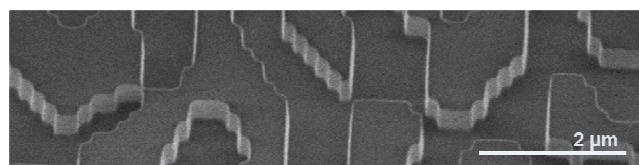

Figure 1. Tilted top view SEM image of a binary diffractive optical element using nanoimprint lithography.
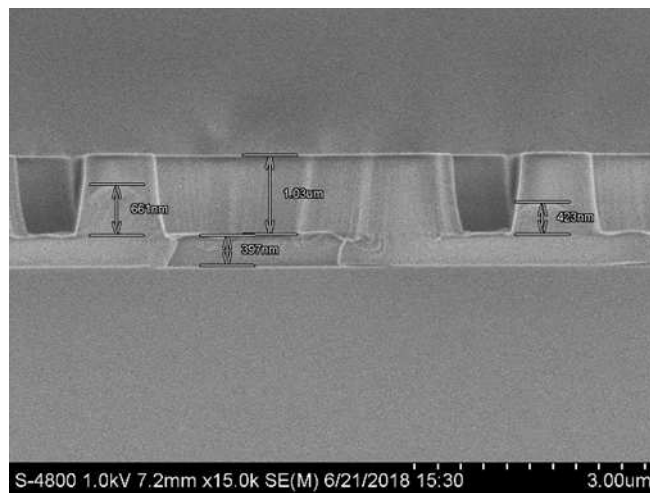

Figure 2. SEM side view image of a diffractive optical element on a silicon substrate.

REFERENCES

[1] Donald C. O'Shea; Thomas J. Suleski; Alan D. Kathman; Dennis W. Prather: Diffractive Optics: Design, Fabrication, and Test (2004), SPIE, ISBN: 9780819451712

[2] Jingjing Guo, Yan Tu, Lanlan Yang, Lili Wang, and Baoping Wang: Holographic waveguide display with a combined-grating in-coupler, Applied Optics, 55 (2016), 32, p. 9293-9298.

[3] M. T. Gale: Replication techniques for diffractive optical elements, Microelectronic Engineering, 34 (1997), 3-4, p.321-339

TECHNOLOGICAL PROCESS FOR THE FABRICATION OF THICK TITANIA FILMS AND DEEP TiO$_2$ SOL-GEL GRATING.

Maria USUGA HIGUITA[1,2], Nicolas CRESPO-MONTEIRO[1], Francis VOCANSON[1], Michel LANGLET[2], Yves JOURLIN[1*].

[1] Univ Lyon, UJM Saint-Etienne, Laboratoire Hubert Curien Saint-Etienne, F-42023 France

[2] Univ. Grenoble Alpes, LMGP, F-38000 Grenoble, France, CNRS, LMGP, F-38000 Grenoble, France

*Yves.jourlin@univ-st-etienne.fr.

Topic: *photo-sensitive TiO$_2$ sol-gel film, deep grating, high diffraction index.*

Abstract: This paper describes a method to obtain thick titania films with high diffractive index (above 2.2) by sol gel-method. It is based in a multilayer sol-gel deposition allowing to obtain thick photosensitive sol-gel films. In a second step these films are microstructured using UV light to obtain a deep grating.

I. INTRODUCTION

Titanium oxide films have largely studied for a great number of applications[1], like photocatalysis, coatings for optics, sensors or waveguides. In the case of waveguide, TiO$_2$ is interesting due to its high refractive index (up to 2.2) and its lossless properties in the visible and near infrared wavelength range[2]. TiO$_2$ layers can be obtained by different techniques such as CVD, PVD or sol-gel method[1]. The last one attracts a lot of attention because it is a soft chemistry method, and it allows to develop films with a wide variety of thicknesses. This cheap and flexible method can be applied to large area substrates and unconventional geometries.

Literature demonstrates that deposition of thick inorganic layer by sol-gel creates a lot of cracks at the surface; also it is a real difficulty to achieve the deposition of sol-gel layer above 300 nm thick layers[3]. Moreover, one knows that to obtain higher refractive index, annealing processes are needed, but the thermal process reduces notably the thickness, limiting their use in particular in the field of waveguides and optical components.

In this paper, we show a method to fabricate thick anatase titania films with a high refraction index using a multi-layer sol-gel deposition process with a thermal treatment at 300°C between each layer.

Following the same sequence another method is proposed consisting in a multilayer deposition, with short thermal treatment to keep the photo sensitive properties of sol-gel, in order to print deep periodic gratings.

II. EXPERIMENTAL PROCEDURE.

A. Sol-gel method.

A specific sol-gel formulation has been prepared from titanium isopropoxide (TIPT) complexed by Benzoylacetone (BzAc) in methanol and butanol (molar ratio TIPT/BzAc/MeOH/BuOH: 1/20, 4/0, 75/23, 9), the whole process being previously published[3].

The specificity of this sol-gel is the photosensitive properties of TIPT-BzAc complex, which make it photo-patternable under UVA light. Under UVA, the complexed species is partially degraded in carbonates and/or carboxylates which are insoluble in ethanol that induces a contrast of solubility between irradiated and non-irradiated areas. This photo-patternable sol-gel acts like a negative photoresist and its properties are interesting to obtain micrometric or submicrometric structures using a simple mask or laser beam[4].

B. Thick anatase titania films.

In order to obtain thick anatase titania films, a multilayer sol-gel deposition process is used. The films are developed with the previous sol-gel. The first film is deposited by spin coating on a silica substrate; it leads a xerogel film, which is heated in an oven at 300°C for 1h. Then, a second layer is added using the same deposition conditions as the first layer. After that, a final thermal treatment at 500°C during 3h is made in order to obtain a densified crystallized layer with a high refraction index (TiO$_2$ anatase) (fig 1).
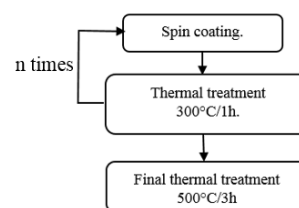

Figure 1. Schema of process to obtain thick anatase titania films

This method makes to obtain a range of thicknesses according to the number of layers. Table 1 shows the different thicknesses obtained. Films are crack-free and homogeneous.

TABLE I. MEASURE THICKNESSES OF ANATASE TITANIA FILMS.

TiO₂ anatase.			
	1 layer	*3 layers*	*4 layers*
Thickness	~60	~92	~125

Figure 2. Picture of obtained films with 1 layer, 3 layers and 4 layers, respectively.

C. Thick photo-patternable titania films for obtaining deep TiO₂ grating.

The realization of deep TiO₂ grating with a high refraction index is not possible with the previous method. Indeed, the heat treatment at 300°C causes a loss of photosensitive properties by degrading the complexed species (BzAc), consequently the direct photo-patternable by UVA is impossible.

In order to maintain the photo-patternable properties of sol-gel a second method is proposed to obtain thick photo-patternable titania films. This method consists also of a multilayer deposition, but in this case, the thermal treatment between each layer is different to preserve the complexed species (TIPT-BzAc) and consequently the photo-patternable property. Thermic treatment at 110°C during 5 minutes is made after deposition of layer, to avoid the dissolution between each layer (fig.3).
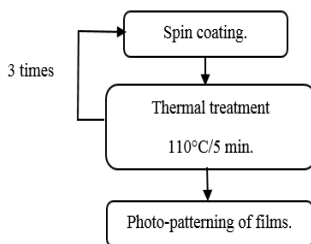
Figure 3. Schema of process to obtain thick photo-patternable titania films

The deep TiO₂ grating is elaborate using thick sol-gel films with 3 layers. The grating is printed on the sample by UV illumination through a chromium photomask of 4 µm period during 10 min under a 365 nm wavelength collimated light. Then a short thermal treatment at 110°C is made to stabilize the insolated and non-insolated areas. The development of samples is obtained by washing in ethanol, which induces the dissolution of non-insolated areas. Then the films are rinsed with deionized water.

The figure 4 shows a comparison between a grating realized in a monolayer and a three-layers film and the AFM profiles of these gratings (figure 4c and 4d, respectively).The height of patterns is around 360 nm for multilayer film (fig 4d) and 240 nm for monolayer film (fig. 4c). These results show that it is an interesting method to obtain deep gratings
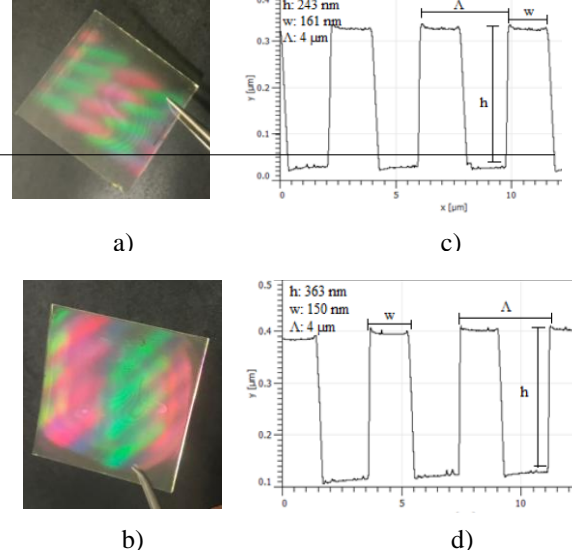

Figure 4. Pictures of gratings obtained from a) monolayer and b) multilayer photo-patternablesand their AFM profile (c,d).

III. CONCLUSION AND PERSPECTIVES.

A simple method to obtain thick titania films by sol-gel has been successfully tested and described. We have fabricated thick homogeneous and crack-free titania films using a multilayer deposition and an annealing at 300°C between each layer and a thermal treatment at 500°C to obtain a densified titania anatase film.

A second method based on multilayer deposition and a short thermal treatment at 110°C was realized in order to keep the photo-sensitive properties of sol-gel. A homogeneous deep TiO₂ grating was obtained from this reproducible process.

Perspectives concern the determination of optical losses and the influence of interfaces between layers for thick anatase titania films.

In order to have a high index deep grating, next step is the crystallization of TiO₂ grating by thermal process at 500°C. Optical and microstructure characterization will also be performed.

REFERENCES

[1] A X. Chen, S.S. Mao, "Titanium Dioxide Nanomaterials: Synthesis, Properties, Modifications, and Applications," Chem. Rev., vol. 107, pp. 2891-2959, 2007.

[2] Y. Liang, H. Liu, F. Wang, H. Meng, J. Guo, J. Li and Z. We, "High efficiency, near-diffraction limited, dielectric metasurface lenses based on crystalline titanium dioxide at visible wavelengths," Nanomaterials, vol. 8, pp. 288, 2018.

[3] S. Briche, Z. Tebby, D. Riassetto, M. Messaoud, E. Gamet, E. Pernot, H. Roussel, O. Dellea, Y. Jourlin, M. Langlet, "New insights in photo-patterned sol–gel-derived TiO₂ films," J. Mat. Sci., vol. 46, pp. 1474-1486, 2011.

[4] V. Gâté, Y. Jourlin, F. Vocanson, O. Dellea, G. Vercasson, S. Reynaud, D. Riassetto, M. Langlet, "Sub-micrometric patterns written using a DIL method coupled to a TiO₂ photo-resist", Opt. Mater., vol. 35, pp 1706-1713, 2013.

Modifying Ta_2O_5 material properties by tuning directional ions during Plasma Enhanced Atomic Layer Deposition

YEGHOYAN Taguhi, PESCE Vincent, BONVALOT Marceline, VALLEE Christophe
Univ. Grenoble Alpes, LTM-CNRS, F-38000 Grenoble, France
taguhi.yeghoyan@cea.fr

Keywords: **Ta_2O_5, Plasma Enhanced Atomic Layer Deposition, substrate bias, ion directionality, resistive memories**

Abstract— **An emerging approach for Area Selective Deposition (ASD) can potentially resolve the lithography issues for the latest technology nodes. It is based on directional ions usage, during Plasma Enhanced Atomic Layer Deposition (PEALD), which results in controllable material properties. In this report, we use such approach for Ta_2O_5 properties modification.**

I. OVERVIEW

The deposition processes using plasma-based technology have several advantages over standard thermal ones. Some applications include lowering the processing temperature while increasing the deposition rate, lowering the consumption of gases for deposition, and avoiding the use of polluting chemicals for etching and post-processing.

For deposition processes, plasma-based technologies are also considered to improve the film quality such as stoichiometry and purity. For that however, plasma-based processes must be carefully optimized. Aside from standard parameters such as process temperature, time, pressure or precursor flux, additionally, the plasma source, its power, density and eventually substrate bias can be tuned. Such tuning of deposition parameters is even more important when deposition is carried out with atomic precision with Plasma Enhanced Atomic Layer Deposition (PEALD), a technique that has proven compatibility with continuous micro and nano-electronics miniaturization.

However, the complexity of such process can be used as an advantage for tailoring the substrate functionalization and/or thin-film properties. Ultimately, this can lead to Area Selective Deposition (ASD) which is a trending topic that, coupled with ALD, could potentially replace costly and technologically challenging nano-patterning. In our laboratory, ASD has been successfully implemented with atomic precision for Ta_2O_5 and TiO_2 thin-films, using nucleation delay on various surfaces coupled with in-situ etch [1, 2, 3]. Additionally, other groups reported that ASD can be also done ex-situ by wet etch post-processing of SiN_x with variable stoichiometry and density, by employing variable substrate bias during the ALD growth [4].

II. RESULTS

In this work, we report a combination of the above-mentioned ASD methods for Ta_2O_5 thin-films deposited on thermal SiO_2 seed. By using different substrate temperature and varying the substrate bias, we show that while keeping a similar growth duration, the refractive index, density and purity can be tailored (see Figure 1).
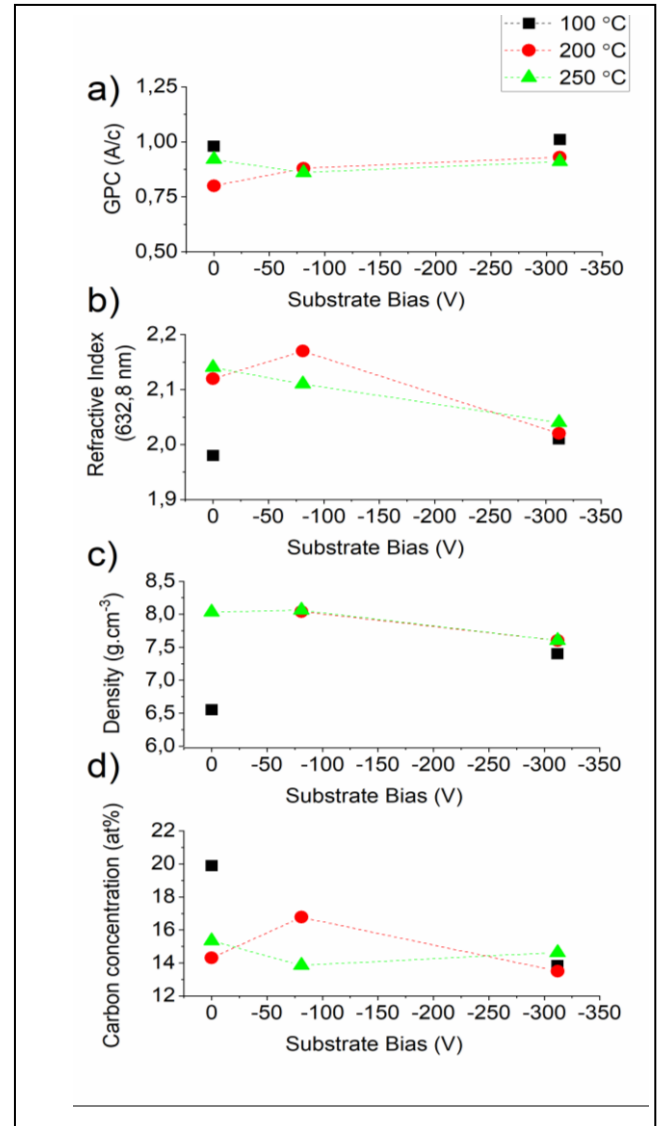

Figure 1. a) Growth per cycle (GPC), b) refractive index, c) density and d) carbon atomic concentration of PEALD deposited Ta2O5 thin-films at various temperatures and with various substrate bias. Note that the lines between the measurement point are a guidance for eyes.

We show that that the strongest effect on film quality occurs for a substrate temperature of 100°C, where the film quality improves for -319V of substrate bias. It is argued that the reason for this is a local increase of temperature at the extreme thin-film surface by usage of directional ions. This is interesting for temperature-sensitive applications of Ta_2O_5 such as gate dielectric for organic thin-film transistors [5]. Moreover, ions directionality can be

potentially integrated into ASD of 3D structures, a continuation of the previous work in our laboratory for resistive memory applications.

REFERENCES

[1] R. Vallat, R. Gassilloud, B. Eychenne, and C. Vallée, "Selective deposition of Ta2O5 by adding plasma etching super-cycles in plasma enhanced atomic layer deposition steps" in Journal of Vacuum Science & Technology A 35, 01B104, 2017

[2] A. Chaker, C. Vallee, V. Pesce, S. Belahcen, R. Vallat, R. Gassilloud, N. Posseme, M. Bonvalot, and A. Bsiesy, "Topographically selective deposition", Applied Physics Letters 114, 043101, 2019

[3] R. Vallat, R. Gassilloud, O. Salicio, K. El Hajjam, G. Molas, B. Pelissier, and C. Vallée, "Area selective deposition of TiO2 by intercalation of plasma etching cycles in PEALD process: A bottom up approach for the simplification of 3D integration scheme", Journal of Vacuum Science & Technology A 37, 020918, 2019

[4] T. Faraz, H. Knoops, E. Kessels, "Ion energy control during plasma-enhanced atomic layer deposition:enabling materials control and selective processing in the third dimension" Nevac Blad, 57(1), 6-10, 2019

[5] C. Bartic, H. Jansen, A. Campitelli, S. Borghs, "Ta2O5 as gate dielectric material for low-voltage organic thin-film transistors", Organic Electronics 3 (2), 65-72, 2002

MOCVD grown InAs/GaAs quantum dots on GaAs and Ge/Si substrates

O. Abouzaid[1, 3], M. Martin[1], J. Moeyaert[1], B. Salem[1], S. David[1], F. Bassani[1], A. Souifi [2], N. Chauvin[2], J. M. Bluet[2], A. Ahaitouf [3], Az. Ahaitouf [4], T. Baron[1]

[1] Univ. Grenoble Alpes, CNRS, CEA-Leti, MINATEC, LTM, F-38054 Grenoble, France

[2] Université de Lyon, Institut des Nanotechnologies de Lyon (INL)-UMR5270-CNRS, INSA-Lyon, 7 avenue Jean Capelle, 69621 Villeurbanne, France

[3] LERSI, FSTF, Univ. Sidi Mohamed Ben Abdellah, B.P. 2202 – Route d'Imouzzer Fès, Morocco

[4] Univ. Sidi Mohammed Ben Abdellah, FP Taza, LSI, B.P. 1223, Taza, Morocco

abouzaidoumaima@gmail.com

Topic : **Intégration et applications des micronanotechnologies**

Abstract— **Direct epitaxial growth of III –V semiconductor materials on Si is one of the most promising candidates for the fabrication of efficient electrically pumped light sources on a Si platform. In this work, the growth of InAs/GaAs quantum dots (QDs) on both GaAs and Ge/Si (001) 300 mm nominal substrates is investigated using an industrial MOCVD (Metal Organic Chemical Vapor Deposition) tool.**

I. INTRODUCTION

III-V semiconductors (GaAs, InAs, InP ...) have remarkable intrinsic properties. They exhibit a high electron mobility and, most often, a direct band gap allowing the emission of light in a wide spectral range (from UV to infrared) with a high quantum efficiency. They are thus materials of choice for producing light sources such as light emitting diodes and laser diodes. Their integration on a silicon CMOS platform would open wide perspectives in the field of silicon photonics and optical interconnections.

II. OPTIMIZATION OF THE GROWTH

We will report on the realization of As-based heterostructures allowing the fabrication of light sources emitting at around 1.3 µm. However, the hetero-epitaxy of As-based semiconductors on a silicon substrate remains a major challenge mainly due to the difference of lattice parameter and polarity of the materials. That is why, in the context of this work, to minimize the impact of structural defects on the emission properties of III-V materials, we have investigated the growth of InAs/GaAs quantum dots (QDs) on nominal Ge/Si (100) substrates by MOCVD in a 300 mm industrial type reactor. The optimization of the growth parameters leads to a high QD density ($\sim 10^9$ cm^{-2}) and a photoluminescence (PL) emission around 1.3 µm. Further PL investigations have been performed to probe the emission quality of these QDs grown on Ge/Si (100) substrates and compare them with QDs grown on GaAs substrates.

III. Application

As an application, we will report on InAs/GaAs QD photodetectors (PDs) grown on GaAs substrate operating around 1.3 µm at 300K. We studied the optical absorption mechanism using photocurrent technique. The comparison between the absorption thresholds and the photoluminescence peaks will also be presented.
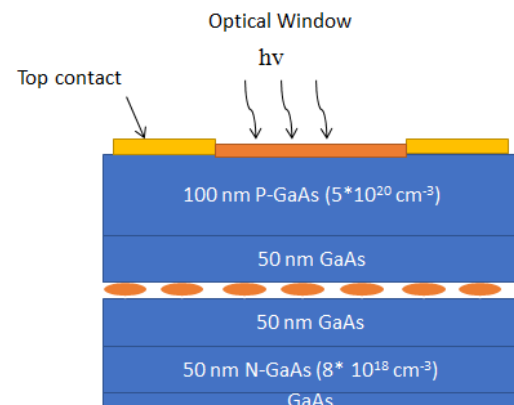

Figure 1 : Schematic diagram of the epitaxial photodetector structure

sciencesconf.org:jnte2019:291289

Towards Silicon Nanonet-based Flexible Electronics

T. Arjmand[a,b,c*], T. Nguyen[a], M.Legallai[b], B. Salem[b], M. Bawedin[c], C. Ternon[a]

a. Univ. Grenoble Alpes, CNRS, Grenoble INP, LMGP, F-38000 Grenoble, France.
b. Univ. Grenoble Alpes, CNRS, LTM, F-38000 Grenoble, France.
c. Univ. Grenoble Alpes, CNRS, Grenoble INP, IMEP-LaHC, F-38000 Grenoble, France.

∗ tabassom.arjmand@grenoble-inp.fr

Due to their flexibility, workability, lightness, fineness and reproducibility, randomly oriented nanostructured networks, also called nanonets (NNs), are an attractive material for flexible and large area electronics as a potential alternative to amorphous silicon or organic materials. Moreover, NN-based device integration process is based on simple technologies [1] and done at low temperature ($< 400°C$) compatible with some flexible substrates. The device geometry can vary from a micro-to-millimeter scale. As a consequence, such a material provides an interesting path to low cost devices [2]. To this end, by combining bendable NNs based on Si nanowires (SiNWs) with rigid (Si/Si3N4) and flexible (Kapton) substrates, we report on the successful fabrication and electrical characterization of rigid and flexible resistors and transistors using bottom-up fabrication and standard microelectronic technology. Both type of resistors, flexible or not, exhibit high electrical performances with linear characteristics, even if current has to flow through a succession of tens to hundreds of SiNWs, depending on device geometry, and as many SiNW-SiNW junctions. Electrical performance of flexible transistors are still under study, but rigid transistors with long channel ($1000\mu m$) exhibit outstanding performances with high drain current up to 10^{-7} A, I_{On}/I_{Off} ratio as large as 10^5 and a better mobility as compared to a-Si and organic materials [3].
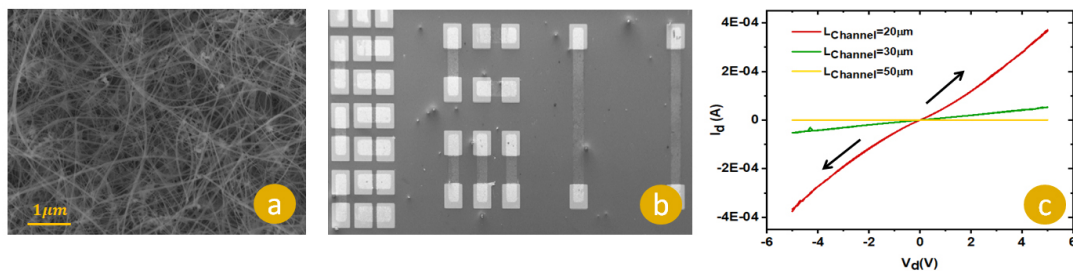
Figure 1: SEM image of as-fabricatedSiNN; (b) SEM image of SiNN-based devices; (c) Electrical characteristic of flexible NN-based resistor with channel length (L) from $20\mu m$ to $50\mu m$ which, clearly shows the great conduction of NN through numerous NW/NW junctions (NW length = 7 μm).

[1] M. Legallais et al., Solid State Electronics 143, 97-102 (2018)
[2] T.T.T. Nguyen et al, Nano Futures (2019) doi 10.1088/2399-1984/ab1ebc
[3] This work has received funding from the EU H2020 RIA project Nanonets2Sense under grant agreement $n°688329$

MULTIPLE HEATER-SENSOR MICROSYSTEMS ON A SINGLE GLASS SLIDE TO MONITOR CELL CULTURE TEMPERATURE

Alexandra Garraud[1], Gaëtan Debontride[2], Skandar Basrour[2], David Peyrade[1]
[1]Univ. Grenoble Alpes, CNRS, CEA/LETI Minatec, LTM, Grenoble, France
[2]Univ. Grenoble Alpes, CNRS, TIMA, Grenoble, France
alexandra.garraud@cea.fr

Topic : Intégration et applications des micronano-technologies

Abstract—**In this paper, we present a platform composed of three transparent heater-sensor microsystems capable of maintaining a cell culture at a desired temperature. Accurate and stable temperature conditions are therefore accessible throughout the entire culture cycle.**

I. INTRODUCTION

When working on biologic systems like cell cultures, environmental conditions need to be accurately controlled to obtain physiologically relevant data during the cell study [1,2]. Commonly, bulky incubators are used to regulate both temperature and surrounding gas composition. However, in recent years, thanks to the rise of microfluidics and bio-MEMS, more and more devices are designed to monitor the temperature at the cell culture level [3–5]. Those solutions are still relatively large and not compatible with a multiple-well plate: they have one active area, where the temperature is monitored, generally in the 1 mm^2 to 1 cm^2 range.

They are usually composed of one heater, and one or more temperature sensors. These heater-sensor systems are able to apply a desired temperature while monitoring it. It is common that the overall system is designed to be as much transparent as possible to avoid hindering subsequent cell observations. Therefore transparent conductive oxide materials such as indium tin oxide (ITO) would be preferred over using opaque Peltier modules to perform the heater function [6,7]. Accurate thermal sensing is also a key factor to obtain cell-friendly conditions. Thermocouples, diode temperature sensors or resistive temperature detectors (RTDs) can perform such measurements, each with their advantages and limitations [8]. For cell culture systems, RTDs are generally selected, with a preference for platinum as the sensing layer.

In this abstract, we present a transparent system capable of applying and measuring the temperature at three separate locations on a single glass slide. In the future, this will allow for accurately studying the temperature effects on cellular growth by performing parallel cell cultures where all other environmental conditions are kept constant apart from the temperature.

In Section II, we present the fabrication methods to realize the heater-sensor systems on a regular rectangular glass slide. Section III explains the numerical modeling and the related results. Section IV discusses the experimental results. Finally, Section V summarize the paper and considers future directions.

II. FABRICATION METHODS

The system is fabricated on a rectangular indium tin oxide coated glass slide (75 mm × 25 mm × 1.1 mm, Sigma Aldrich), with a sheet resistivity of 70-100 Ω/sq. Using a maskless photolithography tool [9] (SmartPrint, objective x2.5, SmartForce Technologies), the ITO heater pattern is defined on AZ1512 photoresist. ITO layer is then etched in an ICP plasma chamber (Plasmalab100, Oxford). A SiNx protective window (3 mm × 3 mm) is then deposited by PVD (CT100, Alliance Concept) over the active area. Being thermally conductive, silicon nitride will allow heat flux to move from the ITO heater to the Pt RTD while avoiding any short. Finally, the Pt layer is evaporated in a metal evaporator (MEB 550S, Plassys). Figure 1 shows a picture of the resulting glass slide with 3 heater-sensor systems, along with a zoom-in microscope image of the active area.
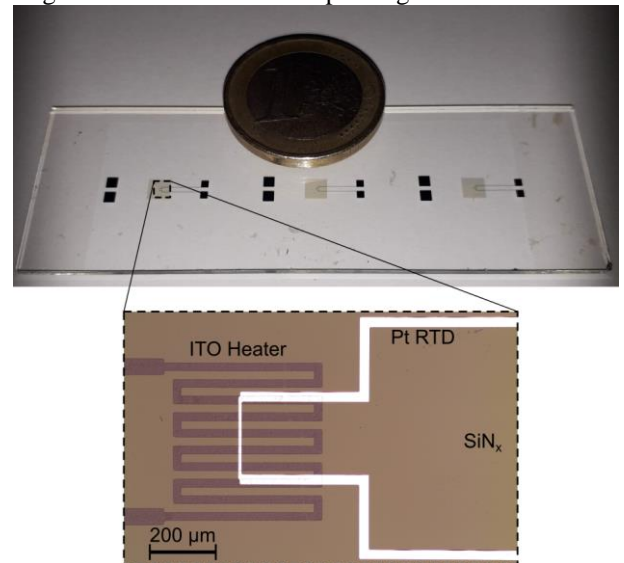

Figure 1 Picture of the glass slide with three heater-sensor microsystems. Zoom-in microscope image on the active area composed of the ITO heater and the Pt RTD, separeted by a SiNx protective layer.

III. NUMERICAL MODELING

ITO heater pattern is first modeled using ANSYS FEM software (v17). Several implementations of the design, modifying the numbers of meanders, are tested to obtain the most homogeneous temperature distribution over the active area (500 μm × 500 μm) without reaching the minimal resolution of the selected SmartPrint objective.

Three designs are compared: 3-meander, 5-meander and 6-meander. Figure 2 compares the temperature profiles

along the y axis for the three tested designs. While the 3-meander pattern lacks temperature homogeneity, the 6-meander design would require using a larger magnification objective resulting in a longer fabrication time. Therefore the 5-meander design is selected: the temperature does not vary more than 15 % across the active area.
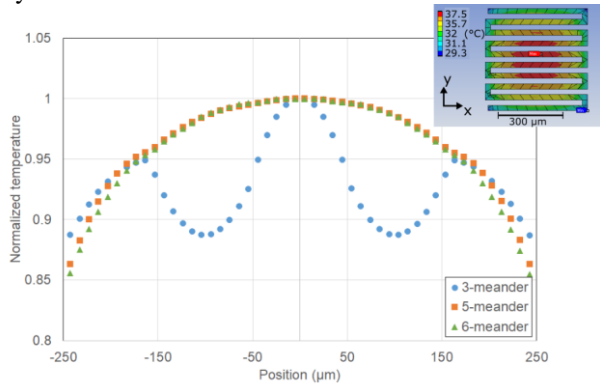

Figure 2   Temperature profile along the y axis depending on the ITO heater design. Inset: Temperature distribution for the 5-meander active area design.

IV.   EXPERIMENTAL RESULTS

A.   Pt Temperature Sensor Calibration

Once the device is fabricated, calibration can be initiated. First, the Pt resistance $[R(T) = R_0(\alpha T + 1)]$ is measured versus known temperatures to obtain α, the temperature coefficient of resistance and R_0, the resistance at 0 °C. Experiments are conducted in a temperature-controlled oven (Memmert UFP 400). Platinum resistance is measured with a Keysight B2901A sourcemeter by injecting a 100 µA current and measuring the resulting voltage.

Four different temperatures are selected for the Pt resistance calibration (Figure 3), spanning across the 37 °C temperature range the device will eventually work close to. A linear fit is found, with $\alpha=0.0024$ °C^{-1} and $R_0=587.83\ \Omega$, in accordance with the literature.
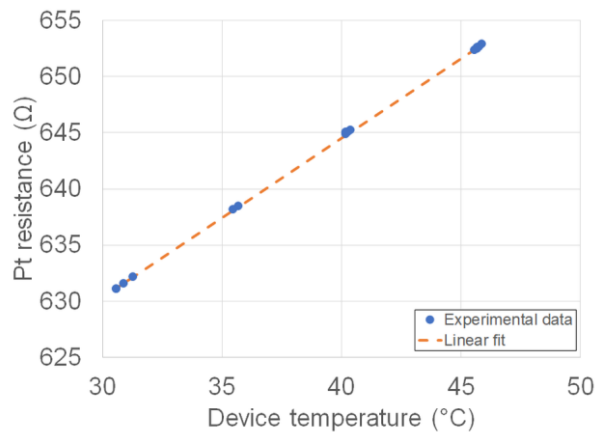
Figure 3   Pt resistance versus device temperature.

B.   ITO Heater Calibration

ITO heater is then characterized by injecting a known current while measuring the Pt resistance, resulting in the temperature determination. ITO current is controlled by a Keithley 2400 sourcemeter while measuring the Pt resistance with a Keysight B2901A sourcemeter.

Figure 4 presents the experimental data along with a quadratic fit. We determine that a 2 mA current is necessary

to reach a temperature of 37 °C, in accordance with the 1.9 mA predicted by the ANSYS simulations.
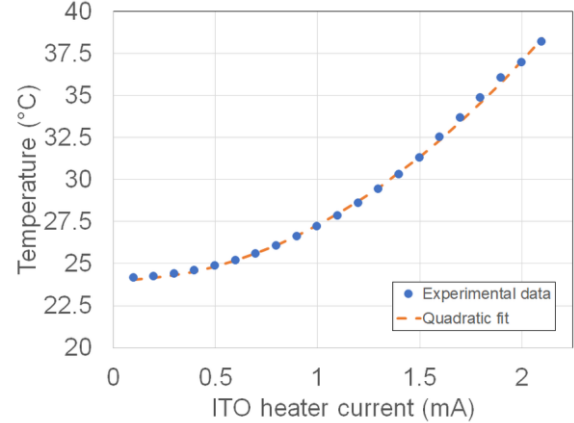
Figure 4   Pt resistance temperature versus ITO current.

V.   CONCLUSIONS AND PERSPECTIVES

A simple and transparent device capable of maintaining the temperature of the cells for three parallel cultures is demonstrated. Following a design optimization of the meander pattern through numerical simulations, the heater-sensor system is characterized and cell-friendly temperatures can be obtained.

In the future, cells will be grown on our device and compared to regular cell culture cases.

REFERENCES

[1] S.K. Das, S. Chung, I. Zervantonakis, J. Atnafu, R.D. Kamm, A microfluidic platform for studying the effects of small temperature gradients in an incubator environment, Biomicrofluidics. 2 (2008) 034106.

[2] T. Neutelings, C.A. Lambert, B. V. Nusgens, A.C. Colige, Effects of mild cold shock (25 °C) followed by warming up at 37 °C on the cellular stress response, PLoS One. 8 (2013) e69687.

[3] C.-W. Huang, G.-B. Lee, A microfluidic system for automatic cell culture, J. Micromechanics Microengineering. 17 (2007) 1266–1274.

[4] A.-J. Mäki, J. Verho, J. Kreutzer, T. Ryynänen, D. Rajan, M. Pekkanen-Mattila, A. Ahola, J. Hyttinen, K. Aalto-Setälä, J. Lekkala, P. Kallio, A Portable Microscale Cell Culture System with Indirect Temperature Control, SLAS Technol. Transl. Life Sci. Innov. 23 (2018) 566–579.

[5] J. Peng, C. Fang, S. Ren, J. Pan, Y. Jia, Z. Shu, D. Gao, Development of a microfluidic device with precise on-chip temperature control by integrated cooling and heating components for single cell-based analysis, Int. J. Heat Mass Transf. 130 (2019) 660–667.

[6] V. Miralles, A. Huerre, F. Malloggi, M.-C. Jullien, A Review of Heating and Temperature Control in Microfluidic Systems: Techniques and Applications, Diagnostics. 3 (2013) 33–67.

[7] R. Pawlak, M. Lebioda, Electrical and Thermal Properties of Heater-Sensor Microsystems Patterned in TCO Films for Wide-Range Temperature Applications from 15 K to 350 K, Sensors. 18 (2018) 1831.

[8] F. Yang, N. Yang, X. Huo, S. Xu, Thermal sensing in fluid at the micro-nano-scales, Biomicrofluidics. 12 (2018) 041501.

[9] J. Cordeiro, M. Zelsmann, T. Honegger, E. Picard, E. Hadji, D. Peyrade, Table-top deterministic and collective colloidal assembly using videoprojector lithography, Appl. Surf. Sci. 349 (2015) 452–458.

ROBUST ATMOSPHERIC PRESSURE PLASMA SOURCE FABRICATED BY MICROFABRICATION TECHNIQUES

R. Michaud, A. Stolz, S. Iséni, O. Aubry, P. Lefaucheux, and R. Dussart

GREMI, Polytech'Orléans/CNRS, 14 rue d'Issoudun, BP 6744, 45067 ORLEANS Cedex 2 France

ronan.michaud@univ-orleans.fr

Topic : Integration of technologies

Micro hollow cathode discharges (MHCD) operating in DC close to atmospheric pressure in different gases are produced on silicon platforms. Microplasmas were optically and electrically characterized. The micro reactors were also analyzed after operation by SEM observations. Stability enhancement allowed tests of a new geometry that allowed a higher current and power (up to 1 W per microdischarge).

I. INTRODUCTION

Micro hollow cathode discharges (MHCD) operating in DC were first introduced in the mid-90s [1]. Due to their dimensions and their large surface to volume ratio, the produced micro plasma remains cold and can operate at atmospheric pressure in a stable and normal discharge regime as long as the cathode area is not limited [2]. MHCD on silicon platforms were first studied by J. G. Eden's group [3]. Silicon processing, developed for microelectronic devices, offers many opportunities to design new, original and efficient devices to produce high-density microplasmas.

An array of 1064 microplasmas using an etched silicon cathode was totally ignited [4]. However, the operation of the device was not stable and produced many current spikes that significantly damaged the micro cavities and lead to the device failure. The mechanism responsible for this unstable regime and the short microdischarge lifetime was investigated [5] and a solution was found to enhance the robustness of the micro reactors [6].

II. EXPERIMENT

A single hole microdischarge reactor is schematically represented in figure 1 (a). A ballast resistor is used to limit the current. To avoid instabilities during plasma operation, the silicon cathode is covered by a metal thin film (nickel in this example).

More than 15 individual process steps are necessary to create such a structure. This CMOS-compatible device fabrication allows the investigation of different electrode materials. Then, in an argon or helium environment, the microdischarges were operated to compare the stability and the lifetime of the device.
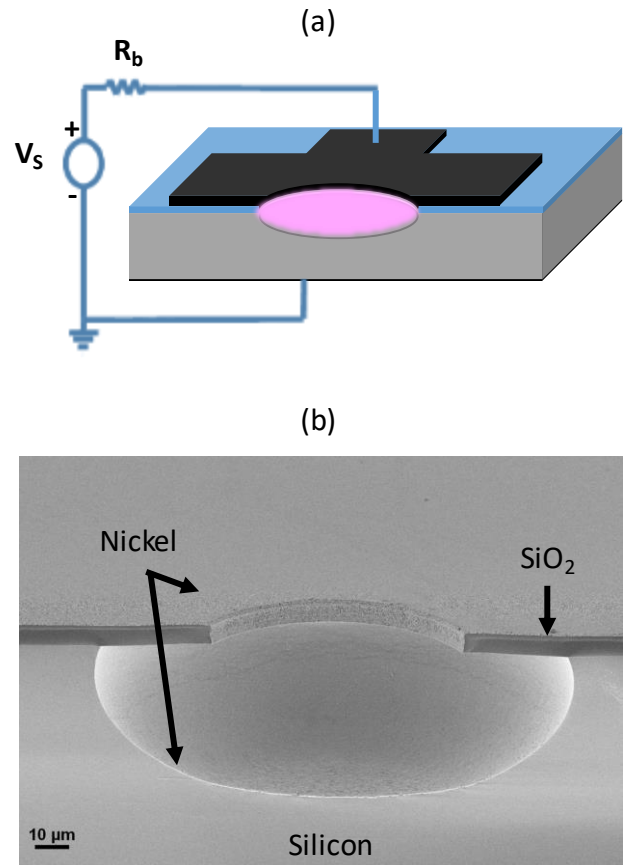
Figure 1. (a) Schematic of a microdischarge reactor. (b) Cross-sectional SEM picture of a microdischarge reactor before use.

III. RESULTS

In both gases and in a large range of pressure, a very stable operation has been obtained by using the cavity configuration with nickel cathode. An example of a single hole microdischarge operating at atmospheric pressure in argon (100 µm diameter cavity) with a cathode of nickel is shown in figure 2 (a). The lifetime of the microdischarge reactor with these parameters can be longer than 24 hours.

Another example of microdischarges operation is shown in figure 2 (b). In this case, an array of 576 microdischarges was ignited in helium at 100 torr. Several tens of mA can be injected in this type of device without observing any damage.
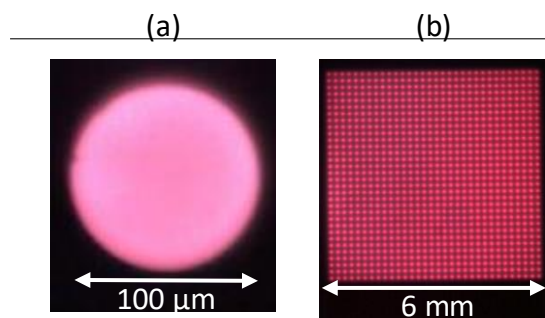
Figure 2. Real pictures of (a) a single hole microdischarge operating in argon at atmospheric pressure and of (b) an array of 576 microdischarges operating in helium at 100 torr.

The cathode surface after operation presents much less damage when it is made of nickel compared to nickel. Figure 3 presents two SEM pictures of the micro reactor surface after operation in (a) helium or in (b) argon at atmospheric pressure in single hole cavity configuration.

After helium operation, no damage was found on the cathode surface. However, after argon operation, a ring-shape structure appears in the center of the cavity. This is explained by pulverization and redeposition process caused by ions bombardment being more efficient in argon plasmas.

REFERENCES

[1] K. H. Schoenbach, R. Verhappen, T. Tessnow, F. E. Peterkin, et W. W. Byszewski, « Microhollow cathode discharges », *Applied Physics Letters*, vol. 68, nº 1, p. 13-15, janv. 1996.

[2] T. Dufour *et al.*, « Effect of limiting the cathode surface on direct current microhollow cathode discharge in helium », *Applied Physics Letters*, vol. 93, nº 7, p. 071508, août 2008.

[3] J. G. Eden *et al.*, « Microplasma devices fabricated in silicon, ceramic, and metal/polymer structures: arrays, emitters and photodetectors », *Journal of Physics D: Applied Physics*, vol. 36, nº 23, p. 2869, 2003.

[4] M. K. Kulsreshath *et al.*, « Study of dc micro-discharge arrays made in silicon using CMOS compatible technology », *Journal of Physics D: Applied Physics*, vol. 45, nº 28, p. 285202, juill. 2012.

[5] V. Felix *et al.*, « Origin of microplasma instabilities during DC operation of silicon based microhollow cathode devices », *Plasma Sources Science and Technology*, vol. 25, nº 2, p. 025021, avr. 2016.

[6] R. Michaud *et al.*, « Direct current microhollow cathode discharges on silicon devices operating in argon and helium », *Plasma Sources Sci. Technol.*, vol. 27, nº 2, p. 025005, 2018.

Figure 3. Cross-sectional SEM pictures of the micro reactor after operation at atmospheric pressure in (a) helium and in (b) argon.

AL/CUO SPUTTERED NANOTHERMITES AS NEW ENERGETIC THIN FILMS FOR TUNABLE IGNITION AND ACTUATION

Nicollet.A, Vivies.S, Salvagnac.L, Rossi.C*

CNRS, LAAS, University of Toulouse, 7 avenue du Colonel Roche, F-31400 Toulouse, France
*rossi@laas.fr

Topic : Integration and micro nanotechnology applications

Abstract — **Sputter-deposited Al/CuO multilayers are used to manufacture tunable igniters and actuators with applications in various fields of application such as defense, space and infrastructure safety. This paper describes the technology of deposition and characteristics of Al/CuO multilayers followed by some examples of applications of these energetic layers.**

I. INTRODUCTION

Energetic materials are widely used to generate suddenly high amount of thermal or mechanical energy under an electrical, mechanical or thermal stimulus. As typical energetic materials, nanothermites which contain Al and oxide, have attracted much attention as they exhibit not only better combustion efficiencies and better ignitability compared to traditional explosives but also the reaction outputs can be tuned thanks to the selections of fuels, oxidizers, architectures and reactant size allowing multiple actions. Among nanothermites, sputter-deposited Al/CuO multilayers represent an interesting energetic thin film nanomaterials for tunable ignition to replace old hot-wire ignitor.

In that context, our research group at LAAS-CNRS demonstrated several miniature pyrotechnical ignition devices integrating Al/CuO multilayers within MEMS based microheaters, called pyroMEMS, for application in civilian and military applications such as triggering the inflation of airbags, micro-propulsion systems, and arm and fire devices.

This paper reviews the technological process focusing on sputter-deposition technique, presents the properties of Al/CuO multilayered films and details the fabrication process flow of a micro-igniter. As conclusion, some examples of applications of pyroMEMS are overviewed.

II. AL/CuO MULTILAYERED NANOTHERMITES

Two decades ago, the introduction of nanotechnologies enabled the emergence of a new class of energetic materials called nanothermites that could play a great role in the future society. Nanothermites use raw materials that can be found in abundance, are low cost and non-polluting (green materials). They also exhibit better combustion efficiencies and better ignitability compared to typical CHNO energetic mixtures while being safer. Importantly, the reactions and ability to trigger specific actions can be tailored by varying the size and composition of the oxide, allowing multiple applications. Focusing on thermite multilayers, the overwhelming majority of works concern Al/CuO systems, as they feature an exceptionally high-energy release with gaseous production.

A. Sputter-deposition of Al/CuO multilayers

Al/CuO thermite multilayers are mainly produced by sputter-deposition technique [1]–[5] as it provides excellent control over the layering and stoichiometry. Cupric oxide thin film is synthesized using direct current (DC) reactive magnetron sputtering technique in an oxygen enriched environment. To produce Al/CuO multilayered films, layers of Al and CuO are deposited on top of each other in an alternating fashion (see Fig. 1) without venting the chamber. However, after each layer deposition, the sample stage is cooled at ambient temperature for 600 s. CuO is polycrystalline and characterized by XRD before deposition. At each interface between cupric oxide and Al layers an intermixing layer of 4-8 nm is present and formed during the deposition itself.

Depositions parameters have been published several times and can be found in [6], [7].
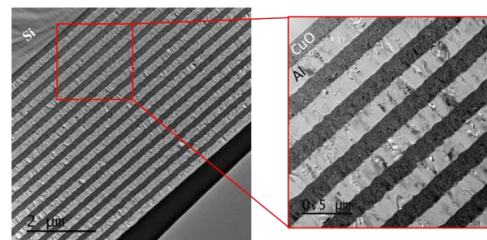

Figure 1. Cross sectional transmission electron micrographs of the Al/CuO multilayer obtained by magnetron sputtering.

B. Ignition and reaction properties

Applying an external source of energy locally on the multilayer results in an increase of the temperature in the multilayer section directly in contact with the heated surface. This can be done by electrostatic discharge [8], mechanical impact [9], laser irradiation [10], electrical heating (spark) [11] and thermal hot points [12] which is the widest used. After being ignited, the multilayers react by a self-sustained propagating reaction following the chemistry of eq. 1.

$$2.Al + 3.CuO \rightarrow Al_2O_3 + 3.Cu + \Delta H \qquad (1)$$
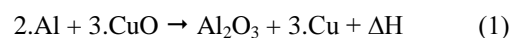
In other words, after the temperature is raised locally and rapidly to a characteristic onset reaction temperature, the reaction enthalpy (ΔH) spreads into neighboring

unreacted portions of the film, leading to a self-sustained reaction wave, which is highly luminous.

As the exothermic chemical reactions are controlled by the outward migration of oxygen atoms from the CuO matrix towards the aluminum layers, the reaction rate strongly depends on the reactant spacing (bilayer thickness). The sustained combustion rate is commonly characterized with a standard high-speed camera under ambient pressure [5], [7].

The combustion velocity increases for thinner bilayers with a maximum at ~ 90 m/s for free-standing foils (see Fig. 2(a)). However, the reaction stops suddenly for extremely small bilayer thicknesses, which is due to the presence of interfacial layers, as described earlier which reduces the amount of stored energy i.e., reaction enthalpy, ΔH.
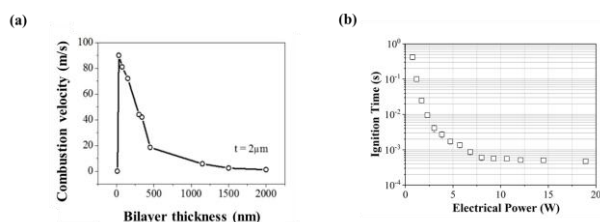
Figure 2. (a) Sustained combustion velocity in air of free-standing multilayers as a function of bilayer thickness (total thickness t=2 μm); (b) ignition time as a function of the electrical power send through the micro-heater for 5 bilayers of Al/CuO (Taken from [12]).

III. PyroMEMS integration and characterization

When integrated on a device/substrate, the widest and simplest ignition method for igniting an Al/CuO multilayered thin film is hot-wire by a local metallic thin film resistance. A pyroMEMS is mainly composed of a substrate, a thin metallic resistance and the Al/CuO nanothermites (see Fig. 3(a)).

To minimize the ignition energy, the substrate must be a good thermal insulator. We chose 500 μm thick 4-in. glass substrates (AF32 from Schott). After being cleaned in oxygen plasma to remove surface contaminants, 300 nm thick titanium followed by 300 nm thick gold layers are evaporated onto the glass substrate and the filament is patterned using lift-off technique. Then the gold is chemically etched and patterned to define the Ti resistance and Au electrical pads. Finally, Al/CuO multilayers are sputter deposited through a silicon shadow mask. A photo of a pyroMEMS thus manufactured is presented in Fig. 3(b).
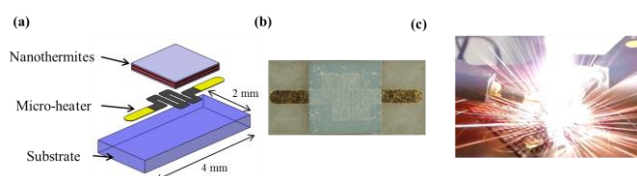
Figure 3. (a) 3D schematic representation of a pyroMEMS; (b) photo of the pyroMEMS; (c) photo during the nanothermite reaction.

We characterized that, for any heating surface areas (micro-heater sizes), the ignition time (delay between the time of application of the electrical power and the emission of the light as shown in Fig. 3(c)) rapidly decreases when the ignition power density increases until an asymptotic value, defining the minimum response ignition time, which is a characteristic of the multilayered film itself.

As an illustration, Fig. 2(b) provides the ignition time vs the ignition power for a thermite made of fifteen 300 nm thick 1:1 Al/CuO bilayers. Below a certain electrical power, no ignition occurs, regardless the duration of application of the power. This is simply explained by the fact that, below this ignition power threshold, the electrical energy supplied to the micro-heater is not sufficient to compensate for the energy lost by conduction through the substrate, by radiation from the exposed surface, and by convection in the air. The multilayer cannot reach its ignition temperature, also known as onset reaction temperature.

This threshold highly depends on the heating surface area and detailed results can be found in [12].

IV. Examples of applications

To date, igniters are the widest investigated applications and widely used to trigger the inflation of airbags, micro-propulsion systems, and arm and fire devices used in missiles, rockets and any other ordnance systems. Traditionally, igniter technology consists of a metallic hot wire (Ni/Cr, …) or bridge wire in contact with a secondary or primary explosive. The fabrication and integration of explosives in igniters require extreme precautions due to high sensitivity to the electrostatic discharge, friction or shock.

Al/CuO multilayers can efficiently replace the hot wire and primary explosive. Another advantages of replacing traditional hot-wire with pyroMEMS are: (1) the overall integration is easier requiring only the electrical connections of the pyroMEMS whereas traditional pyrotechnical igniters required at least two steps (hot wire and primary pyrotechnic composition deposition). (2) The Al/CuO multilayers are safe and less sensitive to environment. (3) Ignition threshold and reaction output (flame temperature and gaseous products) can be easily tuned by changing the Al/CuO bilayer thickness and stoichiometry (bilayer thickness ratio).

Taton et al. [13] first reported the design, realization and characterization of hot-wire ignition integrating Al/CuO multilayers (see Fig. 4 (a)-(b)) for application in pyrotechnical systems for space applications. The reactive Al/CuO multilayered thin film resides on a 100-μm-thick epoxy/polyethyleneterephtalate (PET) membrane to insulate the reactive layer from the bulk substrate. When current is supplied, Al/CuO reacts and the products of reaction produce sparks that can ignite any secondary energetic composition, such as RDX. The authors demonstrate a 100% success of ignition over 0.25–4 A firing current range corresponding to 80– 244 μJ and with response times ranging from 2 to 260 μs. Then, Glavier et al. [14] used this igniter to cut and propel a thin metallic foil and ignite RDX in a detonation. Authors showed that a stainless steel flyer of 40 mg can be properly cut and propelled at velocities calculated from 665 to 1083 m/s as a function of the RDX extent of compaction and ignition charge. The impact of the flyer can directly initiate the detonation of an RDX explosive, which is very promising to remove primary

explosives in detonators. A schematic view and photo of one miniature detonator is given in Fig. 4 (c)-(d).
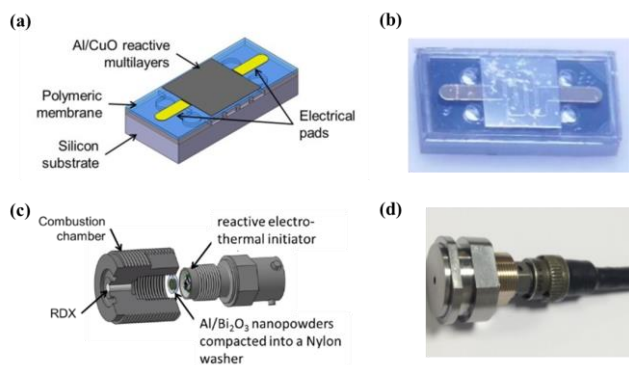

Figure 4. (a) Schematic and (b) photo of the reactive electro-thermal initiator on Epoxy/PET membrane. Chip dimension is 4 mm x 2 mm. (c) Schematic and (d) photo of one miniature detonator integrating Al/CuO multilayers as initiator. Taken from [14].

More recently, Nicollet *et al.* [12] derived the Al/CuO multilayer igniter concept for several substrates and simplified the fabrication process to adapt it to airbag initiation. Additionally, our team has demonstrated miniature one-shot circuit breakers [15] based on the combustion of a nanothermite. Each device is simply made from two assembled Printed Board Circuits (PCBs) to define a hermetic cavity in which an Al/CuO multilayer initiator chip ignites –in less than 100 µs- a few milligrams of nanothermite to cut a thick copper connection (see Fig. 5). The authors demonstrated the good operation (100 % of success rate) with a response time of 0.57 ms, which is much lower than the response time of classical mechanical circuit breakers (> ms).
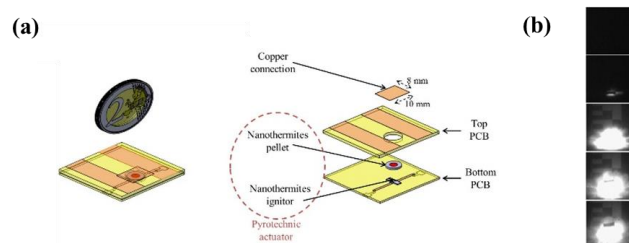
Figure 5. (a) 3D schematic of the nanothermite based circuit breaker; (b) epxloded views and (c) scnapshots of high speed images taken for the tested circuit breaker. The time between each picture is 100 µs.Taken from [15].

V. CONCLUSION

Sputter-deposited Al/CuO multilayers, composed of alternating Al and CuO nanolayers with total thickness ranging from 1 to tens of µm, present an opportunity for tunable ignition and actuation. The interest and the integration in igniter applications have been demonstrated for different applications, such as inflators, aerospace or actuators.

REFERENCES

[1] M. Petrantoni, C. Rossi, L. Salvagnac, V. Conédéra, a. Estève, C. Tenailleau, P. Alphonse, and Y. J. Chabal, "Multilayered Al/CuO thermite formation by reactive magnetron sputtering: Nano versus micro," J. Appl. Phys., vol. 108, no. 8, p. 84323, 2010.

[2] D. P. Adams, "Reactive multilayers fabricated by vapor deposition: A critical review," Thin Solid Films, vol. 576, pp. 98–128, Feb. 2015.

[3] S. Fu, R. Shen, P. Zhu, and Y. Ye, "Metal–interlayer–metal structured initiator containing Al/CuO reactive multilayer films that exhibits improved ignition properties," Sensors Actuators, A Phys., vol. 292, pp. 198–204, Jun. 2019.

[4] N. A. Manesh, S. Basu, and R. Kumar, "Experimental flame speed in multi-layered nano-energetic materials," Combust. Flame, vol. 157, no. 3, pp. 476–480, Mar. 2010.

[5] C. Rossi, "Engineering of Al/CuO Reactive Multilayer Thin Films for Tunable Initiation and Actuation," Propellants, Explos. Pyrotech., Jul. 2018.

[6] G. Lahiner, J. Zappata, J. Cure, N. Richard, M. Djafari-Rouhani, A. Estève, and C. Rossi, "A redox reaction model for self-heating and aging prediction of Al/CuO multilayers," Combust. Theory Model., 2019.

[7] J. Zapata, A. Nicollet, B. Julien, G. Lahiner, A. Esteve, and C. Rossi, "Self-propagating combustion of sputter-deposited Al / CuO nanolaminates," Combust. Flame, vol. 205, pp. 389–396, 2019.

[8] C. Weir, M. L. Pantoya, G. Ramachandran, T. Dallas, D. Prentice, and M. Daniels, "Electrostatic discharge sensitivity and electrical conductivity of composite energetic materials," J. Electrostat., vol. 71, no. 1, pp. 77–83, 2013.

[9] J. L. Cheng, H. H. Hng, Y. W. Lee, S. W. Du, and N. N. Thadhani, "Kinetic study of thermal- and impact-initiated reactions in Al-Fe2O3 nanothermite," Combust. Flame, vol. 157, no. 12, pp. 2241–2249, 2010.

[10] D. Damm and M. Maiorov, "Thermal and radiative transport analysis of laser ignition of energetic materials," in Optical Technologies for Arming, Safing, Fuzing, and Firing VI, 2010, vol. 7795, p. 779502.

[11] A. Hadjiafxenti, I. E. Gunduz, C. C. Doumanidis, and C. Rebholz, "Spark ignitable ball milled powders of Al and Ni at NiAl composition," Vacuum, vol. 101, pp. 275–278, 2014.

[12] A. Nicollet, G. Lahiner, A. Belisario, S. Souleille, M. Djafari-Rouhani, A. Estève, and C. Rossi, "Investigation of Al/CuO multilayered thermite ignition," J. Appl. Phys., vol. 121, no. 3, 2017.

[13] G. Taton, D. Lagrange, V. Conedera, L. Renaud, and C. Rossi, "Micro-chip initiator realized by integrating Al/CuO multilayer nanothermite on polymeric membrane," J. Micromechanics Microengineering, vol. 23, no. 10, p. 105009, 2013.

[14] L. Glavier, A. Nicollet, F. Jouot, B. Martin, J. Barberon, L. Renaud, and C. Rossi, "Nanothermite/RDX-Based Miniature Device for Impact Ignition of High Explosives," Propellants, Explos. Pyrotech., vol. 42, no. 3, pp. 308–317, 2017.

[15] A. Nicollet, L. Salvagnac, V. Baijot, A. Estève, and C. Rossi, "Fast circuit breaker based on integration of Al/CuO nanothermites," Sensors Actuators A Phys., vol. 273, pp. 249–255, 2018.

HIGH-YIELD ULTRA-LOW LOSSES Si₃N₄ MICRORESONATORS FOR ENERGY-EFFICIENT NONLINEAR PHOTONICS

Laurène Youssef [1], Houssein El Dirani [2], Camille Petit-Etienne [1], Corrado Sciancalepore [2], Erwine Pargon [1]

[1] Univ. Grenoble Alpes, CNRS, CEA/LETI Minatec, LTM, 38000 Grenoble, France
[2] Univ. Grenoble Alpes, CEA/LETI Minatec, DOPT, 38000 Grenoble, France
*E-mail of contact author: laurene.youssef@cea.fr

Topics: Integration and micro-technologies applications
Etching, lithography and nano-patterning

Abstract— **High confinement and ultra-low losses are required to generate Kerr frequency combs at telecom wavelengths, which is challenging for thick anomalous-dispersion Si₃N₄ waveguides. We report the fabrication of ultra-high-Q ($>5x10^6$) Si₃N₄ micro-resonators for nonlinear photonics.**

I. INTRODUCTION

Silicon-nitride-on-insulator (SiNOI) has been demonstrated as a promising chip-based platform for generating wideband frequency combs when pumped at telecom wavelengths, which could be applied to atomic clocks, on-chip spectroscopy, and terabit coherent communications. However, optical losses generally occur during the wave propagation through silicon nitride. This phenomenon is mainly due to the material intrinsic absorption (hydrogen excess and N-H overtone absorption bonds) and scattering losses generated by defects and roughness induced by the patterning process [1]. Recently, Damascene-based approaches [2] could achieve the fabrication of 2-µm-wide Si₃N₄ waveguides for low-loss resonators with a mean quality factor approaching $5x10^6$. However, such processing is inherently affected by a low cross-wafer reproducibility, limited 4-inch wafer tools, and high-cost intellectual properties required for the technological fabrication of the devices reported [2].

In this paper, we report an optimized fully subtractive fabrication process of Si₃N₄ waveguides and ring resonators on 8-inch (200-mm) CMOS pilot lines. We highlight the outstanding impact of high-temperature annealing treatment of the Si₃N₄ patterns on their optical performances. With the optimized process, critically coupled resonators with intrinsic quality factors $Q_i > 5x10^6$ using highly-confined waveguide dimensions (1.7-µm-wide, 820-nm-thick) with corresponding optical losses approaching 5 dB/m.

II. EXPERIMENTAL SETUP

A. Fabrication process flow

The fabrication process starts with a 3-µm-thick thermal oxidation of the 200 mm diameter silicon substrate. Then an 800-nm-thick Silicon Nitride layer (Si₃N₄) is deposited by low pressure chemical vapor deposition (LPCVD) following a tailored deposition method the authors published in [3, 4], which minimizes the hydrogen content and the cracking of the deposited Si₃N₄ films. A 248-nm lithography is then performed using 820-nm-thick resist mask followed by a 49 nm-thick bottom anti-reflection coating (BARC). The etching experiments are performed in an inductively coupled plasma (ICP) reactor. Prior the Si₃N₄ etching, the photoresist patterns are cured with an HBr plasma in order to increase their etch resistance, and thus to improve the etch selectivity [5]. The BARC layer is first opened with an Ar/Cl₂/O₂ plasma process, the Si₃N₄ is then etched with a CF₄/CHF₃/Ar plasma. Finally, the photoresist/BARC layers are stripped using an O₂ plasma, and the surfaces are wet-cleaned using 1% HF dip. After the etching process, several annealing treatments under various ambient (pure N₂, H₂, or N₂ with 1% O₂) and temperatures (above 800°C) have been tested. Their impacts on the waveguide morphology, roughness and optical performances have been evaluated. Nitride circuits are then encapsulated by a 2.2-µm-thick SiO₂ cladding layer deposited at 400°C by high-density plasma-enhanced chemical vapor deposition (HDP-PECVD) technique.

B. Characterization techniques

Scanning electron microscopy (SEM) is used to assess the Si₃N₄ profile after etching, while atomic force microscopy (AFM) on a tilted sample is carried out to estimate their line edge roughness (LER).

The optical characterization of the ring resonators is performed on a 300-mm Cascade prober station using a tunable laser source for direct resonance scanning, spanning the S, C and L-bands and input/ouput fiber arrays. The wavelength tuning range is 1500-1600 nm at a 0.1 pm resolution step. Statistical study was also made on the wafer for the 1.7 µm width guides at several ring bus gap dimensions (from 300nm to 600nm) in order to estimate the reproducibility of the optical losses and the quality factor of the device.

III. RESULTS AND DISCUSSIONS

A. Roughness and Morphology

After etching and without any treatment, the SiN profiles are anisotropic (88°) and their LER is quite good of 4.5 nm (**Fig.1. a-b**), considering the photoresist LER after lithography of 6.3 nm. In a previous study, we demonstrated that Si waveguide sidewalls roughness could be smoothened down to 1 nm LER by applying an H₂ annealing treatment operating at temperature in the 800-900°C range [5]. This allowed to significantly reduce the scattering losses and led to record-low optical losses of 1.2 dB.cm⁻¹ and 0.5 dB.cm⁻¹ for single-mode strip and rib Si waveguides respectively. In this study, we investigate several annealing treatments under various ambient (N₂, H₂, or N₂/O₂ (1%)) and temperatures above 800°C. None of

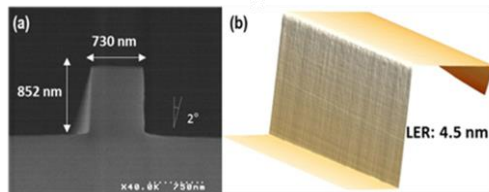the investigated treatments leads to a change of the waveguide morphology nor the roughness.

Figure 1. **a)** SEM image of a Si₃N₄ waveguide profile after subtractive patterning and **b)** the corresponding AFM image of the Si₃N₄ sidewalls and the measured LER.

B. Optical performances

The patterned resonator rings with and without annealing have been tested optically. The results for the 1.7-µm-wide waveguide being compared in **Fig.2 (a-b-c)**. Without annealing (**Fig. 2a**), we observe a critically coupled resonance for a 300 nm-gap (extinction ratio of 11 dB). The intrinsic quality factor obtained is of $8x10^5$ and the optical losses are of 0.45 dB.cm^{-1}. However, after annealing the SiN core under pure N₂ at high temperature (**Fig. 2b),** the intrinsic quality factor value increases up to $4.5x10^6$ and the optical losses decrease up to 0.07 dB.cm^{-1}. This improvement is attributed to the removal of the residual NH bonds present in the SiN bulk by the N₂ thermal annealing. Moreover, introducing an O₂ annealing prior the N₂ annealing increases further the quality factor up to $5.8x10^6$ while the optical losses reach a very low value of 0.05 dB.cm^{-1} (**Fig. 2c**). This means that oxygen annealing could generate a silicon oxynitride (SiON) interface between core SiN and SiO₂ cladding. This refractive index contrast (SiN/SiON/SiO₂) presents a promising procedure towards reaching very low optical losses devices, approaching optical fibres. In addition, the extinction ratio of the annealed sample reaches 14 dB making the bus waveguide and the resonating ring critically coupled.
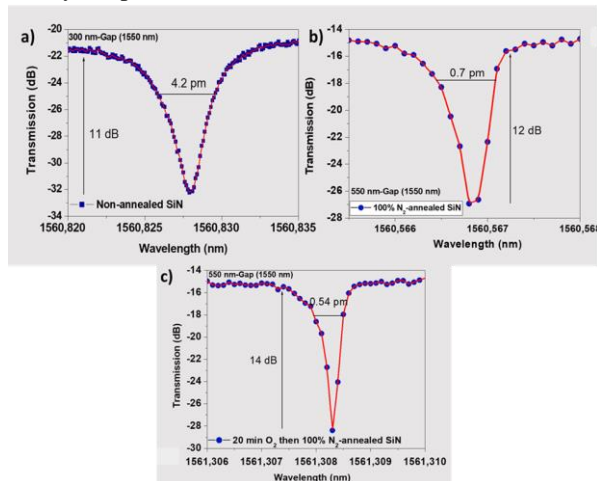
Figure 2. Resonance spectrum of a 1.7-µm bus waveguide coupled with a 112 µm diameter ring **(a)** without, **(b)** with N₂ annealing treatment and **(c)** with O₂ exposure then N₂ annealing treatment.

It is worth to point out that, the waveguide sidewalls roughness and morphology are not impacted by the annealing, as the beneficial impact of the annealing resides in an almost complete elimination of the N-H bonds, responsible for absorption losses. As a result, the clever combination of high-temperature annealings, directly impacting the SiN material properties, leads to the outstanding optical performances.

The statistical study performed on 22 dies on the 200 mm wafer shows a cross-wafer variability of the Q_i of 0.8% which proves the high reproducibility of the fabrication process. In addition, thanks to such high-quality factor devices, it was possible to generate Kerr-frequency comb at sub-mW input powers coupled into the bus waveguide, using high-confinement 1.6-1.7 µm-width waveguides.

VI. CONCLUSIONS

In conclusion, the optimization of the fabrication process of Si₃N₄ waveguides allows to obtain ring resonators with extremely high intrinsic quality factors of near $6x10^6$ and estimated optical losses as low as 0.05 dB.cm^{-1} with a high-reproducibility on a 200 mm wafer. This is to our knowledge, the best published values for highly confined SiN bus-ring resonators with dimensions as low as 1.7 µm. This is very promising for the future of high-speed data transmission and telecommunication, but also for optical sensing application using Si₃N₄ based micro-resonators as a source of wideband Kerr frequency combs at telecom wavelengths.

REFERENCES

[1] R. Dinu, E. Miller, G. Yu, B. Chen, A. Scarpaci, H. Chen, C. Pilgrim, "High-Speed Polymer Optical Modulators" in *Optical Fibers Telecommunications (Sixth Edition)* (Optics and Photonics, Ed. Academic Press), pp. 175-204 (2013).

[2] M. Pfeiffer, J. Liu, A. Raja, T. Morais, B. Ghadiani, T. Kippenberg, "Ultra-smooth silicon nitride waveguides based on the Damascene reflow process: fabrication and loss origins" in *Optica* **5**, pp. 884-892 (2018).

[3] H. El Dirani, M. Casale, S. Kerdiles, C. Socquet-Clerc, X. Letartre, C. Monat, C. Sciancalepore, "Crack-Free Silicon-Nitride-on-Insulator Nonlinear Circuits for Continuum Generation in the C-Band," in *IEEE Phot. Technol. Lett.,* **30**, pp. 355-358 (2018).

[4] H. El Dirani, A. Kamel, M. Casale, S. Kerdiles, C. Monat, X. Letartre, M. Pu, L. K. Oxenløwe, K. Yvind, C. Sciancalepore, "Annealing-free Si3N4 frequency combs for monolithic integration with Si photonics" in App. Phys. Lett., **8**, pp. 113, (2018).

[5] C. Bellegarde, E. Pargon, C. Sciancalepore, C. Petit-Etienne, V. Hughes, D. Robin-Brosse, J.M. Hartmann, P. Lyan, , "Improvement of Sidewall Roughness of Sub-Micron SOI Waveguides by Hydrogen Plasma and Annealing" in *IEEE Phot. Technol. Lett*. **30**, pp. 591-594 (2018).

Author Index